

# Cosmological Black Hole Shadows

DIMITAR PETROV

SUPERVISED BY PROF JOSEPH SULTANA

JULY 2, 2025

DEPARTMENT OF MATHEMATICS

FACULTY OF SCIENCE

UNIVERSITY OF MALTA

A Dissertation submitted in partial fulfilment of the requirements for the Degree  
of Bachelor of Science (Honours) in Mathematics as main area.



## **University of Malta Library – Electronic Thesis & Dissertations (ETD) Repository**

The copyright of this thesis/dissertation belongs to the author. The author's rights in respect of this work are as defined by the Copyright Act (Chapter 415) of the Laws of Malta or as modified by any successive legislation.

Users may access this full-text thesis/dissertation and can make use of the information contained in accordance with the Copyright Act provided that the author must be properly acknowledged. Further distribution or reproduction in any format is prohibited without the prior permission of the copyright holder.

# Contents

<b>1</b>	<b>Introduction</b>	<b>1</b>
<b>2</b>	<b>The Description of BHs</b>	<b>5</b>
2.1	Tensors and Manifolds . . . . .	5
2.2	General Relativity . . . . .	12
2.3	Symmetries and Killing vector fields . . . . .	16
2.4	So, What are BHs? . . . . .	19
<b>3</b>	<b>BH Shadows... Finally</b>	<b>23</b>
<b>4</b>	<b>BH shadows in static and spherically symmetric spacetimes</b>	<b>29</b>
4.1	Derivation of general expression . . . . .	29
4.2	BH shadow in Schwarzschild spacetime . . . . .	35
4.3	BH shadow in Reissner-Nordström spacetime . . . . .	37
4.4	Concluding Remarks . . . . .	41
<b>5</b>	<b>BH shadows in stationary spacetimes</b>	<b>44</b>
5.1	The frame-dragging effect . . . . .	45
5.2	The Kerr spacetime . . . . .	49
5.2.1	Important Surfaces . . . . .	50
5.2.2	Equatorial Photon Orbits . . . . .	54
5.2.3	General Photon Orbits . . . . .	64
5.2.4	BH shadow in Kerr spacetime . . . . .	69
5.3	Concluding Remarks . . . . .	78
<b>6</b>	<b>BH shadows at cosmological distances</b>	<b>79</b>
6.1	The expanding universe... and the FLRW metric . . . . .	79
6.2	Cosmology in brief . . . . .	81
6.3	The Kottler spacetime . . . . .	83
6.3.1	Structure and important surfaces . . . . .	84
6.3.2	BH shadow in Kottler spacetime for static observers . . . . .	88

6.3.3	BH shadow in Kottler spacetime for comoving observers . . . . .	91
6.3.4	Asymptotic limit of Kottler BH shadow . . . . .	95
6.4	The McVittie spacetime . . . . .	98
6.4.1	Structure and Flaws . . . . .	98
6.4.2	BH shadow in the McVittie spacetime . . . . .	100
6.4.3	The (inner) Schwarzschild region . . . . .	101
6.4.4	The (outer) FLRW region . . . . .	102
6.4.5	The intermediate region . . . . .	103
6.5	BH shadows in a general cosmology . . . . .	106
<b>7</b>	<b>Conclusion</b>	<b>110</b>
<b>A</b>	<b>Derivation of curvature invariants for McVittie spacetime</b>	<b>114</b>
<b>B</b>	<b>Python code for plots</b>	<b>116</b>
B.1	Plot 10 . . . . .	116
B.2	Plot 11 . . . . .	118
B.3	Plot 12 . . . . .	120
B.4	Plot 13 . . . . .	121
B.5	Plot 16 . . . . .	122
B.6	Plot 17 . . . . .	124
B.7	Plot 19 . . . . .	126
B.8	Plots 20 and 21 . . . . .	127
B.9	Plot 25 . . . . .	132
B.10	Plot 27 . . . . .	135
B.11	Plot 29 . . . . .	136
B.12	Plot 30 . . . . .	139
B.13	Plot 31 . . . . .	140

# List of Figures

1	The only two BHs ever imaged by mankind (so far). The EHT collaboration allows us to image objects whose angular size is in the order of microarcseconds. This is analogous to imaging a coin on the surface of the Moon from Earth. . . . .	3
2	The Kretschmann scalar as a function of radial distance, for a static and uncharged (Schwarzschild) BH. This plot is not to scale. The 3d funnelling of spacetime arises from the central mass, which is hidden by the event horizon. . . . .	22
3	Light rays (in red) received by an observer from distant stars after being gravitationally lensed by a static and non-rotating BH. In the grey shaded cone, no incoming photons from the stars can be received due to the BHs strong gravitational field (in blue). . . . .	24
4	An image of galaxy LRG 3-757 gravitationally lensing a background blue galaxy. The perfect alignment of these two galaxies allows us to receive light from the distant galaxy in a ring all around LRG 3-757 [22]. . . . .	24
5	The three categories of past-emitted photons emitted by an observer. Photons emitted inside the grey cone will be absorbed by the BH, tangential at the vertex will spiral into a circular orbit, and outside the cone will escape to infinity. Diagram adapted from figure 1 in [47]. . . . .	26
6	The angular size of the event horizon and photon sphere as projected onto an observer's sky assuming a Euclidean geometry. In a general BH spacetime, the phenomenon of light bending will lead to photons having a curved path. Photons comprising the BH shadow will appear to arrive from an area much larger than the photon sphere itself. Diagram adapted from figure 3 in [47]. . . . .	27
7	A Schwarzschild BH surrounded by a thin accretion disk, viewed from an inclination of $10^\circ$ above the disk's plane. The inner bright ring corresponds to the projection of the unstable photon sphere. The diagram was generated through a primitive computer simulation in 1979 [36]. . . . .	28
8	The trajectory of a photon being emitted towards a BH by an observer. In the strong gravitational regime, the photon's geodesic path will deform increasingly before receding away towards infinity. At some azimuthal angle with respect to the BH, the radial distance will reach a minimum at $r = R$ . If $R = r_{ps}$ , the photon will become trapped in a circular orbit. . . . .	32
9	Measure of distance in a spherically symmetric and static spacetime. Given the spherical coordinate system in grey, the spatial scaling factors are obtained from the metric tensor. Diagram adapted from figure 5 in [47]. . . . .	33

10	Angular size of a Schwarzschild BH with various observed distances, $r_O$ , and geometric masses, $m$ . Although equation 27 was used for the plot, the approximation in equation 24 can be used for distant observers. The yellow background depicts the homogeneously spread light sources. The program used to plot this figure can be found in appendix B.1. . . . .	38
11	Plot showing the pair of photon spheres and event horizons of the Reissner-Nordström BH of mass $m = 1$ and charge $Q \in [0, m]$ . A vertical section will give the radial distance to each surface from the singularity at $r = 0$ . Note that if the charge domain was extended to $[0, \sqrt{9/8}m]$ , then the photon spheres would coincide at $Q = m\sqrt{9/8}$ . The program used to plot this figure can be found in appendix B.2. . . . .	40
12	The angular size of a Reissner- Nordström BH shadow as a function of electric charge $Q$ . This uses the parameters $r_O = 10m$ and $m = 10$ , while $Q$ varies in the interval $[0, m]$ . The leftmost shadow having $Q = 0$ is identical to the Schwarzschild case, while the rightmost is the extremal Reissner-Nordström case. The internal white disk is added to compare each shadow to the extremal case. The program used to plot this figure can be found in appendix B.3. . .	42
13	A comparison between the angular size of a Schwarzschild and a Reissner-Nordström BH shadow, in blue and in red, respectively. Here we have set $m = 1$ and $r_O = 100m$ , while $Q \in [0, m]$ is variable. In the extreme case when $Q = m$ , the Reissner-Nordström BH shadow appears $\sim 23.5\%$ smaller than the Schwarzschild one. The program used to plot this figure can be found in appendix B.4. . . . .	43
14	A composite image of Centaurus A, the nearest active radio source to Earth. A fraction of the ionised matter from its accretion disk is continuously ejected at speeds close to that of light along its axis of rotation. The jets extend up to 1.5 million light years from the centre. This is over 15 times the diameter of the Milky Way [71]. . . . .	45
15	The frame-dragging (Lense-Thirring) effect present in the proximity of a rotating BH. The clockwise rotation of the BH causes the local spacetime around the BH to experience a 'drag' in the direction of the rotation. The geodesics depicted are all found in the equatorial plane.	49
16	Surfaces characteristic to the Kerr BH in Boyer-Lindquist coordinates. In these plots, the $r$ coordinate describes the radial distance while the inclination angle $\theta$ increases clockwise starting from the vertical $z$ -axis ( $\theta = 0^\circ$ ). The BH is also rotating along the $z$ -axis. The program used to plot this figure can be found in appendix B.5. . . . .	54

17	Plots of $V_{\pm}^{\text{eff}}(r)$ as functions of the radial orbital distance, $r$ . The left plot corresponds to the co-rotating case, while the right plot corresponds to the counter-rotating case. We have set $m = L = 1$ , and $ a  = 0.8$ . The two green vertical lines correspond to the locations of the two event horizons (found from 47), while the dashed line highlights the exact turning point of $V_{+}^{\text{eff}}(r)$ . The grey region is forbidden for equatorial photon orbits. The program used to plot this figure can be found in appendix B.6. . . . .	59
18	Visualisation of photon trajectories for three distinct values of the total radial energy, $E$ . The blue curve on the plot corresponds to $V_{+}^{\text{eff}}(r)$ for the counter-rotating case. The colour of each energy level corresponds to a photon trajectory on the RHS. . . . .	60
19	Plot of radial distance for equatorial photon orbits, $r_{\text{ps},\pm}$ , and event horizons, $r_{\text{eh},\pm}$ , against the spin parameter, $a$ , for a Kerr BH of geometric mass $m = 1$ . The program used to plot this figure can be found in appendix B.7. . . . .	63
20	The important surfaces of a Kerr BH, together with a corresponding photon region, in Boyer-Lindquist coordinates. The volume encapsulated by the photon regions (in pink) was obtained numerically by following [27, 44, 46]. The boundary of the photon region is characterised by $\Theta(\theta) = 0$ . The program used to plot this figure can be found in appendix B.8. . . . .	68
21	The important surfaces of a Kerr BH in Kerr-Schild coordinates. The plot is obtained by transforming the surfaces in figure 20 using equation 49. The program used to plot this figure can be found in appendix B.8. . . . .	69
22	Three different spherical photon orbits around a Kerr BH with $a = 0.9m$ and $m = 1$ . The black circle corresponding to the BH itself is not to scale! The orbits have different bounds on their inclination angle $\theta$ – as measured from the axis of rotation (grey arrow). The LHS plot has $\theta \in [0, \pi]$ , the middle has $\theta \in [\frac{3\pi}{10}, \frac{7\pi}{10}]$ , and the RHS has $\theta \in [\frac{3\pi}{7}, \frac{4\pi}{7}]$ . Since the photon paths do not start and end at the same point, 60 revolutions around the BH were plotted. . . . .	70
23	A distant observer at spatial coordinates $(r_O, \theta_O)$ with respect to a Kerr BH rotating about the $z$ -axis. The three spatial axes $\{e_1, e_2, e_3\}$ belonging to the distant observer are also depicted together with a past-emitted photon ray with celestial coordinates $(\gamma, \psi)$ , which spirals into unstable spherical orbit at some fixed $r = r_{\text{ps}}$ . Such photons will be used to construct the BH shadow. The diagram is adapted from figure 7 in [27]. . . . .	71
24	The parametrisation of an observer’s sky, $\mathbb{S}^2$ . Every past-emitted photon ray has associated celestial coordinates $(\gamma, \psi)$ . Some directions corresponding to specific values of $\gamma$ and $\psi$ are also depicted to aid the visualisation. The diagram is adapted from figure 8 in [27]. . . . .	72

25	Four subplots each showcasing the effects of a parameter on the shape and size of the Kerr BH shadow, as seen by a ZAMO. For each subplot, three out of the four parameters ( $r_O, \theta_O, a, m$ ) were kept constant, usually in a near-extremal regime. The program used to plot this figure can be found in appendix B.9. . . . .	77
26	An observer located at $t = t_1$ in an expanding universe measures angular sizes of cosmological objects (in red) as they appeared in the past ( $t_0 < t_1$ ) since the speed of light is finite. Although the diameter $2R$ of the red object cannot be measured through direct observation, this can be inferred from other factors such as its mass or gravitational effects. . . . .	83
27	The locations of the event horizons and photon sphere for a Kottler BH of mass $m = 1$ , as a function of $\Lambda$ . A logarithmic scale was used to visualise the asymptotic nature of $r_{\text{eh},+}$ , which diverges as $\Lambda \rightarrow 0$ . Moreover, the inner event horizon coincides with the Schwarzschild one (at $2m$ ) as $\Lambda \rightarrow 0$ . Expectedly, the photon sphere has a constant radial distance for any $\Lambda$ . The three surfaces coincide in the extremal case when $\Lambda = \frac{1}{9m^2}$ . The program used to plot this figure can be found in appendix B.10. . . . .	88
28	A diagram showing the expansion of the universe using two snapshots at $t = t_0, t_1$ . A static observer will not change their position with respect to their initial one, while a comoving observer will allow themselves to be dragged with the expansion. A comoving observer will have an associated 4-velocity away from the BH, which induces redshift effects. . . . .	89
29	Plots showcasing the angular size of Kottler BH shadows against radial distance, for both static and comoving observers, using equations 113 and 131. The mass of the BH is fixed at $m = 1$ . Each curve represents the shadow profile characterised by some fixed $\Lambda$ . These plots generalise figure 4 from [48], and figure 7 from [20]. The program used to plot this figure can be found in appendix B.11. . . . .	97
30	Plot showcasing the angular sizes of BH shadows in a McVittie spacetime. In particular, it was assumed that the Schwarzschild BH of mass $m = 1$ was embedded in a matter-dominated FLRW cosmology. The Hubble constant was varied to distinguish the effects of rapid expansion on the shadow. While the shadow coincides with the Schwarzschild shadow close to the photon sphere, it diverges as $R_O$ is increased. This plot generalises figure 2 from [65]. The program used to plot this figure can be found in appendix B.12. . . . .	106
31	Plot of angular diameter distance (solid line) and BH shadow size in the outer cosmological region (dashed line). This plot describes a BH of mass $m = 1$ embedded in an expanding McVittie spacetime with $H_0 = 1$ . Note that in the region of low redshift, $\alpha_{\text{outer}}$ is not representative of the actual BH shadow size since $\alpha_{\text{inner}}$ and $\alpha_{\text{overlap}}$ are non-negligible! The program used to plot this figure can be found in appendix B.13. . . . .	107

## List of Tables

1	Table showing the classification of stationary and asymptotically flat BH spacetimes. . . . .	22
2	A summary of the results obtained from our discussion, in regards to the angular sizes of BH shadows. In the case of the Kerr spacetime, this is given as a parametric curve due to the non-circular nature of the BH shadow. Moreover, its distant observer approximation was taken from [47]. . . . .	110

# Glossary

## Abbreviations

- BH: Black Hole  
CP: Cosmological Principle  
EFEs: Einstein Field Equations  
EHT: Event Horizon Telescope  
ELEs: Euler-Langrange Equations  
FE1/FE2: Friedmann Equations 1 and 2  
FLRW: Friedmann-Lemaitre-Robertson-Walker  
GR: General Relativity  
LHS: Left-Hand Side  
NG: Newtonian Gravitation  
RHS: Right-Hand Side  
ZAMO: Zero Angular Momentum Observer

## Mathematical Objects

- $\partial_\mu$ : Directional derivative along  $x^\mu$   
 $\nabla_\mu$ : Covariant derivative with respect to  $x^\mu$   
 $g_{\mu\nu}$ : Metric tensor  
 $\Gamma_{\alpha\beta}^\mu$ : Christoffel symbols  
 $R_{\mu\nu\alpha\beta}$ : Riemann curvature tensor  
 $R_{\mu\nu}$ : Ricci tensor  
 $R$ : Ricci scalar  
 $\Lambda$ : Cosmological constant  
 $T_{\mu\nu}$ : Energy-momentum tensor  
 $G_{\mu\nu}$ : Einstein tensor  
 $\kappa_{\text{Ricci}}$ : Normalised Ricci curvature

$\kappa_{\text{Kretsch}}$ : Kretschmann scalar

$\mathcal{L}$ : System Lagrangian

$\mathcal{H}$ : System Hamiltonian

$\mathbb{S}^2$  - Surface of a 3d sphere

$\gamma, \psi$  - Coordinates parametrising  $\mathbb{S}^2$  (colatitude and azimuth)

## Physical Variables

$\alpha_{\text{sh}}$ : Angular size of the black hole shadow

$M$ : Black hole mass

$m$ : Geometric mass

$Q$ : Electric charge

$J$ : Angular momentum of the black hole

$a$ : Spin parameter

$b, \eta, \xi$ : Impact parameters

$r_{\text{ps}}$ : Radius of the photon sphere

$r_{\text{eh}}$ : Radius of the event horizon

$r_O, \theta_O$ : Observer distance and inclination

$E$ : Total (radial) energy

$L$ : Angular momentum about axis of symmetry

$K$ : Carter constant

$V_{\pm}^{\text{eff}}$ : Effective (radial) potential of an orbit

$H(t)$ : Hubble parameter

$z$ : Cosmological redshift

$a(t)$ : Scale factor of the universe

$\rho(t)$ : Energy density

$p$ : Pressure

$d_A(z)$ : Angular diameter distance

$(\Omega_{0m}, \Omega_{0\Lambda}, \Omega_{0r})$ : Cosmological parameters for matter, dark energy and radiation, respectively

# ABSTRACT

Dimitar Petrov, B.Sc. (Hons.)

Department of Mathematics, May 2025

University of Malta

A black hole (BH) shadow is a dark region on an observer's sky where light from distant sources is completely absorbed due to a BH's strong gravitational pull. The first direct image of a BH shadow, captured by the Event Horizon Telescope (EHT) in 2019, not only confirmed the existence of BHs, but also highlighted the importance of understanding their visual appearance. The angular size of a BH's shadow is significantly larger than its event horizon, since the former is determined by the gravitational lensing of light rays emitted from unstable photon orbits.

This dissertation presents an in-depth theoretical study of BH shadows across various spacetimes, with a focus on the impact of cosmic expansion. We begin by analysing static and spherically symmetric BH spacetimes, deriving a general expression for their shadow's angular size and applying it to the Schwarzschild and Reissner-Nordström solutions. Next, we explore stationary spacetimes, where inertial frame-dragging effects in rotating BHs deform the shadow shape. In particular, the photon orbits and the BH shadow in the Kerr spacetime were studied extensively. Finally, we investigate cosmological BHs embedded in an expanding FLRW universe, using the Kottler (Schwarzschild-de Sitter) and McVittie solutions to model how a dynamic universe influences shadows for both static and comoving observers. This leads us to develop an approach for obtaining the angular size of a BH shadow in a general cosmology.

---

# 1 Introduction

We are fortunate to live in an era of significant technological progress, which allows many longstanding theories to finally be tested, decades after their inception. This is particularly true for physics at both the smallest and largest scales – particle physics and astrophysics. Recent breakthroughs in these fields include the detection of the Higgs Boson at the Large Hadron Collider in 2012, direct observations of gravitational waves by the Laser Interferometer Gravitational-Wave Observatory in 2015, and the first photograph of a Black Hole (BH) by the Event Horizon Telescope in 2019 [4, 56]. These discoveries have opened new frontiers for subsequent investigations in their respective areas.

In particular, the 2019 photograph of the supermassive BH in the centre of the Messier 87 (M87\*) galaxy has fuelled interest in the search for other BHs. In 2022, this was followed by the release of an image of the BH at the centre of our galaxy, Sagittarius A\*. These images have been displayed in figure 1 [4, 5]. Together, these photographs have shed light on some of the most mysterious and complex objects in the universe, providing crucial observational data for validating existing theoretical models.

Unbeknownst to most, the theoretical groundwork for BHs was established over a century ago, in 1916, when Karl Schwarzschild used Albert Einstein’s newly discovered theory of General Relativity (GR) to describe the gravitational field around spherical masses in vacuum space. Despite the consistency of his result with theory, the existence of BHs, beyond simply being a mathematical curiosity, remained controversial for decades [59]. In the 1930s, Subrahmanyan Chandrasekhar showed substantial proof that white dwarfs with a mass in excess of 1.4 solar masses (modern value) would likely collapse into neutron stars or even BHs. Further evidence of this collapse also came from Roger Penrose in the 1960s [15]. As time went on, and with a surge in indirect evidence, the existence of BHs became more widely accepted throughout academia. Direct observational evidence for their existence did not come about until 2019, as previously mentioned.

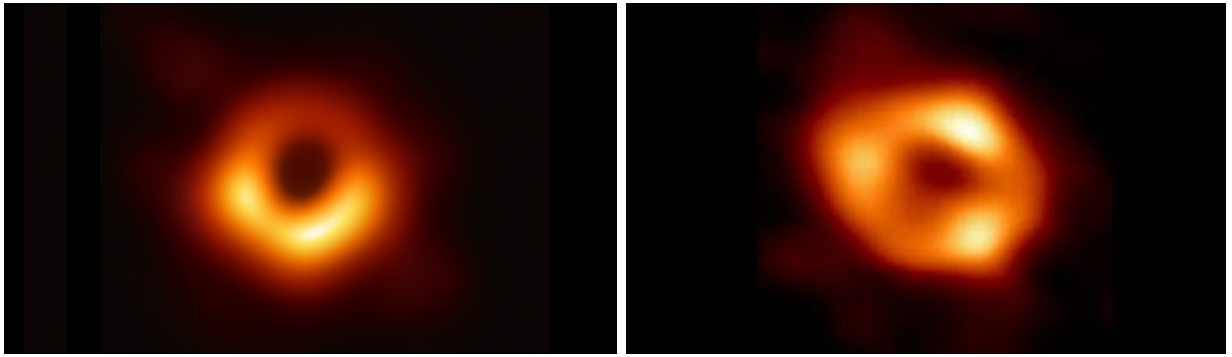
---

The motivation for studying these astrophysical objects stems from their compact structure, which gives rise to extreme gravitational effects. These effects provide a unique opportunity to directly test theories of gravity, particularly under conditions where conventional physics breaks down. Yagi and Stein, in their work "Black Hole Based Tests of General Relativity" [72], provide a comprehensive overview of such tests. From the list of relevant tests, we can highlight the growing interest in alternative theories of GR. These new models are mostly driven by observational data from redshift and other late-time data. They can be tested using BH image data as presented by Mizuno et al in "The Current Ability to Test Theories of Gravity with Black Hole Shadows" [39].

Beyond these alternative theories of gravity, a BH's observed shape and size are of fundamental importance due to the information encoded within it. Kumar and Zakharov, among others, have developed theoretical methods to extract key parameters intrinsic to BHs – such as their mass, charge, and angular momentum – based on the properties of their shadows [33, 70, 73]. While the influence of these parameters on BH shadows has been extensively studied, most analyses assume a static universe, neglecting cosmic expansion and comoving effects. Moreover, given that most BHs reside at cosmological distances, it is essential to account for the expansion of the universe in more accurate theoretical models used to describe these shadows.

This dissertation presents a detailed discussion on BH shadows across various spacetimes, with a mixture of analytical and approximate results to study their appearance. The dissertation begins with the most fundamental examples, before relaxing some of the restrictions on our spacetime to include the larger classes of rotating, and eventually cosmological, BHs. More specifically, it is structured as follows:

- ✿ Section 2 lays the mathematical groundwork, with an emphasis on differential geometry, GR, and spacetime symmetries. This will be essential to our formal understanding of



(a) M87\* image (EHT, 2019) [4].

(b) Sagittarius A\* image (EHT, 2022) [5].

Figure 1: The only two BHs ever imaged by mankind (so far). The EHT collaboration allows us to image objects whose angular size is in the order of microarcseconds. This is analogous to imaging a coin on the surface of the Moon from Earth.

BHs and the structure of their spacetimes.

- ⌘ Section 3 defines BH shadows intuitively, and introduces terminology specific to them. Moreover, the idea of circular photon orbits is provided. These will be essential in constructing the shadow of a BH.
- ⌘ Section 4 studies the shadows in static and spherically symmetric spacetimes. This is the simplest class of BHs to analyse due to the strict constraints they impose on the dynamics of light. An analytical expression for the general angular size of BH shadows in such spacetimes is derived, with the Schwarzschild and Reissner-Nordström BHs used as specific examples.
- ⌘ Section 5 extends our discussion to stationary and axisymmetric spacetimes, with a specific emphasis on the Kerr BH. Prior to deriving its shadow, the topics of frame-dragging and spherical photon orbits were analysed in great detail. These were found to improve intuition regarding the influence of rotation on the null geodesics. Following this, the shadow of a Kerr BH was derived analytically using celestial coordinates on an observer’s sky.
- ⌘ Section 6 finally expands our discussion to BHs embedded in an expanding universe.

---

An introduction to concepts used in modern cosmology is provided, and the Kottler (Schwarzschild-de Sitter) and McVittie spacetimes are used as specific cases of cosmological BHs. A method for estimating the shadow size in a general expanding universe is also provided.

The dissertation is also supplemented with a large number of original diagrams and graphs, designed to visualise the shadows and other interesting features. Such visuals were rarely encountered in literature and took considerable time and effort to generate. Furthermore, accompanying this work are 13 Python codes that were used to create the graphs. By making these diagrams and tools openly available, I hope to facilitate and inspire the creation of more useful visuals.

---

## 2 The Description of BHs

We begin by introducing the mathematical concepts necessary to describe the nature of BHs. In the following subsections, a brief introduction to manifolds, symmetries, and GR is provided.

### 2.1 Tensors and Manifolds

Experience leads us to believe that spacetime can be described by three spatial and one time dimension (ignoring all claims of extra dimensions made by string theory). The time coordinate, denoted by  $x^0$ , takes values from  $(0, \infty)$ , while the three spatial coordinates, usually denoted by  $(x^1, x^2, x^3)$ , can take any value from  $(-\infty, \infty)$ . Often, we describe spacetime as being a continuum, since there are no points that seem to be forbidden by some apparent universal law [15]. Besides the nature of the dimensions, the 4-space must also account for some additional constraints on its geometry. These are derived from empirical observations of the universe.

Firstly, we observe that, locally, our universe spatially resembles the Euclidean space  $\mathbb{R}^3$  at every instant in time. However, we must not falsely assume that the universe resembles  $\mathbb{R}^3$  globally! In fact, as we have already hinted, gravity is an apparent effect that arises from the curvature of spacetime. By definition, Euclidean space has zero curvature everywhere. Hence, the universe is probably very different on large scales, as opposed to our local reality. It is worth mentioning that this so-called curvature is represented by a tensor assigning a value to each point in the 4-space. Physically, curvature probably manifests itself quite differently from that in our familiar 3 dimensions [38].

Secondly, we require this space to be smooth ( $C^\infty$ ), given that there are no abrupt changes observed in the magnitude of this curvature; otherwise, the local Euclidean nature of spacetime will be contradicted. This leads us to the definition of a real differential manifold.

**Definition 2.1.** An  $n$ -dimensional smooth real differential manifold,  $\mathcal{M}$ , is a set together with a collection of open sets  $\{O_\alpha\}_{\alpha \in \mathcal{A}}$  satisfying:

- ★ The family  $\{O_\alpha\}_{\alpha \in \mathcal{A}}$  covers  $\mathcal{M}$ ; that is,

$$\bigcup_{\alpha \in \mathcal{A}} O_\alpha = \mathcal{M}.$$

- ★ For each  $\alpha \in \mathcal{A}$ ,  $\exists \psi_\alpha : O_\alpha \rightarrow U_\alpha$  bijective map between open sets, with  $O_\alpha \subset \mathbb{R}^n$  open subset. The pair  $(O_\alpha, \psi_\alpha)$  is called a chart.
- ★ If  $O_\alpha \cap O_\beta \neq \emptyset$  with  $\alpha \neq \beta$ , then  $\psi_\beta \circ \psi_\alpha^{-1} : \psi_\alpha[O_\alpha \cap O_\beta] \rightarrow U_\beta$  must be a  $C^\infty$  map. Here,  $\psi_\alpha[O_\alpha \cap O_\beta] \subset U_\alpha$  and  $\psi_\beta[O_\alpha \cap O_\beta] \subset U_\beta$  are both open subsets of  $\mathbb{R}^n$  [68].

As a matter of fact, manifolds were conceived precisely as a way to generalise our intuitive experience of living in a locally Euclidean space, while allowing for the possibility of being in a universe that may not be spatially Euclidean on a global scale. Despite the rigorous definition presented above, we will not discuss its intricate details further, as they are not central to our current discussion. Interestingly, this definition is rarely encountered in modern literature and textbooks, which often provide a more physics-based (low-level) approach [15, 68].

Having defined a manifold, we can now discuss the concept of vectors within this space. Of particular interest are the tangent and cotangent spaces on manifolds, as these naturally satisfy the axioms of a vector space.

**Definition 2.2.** The tangent space of any point  $p \in \mathcal{M} = \mathcal{M}(x_1, \dots, x_n)$ , denoted  $T_p \mathcal{M}$ , is the vector space that is tangential to the manifold at  $p$ .

We call elements of  $T_p \mathcal{M}$  contravariant vectors with components denoted by superscripts as  $A^\mu := (A^0, A^1, \dots, A^n) \in T_p \mathcal{M}$  [2].

A natural basis for  $T_p\mathcal{M}$  arises from the one-to-one correspondence between tangent vectors and directional derivatives in  $\mathbb{R}^n$ . More specifically, the set of tangent vectors  $\{\partial_\mu\} := \left\{\frac{\partial}{\partial x^\mu}\right\}_{\mu=1}^n$  on the surface of the manifold form the required basis for  $T_p\mathcal{M}$ . This is discussed in more depth in [15, 68].

Dually, we may also define the cotangent space [15].

**Definition 2.3.** Let  $p \in \mathcal{M} = \mathcal{M}(x_1, \dots, x_n)$ , and let  $B = \{\partial_\mu\}$  be a basis for  $T_p\mathcal{M}$ . Then, the cotangent space, denoted  $T_p^*\mathcal{M}$ , is the vector space that is spanned by dual vectors from a basis  $B^* = \{dx^\nu\}$ . A dual vector  $dx^\nu$  is an element this basis  $B^*$  if:

$$\langle dx^\nu, \partial_\mu \rangle = \delta_\mu^\nu, \quad \forall \partial_\mu \in B \text{ and } \forall dx^\nu \in B^*.$$

Elements of  $T_p^*\mathcal{M}$  are called covariant vectors with components denoted by subscripts as  $B_\mu = (B_0, B_1, \dots, B_n) \in T_p^*\mathcal{M}$  [2].

While more formal definitions for these spaces exist, the above description suffices for our purposes, avoiding unnecessary details [2].

Before proceeding further, we must briefly introduce some notation. This will greatly simplify our expressions, at the expense of perhaps not being very readable for first-time readers. However, given that tensor expressions tend to be expressed in component form, using the Einstein summation convention is preferred. We shall make the following two shortcuts [14]:

- ⌘ A repeated index within the same term denotes summation, i.e.

$$A^\mu B_\mu := \sum_{\mu=1}^n A^\mu B_\mu.$$

If such an index appears in a term, it will always denote a summation. Such indices are called dummy indices, as they can be replaced by any other letter without changing the meaning of the expression.

⌘ On the other hand, a free index is used to access individual components of an array.

An example of a free index is  $\nu$  in the term:

$$\begin{aligned} A^\mu B_\mu C^\nu &:= \sum_{i=1}^n A^i B_i C^\nu \\ &= \left( \sum_{\mu=1}^n A^\mu B_\mu C^0, \sum_{\mu=1}^n A^\mu B_\mu C^1, \dots, \sum_{\mu=1}^n A^\mu B_\mu C^n \right) \\ &= \sum_{\mu=1}^n A^\mu B_\mu (C^0, C^1, \dots, C^n) \end{aligned}$$

An annoying consequence of dealing with (co)tangent spaces is the difficulty in relating vectors belonging to distinct (co)tangent spaces. The curvature of our manifold necessitates the use of a method by which vectors can be systematically transported between different spaces, to enable their direct comparison. This requires us to gain a deeper understanding of the geometry of our locally Euclidean manifold.

In particular, we begin by generalising the definition of a linear transformation between two Euclidean spaces using the concept of tensors  $\mathbb{R}^n$  [15].

**Definition 2.4.** A tensor  $T$  of type  $(m, n)$  is a multilinear map from a collection of  $m$  covariant and  $n$  contravariant vectors into  $\mathbb{R}$ . If  $B = \{\partial_{\mu_i}\}_{i=1}^n$  is a basis for  $T_p\mathcal{M}$ , and  $\{dx^{\nu_j}\}_{j=1}^m$  is a basis for  $T_p^*\mathcal{M}$ , then in component form [15]:

$$T := T^{\mu_1 \mu_2 \dots \mu_m}{}_{\nu_1 \nu_2 \dots \nu_n} (\partial_{\mu_1}, \dots, \partial_{\mu_n}, dx^{\nu_1}, \dots, dx^{\nu_m})$$

Upon a change of coordinates:

$$(x^{\mu_1}, \dots, x^{\mu_m}, x^{\nu_1}, \dots, x^{\nu_n}) \rightarrow (\bar{x}^{\alpha_1}, \dots, \bar{x}^{\alpha_m}, \bar{x}^{\beta_1}, \dots, \bar{x}^{\beta_n}),$$

the components of a tensor change according to the transformation rule [2]:

$$\bar{T}^{\alpha_1 \dots \alpha_m}{}_{\beta_1 \dots \beta_n} = \frac{\partial \bar{x}^{\alpha_1}}{\partial x^{\mu_1}} \dots \frac{\partial \bar{x}^{\alpha_m}}{\partial x^{\mu_m}} \frac{\partial \bar{x}^{\nu_1}}{\partial x^{\beta_1}} \dots \frac{\partial \bar{x}^{\nu_n}}{\partial x^{\beta_n}} T^{\mu_1 \dots \mu_m}{}_{\nu_1 \dots \nu_n}$$

Through this definition, we note that a scalar is nothing but a  $(0, 0)$  type tensor, a tan-

gent vector  $(1, 0)$ , and a cotangent vector  $(0, 1)$ .

By far the most important tensor for the study of differential geometry and GR is the metric tensor  $g_{\mu\nu}$ . This tensor encodes the structure of spacetime in a way that allows us to define the fundamental notions of distances, angles, curvature, and causal structure. For this reason, there are certain constraints on its components. Namely [15]:

- ⌘ It is symmetric on its two indices:  $g_{\mu\nu} = g_{\nu\mu}$ . Hence, in 4-space, only 6 of its 10 total entries will be independent.
- ⌘ It is non-degenerate:  $\det(g_{\mu\nu}) \neq 0$ , meaning that its inverse  $g^{\mu\nu}$  exists. These are related through the Kronecker delta tensor:  $g^{\mu\sigma}g_{\sigma\nu} = \delta_\nu^\mu$ . This allows us to state the 4d spacetime volume element as  $\sqrt{|\det(g_{\mu\nu})|}d^4x$
- ⌘ It has the Lorentzian signature  $(- + + +)$ , i.e. it has three positive and one negative eigenvalue.

Besides the aforementioned uses of the metric tensor, it also finds use in other, more technical scenarios. In particular, the metric tensor [2, 38]:

- ⌘ Defines the inner product between any two vectors,  $A$  and  $B$ , as:

$$g(A, B) = g_{\mu\nu}A^\mu B^\nu,$$

- ⌘ Raises and lowers indices of vectors. Indeed, for every contravariant and covariant vector,  $A^\mu$  and  $B_\nu$ , respectively:

$$A_\nu = g_{\mu\nu}A^\mu, \quad \text{and} \quad B^\mu = g^{\mu\nu}B_\nu$$

- ⌘ Defines the line element on a manifold. This is an especially important concept for our future discussion. This line element is obtained from the inner product between the basis vectors (differentials):

$$ds^2 = g_{\mu\nu}dx^\mu dx^\nu \tag{1}$$

Naturally, the metric tensor is used to define countless other tensors related to the geometry of spacetime. In particular, we can give mention to another set of objects fundamental to our study of curvature – the Christoffel symbols. This object establishes a local connection between the distinct (co)tangent spaces on a manifold. It must therefore be defined in terms of our metric tensor and its derivatives.

**Definition 2.5.** The Christoffel symbols of the second kind for a metric tensor  $g_{\mu\nu}$  are given by [2]:

$$\Gamma^\mu_{\alpha\beta} := \frac{1}{2} g^{\mu\nu} (\partial_\beta g_{\nu\alpha} + \partial_\alpha g_{\nu\beta} - \partial_\nu g_{\alpha\beta}),$$

Although this connection is not a tensor since it does not satisfy the transformation rule for tensors, it is still used to define other tensors. In fact, the Christoffel symbols are central to the definition of the covariant derivative. This type of derivative generalises partial derivatives to manifolds by being a tensor, and is also coordinate-independent.

**Definition 2.6.** let  $g_{\mu\nu}$  be a metric on the manifold  $\mathcal{M}$ . The covariant derivative of a contravariant vector  $A^\mu$  is [2]:

$$\nabla_\nu A^\mu := \partial_\nu A^\mu + \Gamma^\mu_{\nu\alpha} A^\alpha$$

As a special subcase, in Euclidean 4-space with Cartesian spatial coordinates  $(x, y, z)$ , the covariant derivative reduces to the partial derivative:  $\nabla_\nu A^\mu \equiv \partial_\nu A^\mu$ , since  $\Gamma^\mu_{\nu\alpha} = 0$ .

It should be noted that this is not the only derivative that can be defined on a general manifold. It is simply the most commonly used. This is in part due to its pivotal role in defining the most important tensor used for the study of curvature – the Riemann curvature tensor. Intuitively, this tensor was designed to hold all the information regarding the curvature of a manifold. Many other tensors can be defined using the Riemann tensor [15].

**Definition 2.7.** On a manifold  $\mathcal{M}$  with metric tensor  $g_{\mu\nu}$ , we may define [2, 15]:

- ★ The Riemann curvature tensor, as defined by the Christoffel symbols:

$$R^\alpha_{\beta\gamma\delta} := \partial_\gamma \Gamma^\alpha_{\beta\delta} + \Gamma^\alpha_{\mu\gamma} \Gamma^\mu_{\beta\delta} - \Gamma^\alpha_{\mu\delta} \Gamma^\mu_{\beta\gamma} - \partial_\delta \Gamma^\alpha_{\gamma\beta},$$

With the explicit property that:

$$R^\alpha_{\beta\gamma\delta} \equiv 0 \iff \mathcal{M} \text{ is flat}$$

- ★ The Ricci tensor, as obtained by contracting the Riemann tensor:

$$R_{\beta\delta} := R^\alpha_{\beta\alpha\delta}$$

- ★ The Einstein tensor, which is a trace-reversed version of the Ricci tensor in 4-space:

$$G_{\mu\nu} := R_{\mu\nu} - \frac{1}{2} g_{\mu\nu} R^\alpha_\alpha$$

These tensors allow us to define several scalars which quantify the overall presence of curvature on the manifold (spacetime), usually, these are obtained through some contraction.

**Definition 2.8.** On a manifold with metric  $g_{\mu\nu}$  and Riemann tensor  $R^\alpha_{\beta\gamma\delta}$  [15]:

- ★ The Ricci scalar gives the average local curvature:

$$R := R^\mu_\mu = g^{\mu\nu} R_{\mu\nu}$$

- ★ The normalised Ricci curvature for an  $n$ -dimensional manifold is:

$$\kappa_{\text{Ricci}} := \frac{R}{n(n-1)} \tag{2}$$

- ★ The Kretschmann scalar gives a total curvature strength:

$$\kappa_{\text{Kretsch}} := R^{\alpha\beta\gamma\delta} R_{\alpha\beta\gamma\delta} \tag{3}$$

Before concluding this section, it is worth emphasising that Christoffel symbols are also used to derive the paths of motion for freely moving particles in curved spacetime. These trajectories, known as geodesics, represent paths that minimise arc length in a finite region of spacetime. Geodesic paths are obtained by solving a second-order differential equation, which is parametrised in terms of an affine parameter. Here, an affine parameter refers to a variable quantity that can be used to parametrise the geodesic equation in a way which leaves the RHS null [15].

**Definition 2.9.** let  $\lambda$  parametrise the path  $x^\mu = x^\mu(\lambda)$ . Then,  $x^\mu$  is a geodesic if it satisfies the geodesic equation [15]:

$$\ddot{x}^\alpha(\lambda) + \Gamma_{\mu\nu}^\alpha \dot{x}^\mu(\lambda) \dot{x}^\nu(\lambda) = f(\lambda) \dot{x}^\alpha(\lambda),$$

with  $\dot{x}^\mu(\lambda) := \frac{d}{d\lambda}x^\mu(\lambda)$ , and  $f(\lambda)$  a function of the parameter  $\lambda$ . Moreover, if  $\lambda$  is an affine parameter, then the geodesic equation can be written as:

$$\ddot{x}^\alpha(\lambda) + \Gamma_{\mu\nu}^\alpha \dot{x}^\mu(\lambda) \dot{x}^\nu(\lambda) = 0. \quad (4)$$

The significance of this expression comes from the fact that in GR, light always follows geodesic paths. Hence, studying the geodesics in spacetime will be fundamental to our understanding of how light from distant BHs reaches us, and how its path is affected by a BH's gravitational attraction. In particular, a shadow will be formed in the absence of incoming light from some region on our sky. Deriving the shape and size of the region from which light is unable to reach us is the stepping stone to constructing a BH shadow [47].

## 2.2 General Relativity

Formulating a theory of gravity without the explicit mention of forces is no easy task and warrants an alternative formulation altogether. This formulation must comply, in ordinary scales, with Newton's Law of gravitation, while also generalising well to other cases (clearly). Moreover, any theory which attempts to empirically describe the behaviour of natural phe-

nomena must be based on some initial assumptions.

In 1915, Albert Einstein based his theory of relativity on two fundamental postulates [15]:

- ⌘ The laws of physics are the same in all inertial frames of reference, and
- ⌘ The speed of light propagating in vacuum is the same in all inertial frames of reference.

To this extent, a frame consists of an origin which is paired with a basis for 3-space and a time axis. This allows us to define inertial frames below.

**Definition 2.10.** An inertial frame is a coordinate system within which Newton's law of inertia holds. This law of inertia states that: in the absence of a net external force, a free particle is either at rest or moving with a constant velocity [64].

Returning to our coveted postulates, the first is motivated by the fact that experimentally, the acceleration due to gravity on a body is found to be independent of its mass (in the absence of exterior resistive forces such as air resistance). Moreover, the effects of gravity are fundamentally indistinguishable from those of any inertial acceleration – this postulate is often referred to as the Equivalence Principle [2, 68]. The second postulate was inspired by the fact that Maxwell's equations for electromagnetic waves predict that electromagnetic radiation propagates at the speed of light,  $c$ , independent of the observer's velocity. Indeed, this speed is given by the inverse-product-root of the permittivity,  $\epsilon_0 = 8.854 \times 10^{-12} \text{ F m}^{-1}$ , and the permeability,  $\mu_0 = 4\pi \times 10^{-7} \text{ N A}^{-2}$ , of free space. This yields the special constant [38]:

$$c = \frac{1}{\sqrt{\epsilon_0 \mu_0}} = 299,792,458 \text{ m s}^{-1}$$

By exploring these postulates in the framework defined by manifolds and differential geometry, Einstein devised his coveted theory of GR. This theory provides us with the

Einstein Field Equations [2, 15, 68].

**Definition 2.11.** The Einstein Field Equations (EFEs) are a set of 10 coupled second-order non-linear partial differential equations, given by:

$$G_{\mu\nu} + \Lambda g_{\mu\nu} = \kappa T_{\mu\nu}, \quad (5)$$

and whose solutions are the components of the metric tensor  $g_{\mu\nu}$ .

Here,  $G_{\mu\nu}$  is the Einstein tensor found in definition 2.7,  $\Lambda$  is the cosmological constant,  $\kappa = \frac{8\pi G}{c^4}$  is a coupling constant, and  $T_{\mu\nu}$  is the energy–momentum tensor.

As the name suggests, the energy-momentum tensor takes into account the continuous matter distributions and fields which give rise to energy, momentum and pressure in the universe. These quantities will all influence the curvature of spacetime as discussed in [15, 68]. Importantly, the law of energy conservation is verified from the fact that the divergence of  $T_{\mu\nu}$  is locally zero.

On the other hand, the cosmological constant represents the vacuum energy density that is present uniformly throughout the universe. A value of  $\Lambda > 0$  corresponds to an expanding universe, while  $\Lambda < 0$  describes a contracting one. Currently, there is a discrepancy on the order of  $10^{120}$  between the theoretical and observed values of this constant. This is known as the cosmological constant problem, which is still an active area of research. A lengthy discussion is provided in [3]; however, this will not be discussed further.

Although the EFEs can describe the motion of any body in spacetime, we shall only be concerned with the behaviour of photons (light). Formally, a photon is a massless fundamental boson which allows us to observe the world around us – it is the main carrier of information for phenomena originating from the cosmos. The fact that photons are massless leads to their ability to move along lightlike (null) geodesics. Despite their zero mass, they

still possess a non-zero linear momentum, and a resultant energy arising from it [38].

Another important point of discussion involves the line element in spacetime. This quantity will give a measure of the distance between two events in 4-space. The magnitude of the line element allows us to define three distinct types of paths:

$$ds^2 = g_{\mu\nu} dx^\mu dx^\nu \begin{cases} > 0, & \text{for spacelike paths} \\ = 0, & \text{for lightlike paths} \\ < 0, & \text{for timelike paths} \end{cases}$$

Intuitively, a timelike path is one along which the velocity of an object is  $< c$ . A lightlike path is followed by a massless body travelling with  $c$ , and a spacelike path requires a body to be moving at a superluminal speed  $> c$ . This classification is essential to our ability to characterise the trajectories of light and determine the causal structure of spacetime [15, 38].

We should emphasise that in our particular study of null geodesics, explicit use of the EFEs will not be mandatory. Instead, we may wish to consider the energetics of the system. This approach has seen a surge of popularity in the past few decades due to its ability to exploit a system's symmetries very effectively. Special mention can be made to the Lagrangian formulation, which centres around using the scalar  $\mathcal{L}$ , called the Lagrangian. By obtaining this quantity and solving the Euler-Lagrange Equations (defined below), we can equivalently derive the equations of motion for the spacetime [64, 68].

**Definition 2.12.** Let  $x^\mu$  be a set of coordinates in spacetime. The Lagrangian of a massless photon is given by:

$$\mathcal{L}(x^\mu, \dot{x}^\mu) := \frac{1}{2} g_{\mu\nu} \dot{x}^\mu \dot{x}^\nu$$

This scalar satisfies the Euler-Lagrange Equations (ELEs):

$$\frac{d}{d\lambda} \left( \frac{\partial \mathcal{L}}{\partial \dot{x}^\mu} \right) - \frac{\partial \mathcal{L}}{\partial x^\mu} = 0 \quad (6)$$

Alternatively, we can adopt an equivalent formulation called the Hamiltonian, denoted as  $\mathcal{H}$ . Like the Lagrangian, the Hamiltonian is a scalar function that, when applied to Hamilton's equations of motion, yields the system's dynamics. However, this approach is often less straightforward in practice, which has historically limited its widespread use [15, 24]. This will find use in subsequent sections.

**Definition 2.13.** The Hamiltonian,  $\mathcal{H}$ , of a system is defined in terms of the Legendre transformation of the system Lagrangian  $\mathcal{L}(x^\mu, \dot{x}^\mu)$ :

$$\mathcal{H}(p_\mu, \dot{x}^\mu) := \sum_\mu p_\mu \dot{x}^\mu - \mathcal{L}, \quad (7)$$

where the conjugate momenta,  $p_\mu$ , are obtained from:

$$p_\mu := \frac{\partial \mathcal{L}}{\partial \dot{x}^\mu}$$

## 2.3 Symmetries and Killing vector fields

In pure mathematics, the concept of symmetry extends far beyond the study of shapes. Rather, a symmetry is understood as a coordinate transformation that leaves a system invariant. Specifically, a system is said to be invariant under a transformation if its equations of motion (derived from the appropriate laws of motion) remain unchanged when expressed in the new coordinate system [15].

There is a deep connection between the symmetries of an isolated system and the physical quantities that remain constant over time,  $t$ , within it — referred to as conserved quantities. The correspondence between symmetries and conservation laws was formulated by Noether in 1918, and is stated as follows [64]:

**Definition 2.14.** Consider a system with Lagrangian,  $\mathcal{L}(x^\mu, \dot{x}^\mu; t)$ . If the action,

$$S := \int \mathcal{L}(x^\mu, \dot{x}^\mu; t) dt$$

remains invariant under the infinitesimal transformation of the coordinates  $x^\alpha \rightarrow x^\alpha + \delta x^\alpha$ , then there exists a conserved quantity associated with this symmetry.

This theorem is mainly applied (but not restricted!) to three physical applications:

- ⌘ If a system is invariant under time translations, then it is said to be isolated, and the total energy is conserved.
- ⌘ If an isolated system is invariant under spatial translations, then the linear momentum is conserved.
- ⌘ If an isolated system is invariant under rotations, then the angular momentum is conserved.

These properties can also be deduced from the ELE defined in equation 6. If  $\mathcal{L} \neq \mathcal{L}(x^\alpha)$ , then:

$$\frac{\partial \mathcal{L}}{\partial x^\alpha} = 0 \implies \frac{d}{d\lambda} \left( \frac{\partial \mathcal{L}}{\partial \dot{x}^\alpha} \right) = 0,$$

which implies that the conjugate momentum  $p_\alpha := \frac{\partial \mathcal{L}}{\partial \dot{x}^\alpha} = \text{constant}$ .

In practice, conservation laws are often invaluable since they have the power to greatly simplify the derivation of the equations of motion, and eventually, integrate to find the geodesics of the spacetime. In many cases, finding an exact solution without exploiting symmetries is impossible. One thing to note, however, is that in curved spacetime, symmetries often manifest themselves in more subtle manners. Instead of coordinate transformations, we will describe symmetries in terms of isometric maps on spacetime.

To formally introduce the notion of symmetries, we consider mappings from a manifold onto itself. In particular, let  $\mathcal{M}$  be a real manifold, and let  $\phi_\alpha : \mathcal{M} \rightarrow \mathcal{M}$  be a one-parameter

group of isometries such that  $\phi_\alpha^* g_{\mu\nu} = g_{\mu\nu}$ . Then, the vector field  $\xi^\mu$  that generates the transformation  $\phi_\alpha$  is called a Killing vector field. Equivalently, the following definition is also used [15, 68]:

**Definition 2.15.** The vector,  $\xi^\mu$ , is said to be a Killing vector if it satisfies Killing's equation:

$$L_\xi g_{\mu\nu} := \nabla_\beta \xi_\alpha + \nabla_\alpha \xi_\beta = 0, \quad (8)$$

where  $L$  is called the Lie derivative.

Killing vector fields are crucial because they indicate if a spacetime is independent of some parameter, even though the metric might not be expressed in a coordinate system that is explicitly independent of it. This leads to the coordinate being cyclic in the Lagrangian, which also results in the conservation of its respective conjugate momentum [68].

Fortunately, most spacetimes are derived under the assumption that certain symmetries already exist. Without these symmetries, very few solutions to the EFEs exist. Two important examples of symmetric spacetime structures are included in the two definitions below.

**Definition 2.16.** A spacetime,  $g_{\mu\nu}$ , is said to be stationary if it admits a timelike Killing vector  $\partial_t$ , for some timelike coordinate  $t$ . That is,  $\partial_t g_{\mu\nu} = 0$ .

Equivalently, there exists a coordinate system such that  $g_{\mu\nu} \neq g_{\mu\nu}(t)$ .

Intuitively, a stationary spacetime will "look the same" on every  $t = \text{constant}$  slice of spacetime, i.e. the metric tensor will not change with time. In this case, the total energy along a photon path will be conserved as previously discussed. The following is a stronger form of symmetry:

**Definition 2.17.** A spacetime,  $g_{\mu\nu}$ , is said to be static if it is stationary, and the Killing vector  $\partial_t$  is hypersurface orthogonal to surfaces of  $r = \text{constant}$ .

This definition necessitates a brief discussion on hypersurface orthogonality, which was stated directly from [68].

**Definition 2.18.** A vector  $\xi^a$  is said to be hypersurface orthogonal if, and only if, it satisfies:

$$\xi_{[a} \nabla_b \xi_{c]} := \xi_a \nabla_b \xi_c - \xi_a \nabla_c \xi_b + \xi_b \nabla_c \xi_a - \xi_b \nabla_a \xi_c + \xi_c \nabla_a \xi_b - \xi_c \nabla_b \xi_a = 0 \quad (9)$$

In other words, a spacetime is said to be static if  $\partial_t$  is orthogonal on every surface defined by the slice  $r = \text{constant}$ . Additionally, hypersurface orthogonality can also be described as the property of a vector field being irrotational in the classical sense, since the condition  $\xi_{[a} \nabla_b \xi_{c]} = 0$  is equivalent to the vanishing of the vorticity tensor  $\omega_{\mu\nu} := \nabla_{[\mu} \xi_{\nu]}$  [15], cf. diagram 15 for the effects of vorticity on the radial geodesics in non-static spacetimes.

In summary, the symmetries of a metric tensor are most often in the form of time, rotational, or translational invariance. This leads to the conservation of a corresponding conjugate momentum. Without these conserved quantities, solving the geodesic equations would be difficult, if not impossible, as there would be too few constants of motion to integrate the equations analytically. Fortunately, most spacetimes under consideration will be fully integrable, meaning that they possess enough symmetries to allow for exact solutions of geodesic motion.

## 2.4 So, What are BHs?

What distinguishes BHs from every other object in the universe is their extremely compact mass distribution. Every solid celestial body has an associated critical radius – dependent on its angular momentum, mass, and charge – beyond which it will be classified as a BH [17]. In pop culture, a BH is defined as a region in spacetime where the gravitational field

is so strong that not even light can escape. While this fact is generally true, it is not stated precisely.

In general, a BH is characterised by the presence of (at least) two distinct regions: an event horizon and a gravitational singularity [15].

**Definition 2.19.** An event horizon is a hypersurface that partitions spacetime into two regions: those that are connected to future null infinity by a timelike curve, and those that are not. These two regions are said to be *causally disconnected*.

While this definition captures the intuitive notion of this boundary, a more rigorous definition can be given in terms of the causal structure of spacetime, or visually using Carter-Penrose diagrams [46]. This hypersurface has a few interesting properties:

- ⌘ The Kretschmann scalar remains finite at the horizon, indicating that this is only an apparent singularity – this can be removed through a coordinate transformation.
- ⌘ The timelike component of the metric tensor,  $g_{tt}$ , is zero on the horizon. For this reason, event horizons are often referred to as null hypersurfaces.
- ⌘ It is a one-way membrane. While infalling observers can cross past the horizon, neither timelike nor null trajectories can escape the interior. Doing so will require an escape velocity greater than the speed of light (spacelike path).
- ⌘ It will take an infalling observer a finite amount of proper time to cross its surface, but a distant observer will perceive this event to take infinitely long. This phenomenon is known as gravitational time dilation [15].

In 1969, Roger Penrose showed in his weak cosmic censorship conjecture that every gravitational singularity that has resulted from gravitational collapse is hidden behind a so-called event horizon [45, 68]. In the words of Rindler, an event horizon is "a frontier between things observable and things unobservable" [55].

**Definition 2.20.** A gravitational (curvature) singularity is a set of points in spacetime on which any of the curvature invariants  $\{\kappa_{\text{Kretsch}}, \kappa_{\text{Ricci}}, R, p\}$  become infinite.

Physically, this corresponds to a location at which the density of collapsed matter becomes infinite, at which point the laws of physics as we know them break down. The properties of such singularities remain an active area of research to date [38]. Note that this singularity cannot be removed by a change of coordinates, as it is invariant to transformations.

To paint a clearer picture, we shall consider the simplest BH example – a non-rotating and uncharged mass,  $M$ , embedded in a static universe. Sean Carroll in [15] derives the Kretschmann scalar, given as a function of the radial distance from the centre of such a BH, as:

$$\kappa_{\text{Kretsch}}(r) = \frac{48G^2M^2}{r^6c^4}.$$

Moreover, the event horizon of this BH is found at  $r = \frac{2GM}{c^2}$ . In figure 2, the value of the Kretschmann scalar is plotted against radial distance. Note that this diagram is not drawn to scale; rather, it simply serves to give a rough idea of the spacetime curvature we expect to see around BHs.

A final comment can be added to conclude this introductory subsection on BHs. Wheeler [38] was the first to point out the following theorem:

**Theorem 2.1.** (No-Hair Theorem [15, 19])

Stationary, asymptotically flat BH solutions to GR coupled to electromagnetism that are non-singular outside the event horizon are fully characterised by the parameters of mass  $M$ , electric  $Q$  and magnetic  $P$  charge, and angular momentum  $J$ .

In essence, this theorem states that for BHs whose spacetime is time-independent and spatially Euclidean as  $r \rightarrow \infty$ , the only four quantities needed to fully describe their external gravitational fields are  $(M, Q, P, J)$ . By 'hair', we understand information regarding the

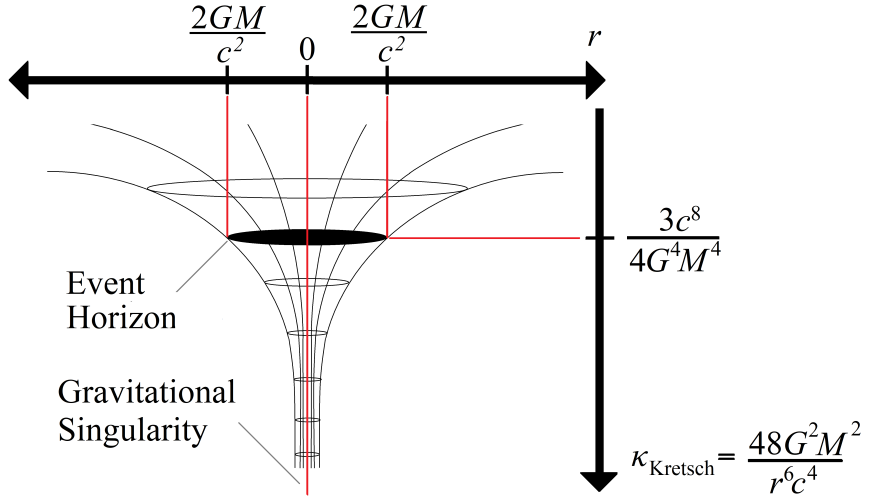


Figure 2: The Kretschmann scalar as a function of radial distance, for a static and uncharged (Schwarzschild) BH. This plot is not to scale. The 3d funnelling of spacetime arises from the central mass, which is hidden by the event horizon.

gravitationally collapsed matter found beyond the event horizon. This includes information relating to the matter distribution and composition – which is lost [15]. In table 1, an account of the BH spacetimes described by all combinations of the  $(M, Q, P, J)$  parameters is given. A detailed discussion on this topic is found in [19].

	Non-rotating ( $J = 0$ )	Rotating ( $J \neq 0$ )
Uncharged ( $Q = 0$ and $P \neq 0$ )	Schwarzschild	Kerr
Charged ( $Q \neq 0$ or $P \neq 0$ )	Reissner–Nordström	Kerr–Newman

Table 1: Table showing the classification of stationary and asymptotically flat BH spacetimes.

---

### 3 BH Shadows... Finally

Throughout the following chapters, we will adopt several important assumptions regarding the nature of the BHs and the surrounding universe. These will be essential for our observation of BH shadows and will not significantly skew our results from reality. Specifically, we assume that [47]:

- ⌘ The central BH will possess the only non-negligible mass in the universe, and will therefore give rise to the only source of gravitational fields. This is only stated to ensure that conventional BH spacetimes can be used.
- ⌘ Observers, such as us, are located sufficiently far from the BH. Here, the notion of "sufficiently far" will depend on the type of BH being considered.
- ⌘ The background sky will consist of a dense uniform distribution of light sources such as stars. Moreover, no additional light sources lie between an observer and a BH. This maximises the clarity of the shadow.

So far, we have built up our discussion in a way which allows us to describe how mass influences the curvature of spacetime. In the words of John Wheeler [38],

*"Spacetime tells matter how to move; matter tells spacetime how to curve."*

This curvature, as encoded into the Riemann tensor and used to describe the null trajectories of light, will imply that BHs deviate the paths of light from an otherwise straight line in Euclidean space. In some cases, the gravitational pull of a BH can even be strong enough to trap light into a circular orbit around it. Light that has become trapped in this manner cannot reach us on Earth. Hence, we have no information about the source from which they originated.

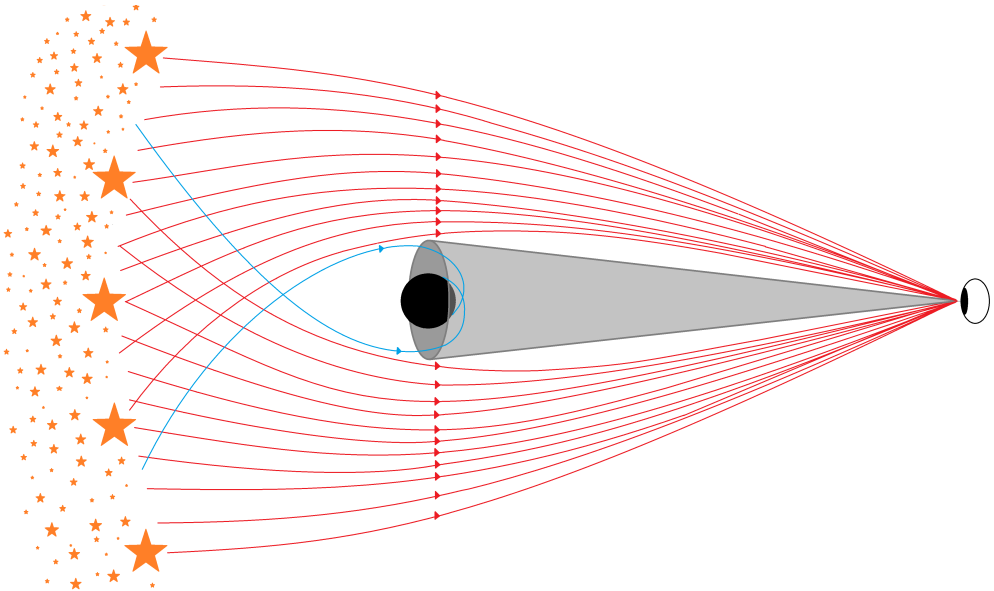


Figure 3: Light rays (in red) received by an observer from distant stars after being gravitationally lensed by a static and non-rotating BH. In the grey shaded cone, no incoming photons from the stars can be received due to the BHs strong gravitational field (in blue).

In figure 3, we illustrate an observer receiving light from light sources located behind a distant BH. Crucially, no photons are received by the observer if their paths pass through the shaded region. Any photon emitted from the light sources that passes too close to the BH becomes trapped, forever unable to reach the observer. This creates a dark region in the sky having an angular size larger than the BH’s event horizon [26, 47]. From the figure, we note that the second, third, and fourth stars emit rays that reach the observer from both above and below the BH. By extending the system to 3d, such rays will create a ring-like image around the BH, as seen in figure 4.

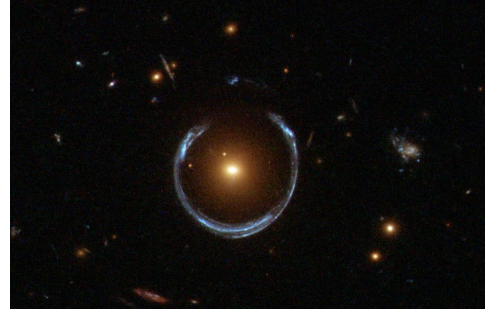


Figure 4: An image of galaxy LRG 3-757 gravitationally lensing a background blue galaxy. The perfect alignment of these two galaxies allows us to receive light from the distant galaxy in a ring all around LRG 3-757 [22].

---

To proceed further, we must establish a method for characterising incoming photons. A useful approach is to reverse the flow of time and treat any photons arriving at the observer from the distant stars as instead being emitted from the observer toward these light sources (past-emitted). This time reversal operation only acts to reverse the direction of motion for incoming photons. Keeping Figure 5 in mind, the paths of all possible past-emitted photons fall into three distinct categories [47]:

- ⌘ Category 1, in blue: Those that reach the distant light sources. Under standard time flow, these photons are emitted by the stars and received by the observer. Hence, Category 1 photons create an image on the observer's sky.
- ⌘ Category 2, in green: Those that fall incident on BH's event horizon. Under standard time flow, these will appear to originate from the surface of the event horizon! This is strictly prohibited, and hence, Category 2 photons are not seen by an observer. This corresponds to a dark region in the sky.
- ⌘ Category 3, in orange: At some critical emission angle, photons may neither impinge on the surface of the BH, nor escape to infinity. Rather, such photons will spiral towards some circular orbit around the BH asymptotically, forming what is known as a closed circular photon trajectory. Under standard time flow, such light will appear to originate from the closest possible region near a BH without being lost to the event horizon.

This visual analysis reinforces the existence of a so-called "light cone" inside which no photons can be received by an observer. This results in a dark region on the sky of the observer, formally defining the shadow of a BH [47]. The boundary of a BH shadow is traced by photons that were emitted by a distant light source before spiralling into some unstable photon orbit asymptotically. These photons are then re-emitted towards an observer through perturbative processes and are observed to arrive tangentially to the vertex of the light cone. This gravitational lensing phenomenon magnifies the apparent size of the photon sphere considerably! The angular sizes of key BH features are illustrated in Figure 6.

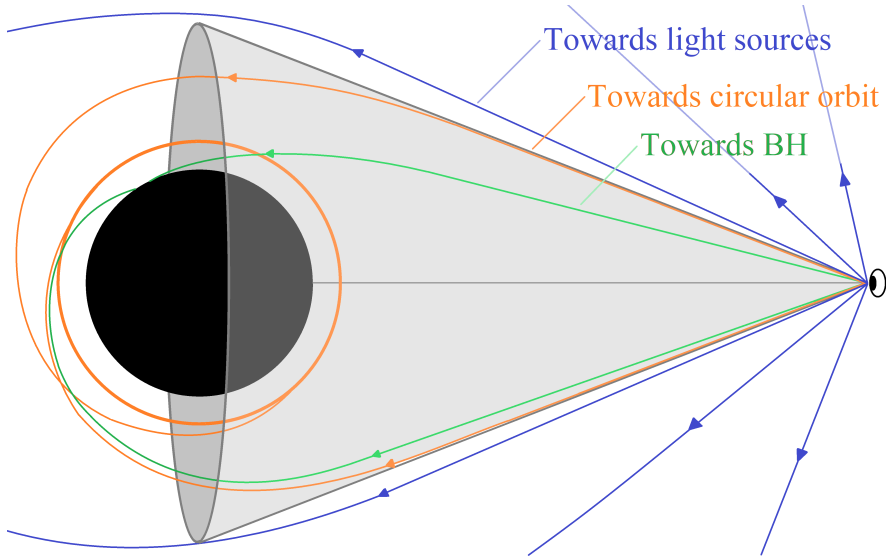


Figure 5: The three categories of past-emitted photons emitted by an observer. Photons emitted inside the grey cone will be absorbed by the BH, tangential at the vertex will spiral into a circular orbit, and outside the cone will escape to infinity. Diagram adapted from figure 1 in [47].

**Definition 3.1.** The shadow of a BH is a region of an observer's sky where light coming from distant light sources is completely absent due to the presence of the BH. The boundary of this shadow is determined by the set of past-emitted photon trajectories asymptotically approaching unstable photon orbits.

**Remark 3.1.** In reference to the images of M87\* and Sagittarius A\* in figures 1a and 1b, their shadows correspond to the central dark regions that are surrounded by a bright ring of light. The size of the shadow is precisely the radius of the base of the projected light cone in figure 6.

Unfortunately, photon orbits around BHs exist in a broad range of shapes, so few general comments on their structure can be made. Nonetheless, an important universal condition these must satisfy is that they should be unstable with respect to radial perturbations. This will allow light to escape from the bound orbit stochastically and reach the observer. While the origin of the photon sphere is not important for our discussion, detailed models incorporating higher-order images, accretion disk emission, and blurring effects are discussed in

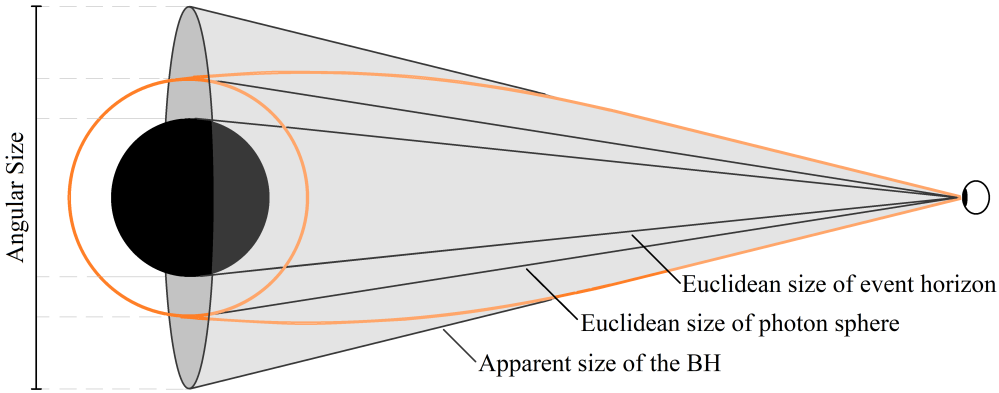


Figure 6: The angular size of the event horizon and photon sphere as projected onto an observer’s sky assuming a Euclidean geometry. In a general BH spacetime, the phenomenon of light bending will lead to photons having a curved path. Photons comprising the BH shadow will appear to arrive from an area much larger than the photon sphere itself. Diagram adapted from figure 3 in [47].

[25]. In particular, Gralla et al provide accurate simulations for the shadow of M87\*.

The term "Black Hole Shadow" was adopted in direct analogy to the Moon eclipsing the Sun – just as the Moon blocks light from the Sun, a BH blocks light from background sources, creating a dark region on the observer’s sky. Although the shadow region has a well-defined angular size, it should not be confused with the event horizon; rather, it corresponds to the projection of the photon region on an observer’s sky, which is typically much larger compared to the event horizon.

Unbeknownst to many, the study of BH shadows can be traced back to the early 1970s. In fact, the first realistic images of shadows were generated by Luminet back in 1979. His most fascinating image is shown in 7, and is taken from his original work in [36]. While shadows in stationary BH spacetimes are well-described theoretically, the introduction of cosmological expansion complicates the system considerably. At large scales, this expansion will affect the trajectories of light in addition to the background gravitational attraction. These issues will be tackled appropriately at a later stage, as we shall first start by deriving the shadows for some idealised spacetimes. This will provide us with the necessary tools and

---

experience to tackle the cosmological case.

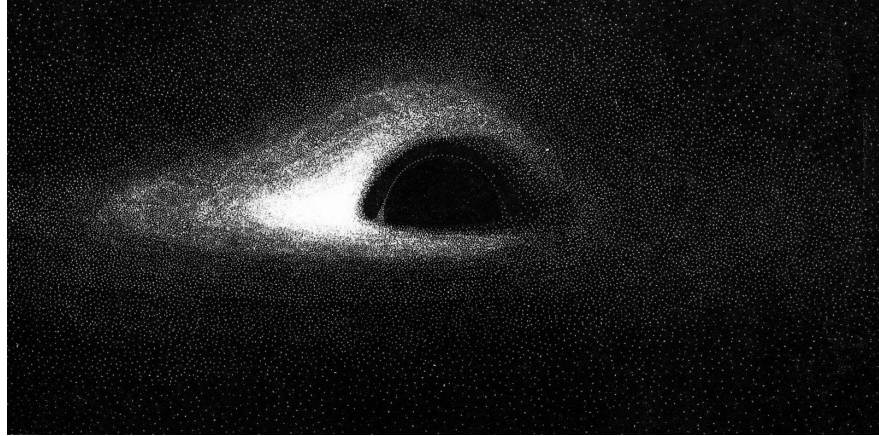


Figure 7: A Schwarzschild BH surrounded by a thin accretion disk, viewed from an inclination of  $10^\circ$  above the disk's plane. The inner bright ring corresponds to the projection of the unstable photon sphere. The diagram was generated through a primitive computer simulation in 1979 [36].

**Remark 3.2.** Newtonian gravitation (NG) fails to accurately describe photon trajectories because it lacks the relativistic curvature terms that lead to unstable photon orbits in GR. Hence, NG cannot be used for our analysis of photon trajectories in the strong gravitational regime. This necessitates the use of GR.

---

## 4 BH shadows in static and spherically symmetric spacetimes

In the following sections, we define  $m := \frac{GM}{c^2}$  to be the geometric mass and assume the geometric units  $G = c = 1$  [38]. We will start our discussion on BH shadows by discussing two elementary examples – Schwarzschild and the Reissner-Nordström BHs. For both cases, only one general derivation for the angular size of the BH shadow is required.

### 4.1 Derivation of general expression

The general form of a spherically symmetric metric is the following [15, 47, 52]:

$$ds^2 = g_{tt}(r, t)dt^2 + g_{rr}(r, t)dr^2 + g_\Omega(r, t)d\Omega^2, \quad (10)$$

where  $d\Omega^2 = (d\theta^2 + \sin^2 \theta d\phi^2)$  is the metric on the 2-sphere  $\mathbb{S}^2$ . As usual,  $-g_{tt}(r, t)$ ,  $g_{rr}(r, t)$  and  $g_\Omega(r, t)$  are all positive functions in the timelike region of spacetime, and are dependent on the radial coordinate  $r = \sqrt{x^2 + y^2 + z^2}$  and coordinate time  $t$ .

According to definition 2.17, static spacetimes are independent of coordinate time. Thus,

$$g_{tt}(r, t) = g_{tt}(r), \quad g_{rr}(r, t) = g_{rr}(r), \quad g_\Omega(r, t) = g_\Omega(r).$$

Furthermore, due to the spherical symmetry of the spacetime, it is very convenient to study its photon orbits only along the equatorial plane with  $\theta = \frac{\pi}{2}$ . The photon orbits will remain unchanged along every direction of observation [15, 17, 47].

We begin our study of photon trajectories in this general spacetime by considering the system Lagrangian:

$$\begin{aligned} \mathcal{L} &= \frac{1}{2}g_{\mu\nu}\dot{x}^\mu\dot{x}^\nu = \frac{1}{2}\left[g_{tt}(r)\dot{t}^2 + g_{rr}(r)\dot{r}^2 + g_\Omega(r)\dot{\Omega}^2\right] = 0 \\ \implies \mathcal{L} &= \frac{1}{2}\left[g_{tt}(r)\dot{t}^2 + g_{rr}(r)\dot{r}^2 + g_\Omega(r)\dot{\phi}^2\right] = 0, \end{aligned} \quad (11)$$

where we have simplified  $\dot{\Omega}^2 = \dot{\theta} + \sin^2 \theta \dot{\phi}^2 \equiv \dot{\phi}^2$  since  $\theta = \frac{\pi}{2} = \text{constant}$ . Ultimately, our Lagrangian approach will yield results identical to those obtained by solving the EFEs directly. However, the issue with using the EFE approach is that we are not concerned with the specific functions describing  $g_{tt}$ ,  $g_{rr}$ , and  $g_\Omega$ . Rather, we are looking for a general approach which bypasses the need to manipulate these functions [47].

One may note that since  $t$  and  $\phi$  do not appear in the system Lagrangian, then their respective conjugate momenta:

$$p_\phi := \frac{\partial \mathcal{L}}{\partial \dot{\phi}} = g_\Omega(r)\dot{\phi} \quad \text{and} \quad p_t := \frac{\partial \mathcal{L}}{\partial \dot{t}} = g_{tt}(r)\dot{t}, \quad (12)$$

will be constants of motion (see discussion in subsection 2.3). These constants are often defined as the total angular momentum  $L$  and the energy at infinity  $E$ , respectively [17, 68]. These are related through:

$$L := p_\phi = g_\Omega(r)\dot{\phi} \quad \text{and} \quad E := -p_t = -g_{tt}(r)\dot{t}. \quad (13)$$

**Remark 4.1.** It is also possible to relate  $\dot{r}$  with its conjugate momentum,  $p_r$ , however, this will not be a constant of motion due to its explicit presence in the components of the metric – it is not a cyclic coordinate.

This spherically symmetric spacetime allows us to extract yet another constant of motion, which will complete the full set of integration constants required to obtain the lightlike geodesics. To obtain this third constant of motion, we may consider the integral of the line element in equation 10 for null geodesics [15, 47]:

$$0 = \left( \frac{ds}{d\lambda} \right)^2 = g_{tt}(r)\dot{t}^2 + g_{rr}(r)\dot{r}^2 + g_\Omega(r)\dot{\phi}^2. \quad (14)$$

By substituting the constants of motion from 13, into the above expression, we obtain [47]:

$$\begin{aligned}
 0 &= g_{tt}(r) \left( -\frac{E}{g_{tt}(r)} \right)^2 + g_{rr}(r) \dot{r}^2 + g_\Omega(r) \dot{\phi}^2 \\
 &= \frac{E^2}{g_{tt}(r)} \frac{1}{\dot{\phi}^2} + g_{rr}(r) \frac{\dot{r}^2}{\dot{\phi}^2} + g_\Omega(r), \quad \text{dividing by } \dot{\phi}^2 \\
 \frac{\dot{r}^2}{\dot{\phi}^2} &= -\frac{E^2}{g_{rr}(r)g_{tt}(r)} \frac{1}{\dot{\phi}^2} - \frac{g_\Omega(r)}{g_{rr}(r)}, \quad \text{dividing by } g_{rr}(r) \\
 \left( \frac{\dot{r}^2}{\dot{\phi}^2} \right) &= -\frac{E^2}{g_{rr}(r)g_{tt}(r)} \left( \frac{g_\Omega(r)}{L} \right)^2 - \frac{g_\Omega(r)}{g_{rr}(r)} \\
 \implies \left( \frac{dr}{d\phi} \right)^2 &= -\frac{g_\Omega(r)}{g_{rr}(r)} \left( \frac{g_\Omega(r)E^2}{g_{tt}(r)L^2} + 1 \right), \quad \text{where } \frac{\dot{r}}{\dot{\phi}} = \frac{dr}{d\lambda} \frac{d\lambda}{d\phi} = \frac{dr}{d\phi}. \tag{15}
 \end{aligned}$$

Note that  $\dot{\phi} \neq 0$  for any non-radial orbit, so dividing by  $\dot{\phi}$  does not cause an issue. From here, we can continue with more assumptions based on the properties of circular orbits. In particular, we can use the condition for instantaneous circular motion  $\dot{r} = 0$ . However, in our case, since equation 15 does not explicitly feature  $\dot{r} := \frac{dr}{d\lambda}$ , we must look at this condition from a different angle [47].

Consider a photon being emitted by an observer in the general direction of the BH, without necessarily being captured into circular orbit (see figure 8). In terms of the photon's radial distance from the BH, we see that this quantity reaches some minimum value of  $r = R$ , before receding to infinity. At the instant in time when  $r = R$ , the rate of change of the radial distance with respect to the azimuthal angle  $\phi$  will vanish. Here, the azimuthal angle gives the direction towards the equatorial photon from the centre of the BH [26, 47]. Formally, this implies that  $\frac{dr}{d\phi}|_{r=R} = 0$ , so that at  $r = R$ , equation 15 yields:

$$0 = -\frac{g_\Omega(R)}{g_{rr}(R)} \left( \frac{g_\Omega(R)E^2}{g_{tt}(R)L^2} + 1 \right).$$

Now, given that both  $g_\Omega(R)$  and  $g_{rr}(R)$  are strictly positive, we may deduce that:

$$\begin{aligned}
 \frac{g_\Omega(R)E^2}{g_{tt}(R)L^2} + 1 &= 0 \\
 \implies \frac{-g_{tt}(R)}{g_\Omega(R)} &= \frac{E^2}{L^2} =: \frac{1}{b^2} = \text{constant}, \tag{16}
 \end{aligned}$$

where we have introduced the impact parameter  $b$ , suitably. Its value will be important in several upcoming results. In general, we may further define the function:

$$h(r)^2 := \frac{g_\Omega(r)}{-g_{tt}(r)}, \quad \text{with} \quad h(R) = b. \quad (17)$$

This allows us to finally hone-in and tackle the problem of finding an expression for the angular size of a static BH.

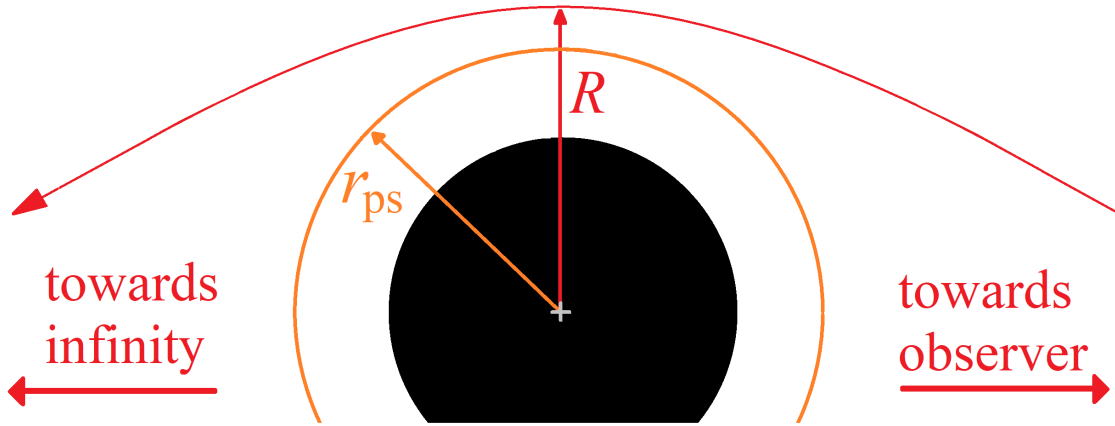


Figure 8: The trajectory of a photon being emitted towards a BH by an observer. In the strong gravitational regime, the photon's geodesic path will deform increasingly before receding away towards infinity. At some azimuthal angle with respect to the BH, the radial distance will reach a minimum at  $r = R$ . If  $R = r_{\text{ps}}$ , the photon will become trapped in a circular orbit.

Consider a static observer located at some fixed radial coordinate  $r = r_O$ . By using figure 9 as reference, we may deduce that a photon's distance of closest approach is related to its angle of emission by [47]:

$$\begin{aligned} \tan \alpha &= \sqrt{\frac{g_\Omega}{g_{rr}} \frac{d\phi}{dr}} \Big|_{(\phi_O, r_O)} \\ \implies \cot^2 \alpha &= \frac{g_{rr}(r)}{g_\Omega(r)} \left( \frac{dr}{d\phi} \right)^2 \Big|_{r=r_O}. \end{aligned}$$

Once again invoking equation 15 at  $r = r_O$ , we obtain:

$$\begin{aligned} \cot^2 \alpha &= \frac{g_{rr}(r_O)}{g_\Omega(r_O)} \left[ -\left( \frac{g_\Omega(r_O)}{g_{rr}(r_O)} \right) \left( \frac{g_\Omega(r_O)E^2}{g_{tt}(r_O)L^2} + 1 \right) \right] \\ \csc^2 \alpha \equiv \cot^2 \alpha + 1 &= \frac{g_\Omega(r_O)}{-g_{tt}(r_O)} \frac{E^2}{L^2} \equiv \frac{h(r_O)^2}{h(R)^2} \\ \implies \sin^2 \alpha &= \frac{h(R)^2}{h(r_O)^2}. \end{aligned} \quad (18)$$

We have just obtained an expression for the angle of emission  $\alpha$  of a past-emitted photon using its distance of closest approach,  $R$ . Obviously, we are especially interested in the emission angle of photons which approach the BH asymptotically and remain in some circular orbit at a radial distance  $r = r_{ps}$  [47].

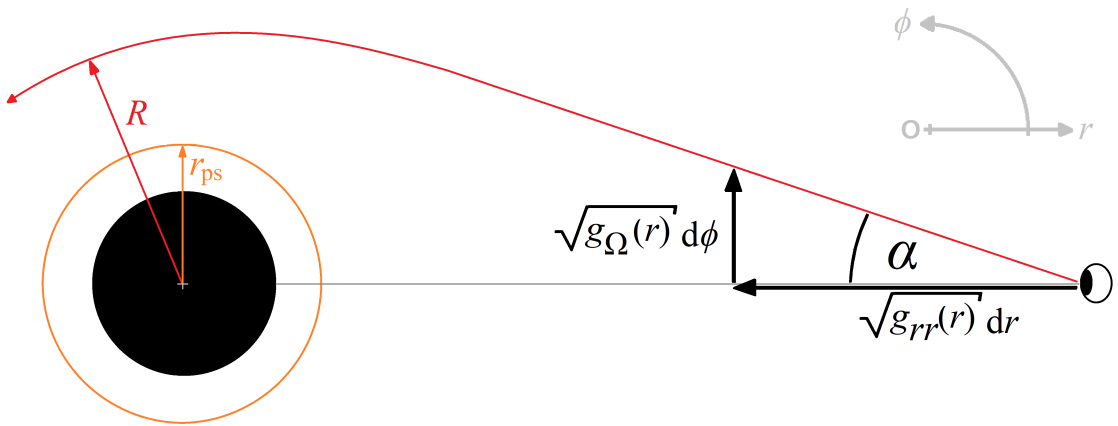


Figure 9: Measure of distance in a spherically symmetric and static spacetime. Given the spherical coordinate system in grey, the spatial scaling factors are obtained from the metric tensor. Diagram adapted from figure 5 in [47].

Past-emitted photons that become trapped in a circular orbit at  $r_{ps}$  possess a precise critical value for their associated impact parameter. Deriving this value of  $b_{cr} := h(r_{ps})$  will allow us to state the angular size of the BH using equation 18 above as:

$$\sin \alpha_{sh} = \frac{h(r_{ps})}{h(r_O)} = b_{cr} \sqrt{\frac{-g_{tt}(r_O)}{g_\Omega(r_O)}} \quad (19)$$

To proceed with the derivation of  $b_{cr}$ , we must emphasise the importance of the geometrical interpretation for the impact parameter  $b$ . Keeping diagram 5 in mind, we note that for

photons in circular orbit, the radial distance remains invariant with respect to the azimuth angle at each point of the motion (not just at an instant). This condition implies that:

$$\frac{dr}{d\phi} \Big|_{r=r_{ps}} = 0 = \frac{d^2r}{d\phi^2} \Big|_{r=r_{ps}}$$

By differentiating equation 15 with respect to  $\phi$  and enforcing the above conditions, we derive the additional constraint [47]:

$$\frac{d}{dr} h(r)^2 \Big|_{r=r_{ps}} = 0. \quad (20)$$

Hence, differentiating equation 17 with respect to  $r$  and equating to zero will allow us to determine the photon sphere radius  $r_{ps}$ . On the photon sphere, using equation 17 again, we find that the corresponding critical impact parameter is given by:

$$b_{cr} := h(r_{ps}) = \sqrt{\frac{g_\Omega(r_{ps})}{-g_{tt}(r_{ps})}} \quad (21)$$

Finally, substituting this value into equation 19 will provide us with the desired BH shadow angular size. This was derived analytically under the conditions that the observer has a fixed location, and that the asymptotically flat spacetime was static and spherically symmetric.

Before moving on to some specific examples, it is useful to approximate the shadow size for distant observers since BHs are typically found at very large cosmic distances. In particular, for asymptotically flat spacetimes with  $g_\Omega(r) = r^2$  (as will be the case for all of our upcoming examples), we must have:

$$-g_{tt}(r), g_{rr}(r) \xrightarrow[r \rightarrow \infty]{} 1.$$

Thus, for large observer distances  $r_O \gg 1$ , we observe:

$$h(r_O) = \sqrt{\frac{r_O^2}{-g_{tt}(r_O)}} \xrightarrow[r_O \gg 1]{} h(r_O) \simeq \sqrt{\frac{r_O^2}{1}} = r_O. \quad (22)$$

This allows us to approximate the angular size of the BH shadow in equation 19 as:

$$\sin \alpha_{sh} = \frac{r_{ps}}{\sqrt{-g_{tt}(r_{ps})}} \sqrt{\frac{-g_{tt}(r_O)}{g_\Omega(r_O)}} \quad (23)$$

as [47]:

$$\sin \alpha_{\text{sh}} \simeq \alpha_{\text{sh}} \simeq \frac{b_{\text{cr}}}{r_0} = \frac{r_{\text{ps}}}{r_0 \sqrt{-g_{tt}(r_{\text{ps}})}}. \quad (24)$$

**Remark 4.2.** In the following subsections, we will determine the angular size of static and spherically symmetric BHs in the following manner:

- ✿ The metric components will be used to derive  $h(r)^2$  using equation 17.
- ✿ Using 20, the radius of the photon sphere will be derived, and the critical impact parameter will be computed using 21.
- ✿ Lastly, equations 23 and 24 will be used suitably to derive the angular size of the BH shadow for an observer at  $r = r_0$ .

## 4.2 BH shadow in Schwarzschild spacetime

As a first example of a spherically symmetric spacetime, we shall consider the solution to the EFEs for the region exterior to an uncharged ( $Q = 0 = P$ ) and non-rotating ( $J = 0$ ) spherical BH embedded in a static universe ( $\Lambda = 0$ ). This solution features the vacuum conditions  $T_{\mu\nu} = 0$  everywhere in spacetime, which lead to the following EFEs:

$$G_{\mu\nu} := R_{\mu\nu} - \frac{1}{2}g_{\mu\nu}R = 0.$$

These allow us to deduce that  $R_{\mu\nu} = 0 = R$ , which follows from a contraction with  $g^{\mu\nu}$ .

It can be shown that the metric tensor that uniquely solves the EFEs under these conditions is given in  $(t, r, \theta, \phi)$  coordinates as [15, 17, 68]:

$$g_{\mu\nu} = -\left(1 - \frac{2m}{r}\right)dt^2 + \left(1 - \frac{2m}{r}\right)^{-1}dr^2 + r^2d\Omega^2, \quad (25)$$

where the uniqueness of the solution follows from Birkhoff's theorem [15].

A quick analysis of the null hypersurfaces in the Schwarzschild spacetime reveals that the event horizon,  $r_{\text{eh}}$ , is located when  $g_{tt}$  vanishes:

$$0 \equiv g_{tt} = -\left(1 - \frac{2m}{r}\right) \implies r_{\text{eh}} := r = 2m.$$

Furthermore, a gravitational singularity is present at the location where the Kretschmann scalar diverges [17]:

$$\kappa_{\text{Kretsch}} = R^{abcd}R_{abcd} = \frac{48m^2}{r^6} \xrightarrow[r \rightarrow 0]{} \infty.$$

Returning to the discussion on BH shadows, we begin by following the procedure presented at the end of the previous subsection. From its definition in equation 17, we find that:

$$h(r)^2 = \frac{r^2}{1 - \frac{2m}{r}}$$

Using this expression in equation 20 will yield the photon sphere radius  $r_{\text{ps}}$  as:

$$\begin{aligned} \frac{d}{dr} h(r)^2 \Big|_{r=r_{\text{ps}}} &= \frac{d}{dr} \left[ \frac{r^2}{1 - 2m/r} \right] \Big|_{r=r_{\text{ps}}} = 0 \\ \frac{2r_{\text{ps}}(1 - 2m/r_{\text{ps}}) - r^2(2m/r_{\text{ps}}^2)}{(1 - 2m/r_{\text{ps}})^2} &= 0 \\ \implies 2r_{\text{ps}}(1 - 2m/r_{\text{ps}}) - r_{\text{ps}}^2(2m/r_{\text{ps}}^2) &= 0 \\ 2r_{\text{ps}} - 4m - 2m &= 0 \\ \implies r_{\text{ps}} &= 0, 3m, \end{aligned} \tag{26}$$

which shows the existence of two possible circular photon orbits. Since the inner photon orbit is located at the gravitational singularity and also obstructed by the event horizon, it will not be considered further. Upon using the result  $r_{\text{ps}} = 3m$  in equation 21, we determine the critical impact parameter as:

$$\begin{aligned} b_{\text{cr}} &= \frac{3m}{\sqrt{1 - 2m/r_{\text{ps}}}} = \frac{3m}{\sqrt{1 - 2m/3m}} \\ \implies b_{\text{cr}} &= 3\sqrt{3}m. \end{aligned}$$

Finally, equation 23 allows us to derive the analytical angular size for the shadow of a Schwarzschild BH as [47]:

$$\alpha_{\text{sh}} = \arcsin \left[ \frac{3\sqrt{3}m}{r_O} \sqrt{1 - \frac{2m}{r_O}} \right]. \quad (27)$$

Using our distant observer approximation from equation 24, under the assumption that  $r_O \gg m$ , we find:

$$\alpha_{\text{sh}} = \frac{3\sqrt{3}m}{r_O}, \quad \text{for } r_O \gg m, \quad (28)$$

which corresponds to the expression derived first by Synge in [61]. It is interesting to note that although the 'surface' of our BH is located at  $r_{\text{eh}} = 2m$ , with a photon sphere at  $r_{\text{ps}} = 3m$ , the actual effective size of the BH, given by  $b_{\text{cr}}$ , is  $3\sqrt{3}m$ . This rather large discrepancy was caused by the light-bending effects in the region of strong gravitational attraction near the BH. Remember that the apparent size of  $3\sqrt{3}m$  is not a physical surface but simply an optical magnification due to lensing.

To visualise the dependence of  $\alpha_{\text{sh}}$  on  $m$  and  $r_O$ , we can turn our attention to the plot in figure 10. In this figure, the size of the BH shadow is not explicitly stated, as it is not of particular importance. Instead, a greater emphasis is placed on visualising the relative sizes of the shadows. From the figure, we may note the strong inverse relationship between the observer distance and angular size, as well as the linear relationship between geometric mass and angular size.

### 4.3 BH shadow in Reissner-Nordström spacetime

Suppose now that our Schwarzschild BH possesses some non-zero overall surface electric charge,  $Q$ . Although this is often viewed as a scenario that is unlikely to ever occur due to the charge-neutral nature of the universe [15, 17], studying the effect of charge on the curvature of spacetime in isolation is an important aspect which can then be applied to other spacetimes.

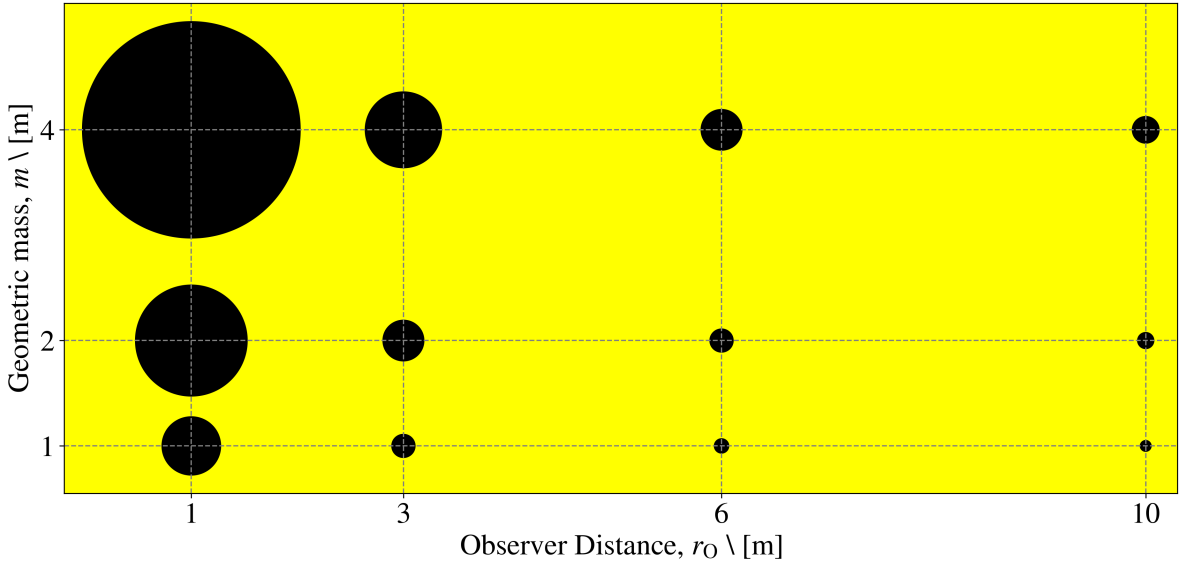


Figure 10: Angular size of a Schwarzschild BH with various observed distances,  $r_O$ , and geometric masses,  $m$ . Although equation 27 was used for the plot, the approximation in equation 24 can be used for distant observers. The yellow background depicts the homogeneously spread light sources. The program used to plot this figure can be found in appendix B.1.

The presence of charge in this universe indicates that the BH is embedded in electrovacuum, which is a source of energy-momentum, given that it arises from the presence of a Maxwell (electromagnetic) field  $F_{\mu\nu}$ . The corresponding energy-momentum tensor takes the form [15]:

$$T_{\mu\nu} = \frac{1}{\mu_0} \left( F_{\mu\alpha} F_\nu^\alpha - \frac{1}{4} g_{\mu\nu} F_{\alpha\beta} F^{\alpha\beta} \right),$$

with  $\mu_0$  being the permeability of vacuum, which will be assigned the natural units of  $\mu_0 = 1$ .

**Remark 4.3.** The energy-momentum tensor of an electromagnetic field is traceless. This can easily be verified from first principles by raising the  $\nu$  index in the above expression, and relabelling  $\nu \rightarrow \mu$ :

$$\text{tr}(T) := T_\mu^\mu = F_{\mu\alpha} F^{\mu\alpha} - \frac{1}{4} g_\mu^\mu F_{\alpha\beta} F^{\alpha\beta} = 0,$$

where  $g_\mu^\mu$  is the trace of the Kronecker delta tensor  $g_\mu^\mu = \delta_\mu^\mu = 4$ . It is easy to conclude that this trace is indeed equal to 0.

As with the Schwarzschild spacetime, the Reissner-Nordström spacetime is the unique solution to the EFEs in electro-vacuum [17]. Solving the corresponding EFEs yields the metric in  $(t, r, \theta, \phi)$  coordinates as [15, 17, 47]:

$$g_{\mu\nu} = -\left(1 - \frac{2m}{r} + \frac{Q^2}{r^2}\right)dt^2 + \left(1 - \frac{2m}{r} + \frac{Q^2}{r^2}\right)^{-1}dr^2 + r^2d\Omega^2. \quad (29)$$

It should be noted that in the most general form of this metric, the quantity  $P$  representing the magnetic charge of the BH is also included. This quantifies the amount of magnetisation present on the surface of the BH. However, since magnetic monopoles have not yet been observed in nature, this term has been set to zero.

An analysis of the null hypersurfaces shows that there are actually two event horizons in this spacetime. Indeed, by setting  $g_{tt} = 0$ , we find that:

$$\begin{aligned} 0 &= -\left(1 - \frac{2m}{r} + \frac{Q^2}{r^2}\right) \\ 0 &= r^2 - 2mr + Q^2 \implies r_{\text{eh},\pm} := r = m \pm \sqrt{m^2 - Q^2}, \end{aligned}$$

thereby confirming the existence of two event horizons  $\forall Q \in [0, m]$ . Note that the two surfaces will coincide at the critical value  $Q = m$ . If  $Q$  exceeds this value, a naked singularity will result. In such a case,  $\partial_t$  will remain timelike everywhere in this spacetime, and hence there will be no event horizon [15]. This case will be neglected since it is not realistic. As for the gravitational singularity, the Kretschmann scalar diverges when  $r = 0$  once again [15, 17].

As far as the shadow of this BH is concerned, we shall once again carry out the procedure outlined in the previous subsection. First, the radius of the photon sphere is derived by solving:

$$\begin{aligned} \frac{dh(r)^2}{dr} \Big|_{r=r_{\text{ps}}} &= \frac{d}{dr} \left[ \frac{r^2}{1 - 2m/r + Q^2/r^2} \right] \Big|_{r=r_{\text{ps}}} = 0 \\ \frac{2r_{\text{ps}}}{1 + Q^2/r_{\text{ps}}^2 - 2m/r_{\text{ps}}} - r_{\text{ps}}^2 \frac{-2Q^2/r_{\text{ps}}^3 + 2m/r_{\text{ps}}^2}{(1 + Q^2/r_{\text{ps}}^2 - 2m/r_{\text{ps}})^2} &= 0 \\ \frac{2r_{\text{ps}}^3(r_{\text{ps}}^2 - 3mr_{\text{ps}} + Q^2)}{(r_{\text{ps}}^2 - 2mr_{\text{ps}} + Q^2)^2} &= 0. \end{aligned}$$

Equating the numerator to zero and solving for the roots of the quadratic in  $r_{\text{ps}}$ , yields the interesting result:

$$r_{\text{ps},\pm} = \frac{3m \pm \sqrt{9m^2 - 8Q^2}}{2}, \quad (30)$$

which shows the existence of two photon spheres, one of which is always found inside the outer event horizon  $r_{\text{eh},+}$  of the Reissner-Nordström BH. Although for a fixed mass  $m$ , photon spheres exist for  $\forall Q \in [0, \sqrt{9/8}m]$ , this interval will instead be restricted to  $[0, m]$  to remain consistent with our restriction on the event horizons – this was done to exclude naked singularities.

Figure 11 showcases the structure of the Reissner-Nordström spacetime, in particular for the photon spheres and event horizons. These surfaces were plotted for a BH of mass  $m = 1$ , and a varying charge  $Q \in [0, m]$ . At any specific value of  $Q$ , we have  $r_{\text{ps},+} > r_{\text{eh},+} > r_{\text{ps},-} > r_{\text{eh},-}$ . This shows that only the  $r_{\text{ps},+}$  photon sphere can be physically projected on an observer’s sky.

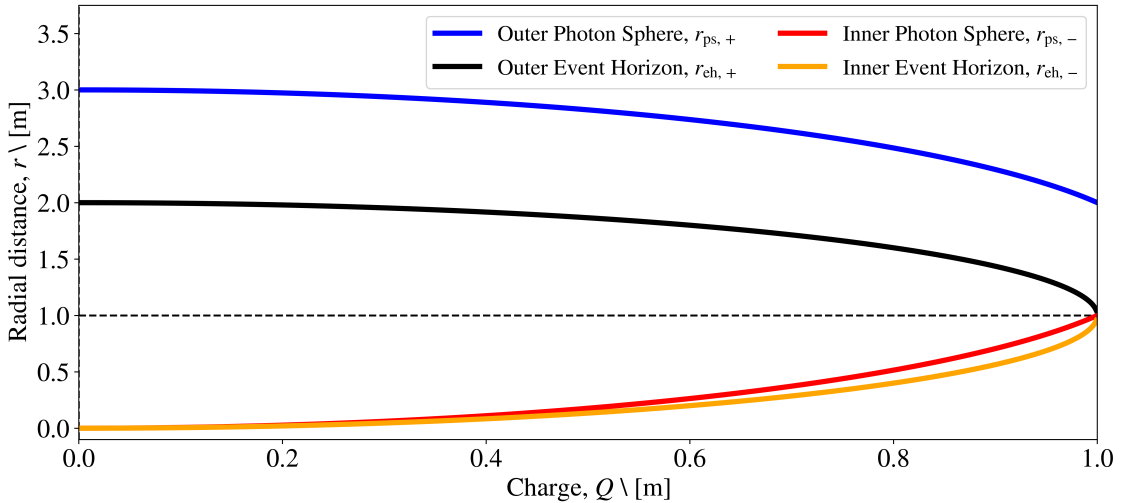


Figure 11: Plot showing the pair of photon spheres and event horizons of the Reissner-Nordström BH of mass  $m = 1$  and charge  $Q \in [0, m]$ . A vertical section will give the radial distance to each surface from the singularity at  $r = 0$ . Note that if the charge domain was extended to  $[0, \sqrt{9/8}m]$ , then the photon spheres would coincide at  $Q = m\sqrt{9/8}$ . The program used to plot this figure can be found in appendix B.2.

Using  $r_{\text{ps}} := r_{\text{ps},+} = \frac{1}{2} \left( 3m + \sqrt{9m^2 - 8Q^2} \right)$  gives rise to a critical impact parameter of:

$$b_{\text{cr}} = \frac{1}{2} \frac{3m + \sqrt{9m^2 - 8Q^2}}{1 - 2m/r_{\text{ps}} + Q^2/r_{\text{ps}}^2}$$

$$\implies b_{\text{cr}} = \frac{1}{2\sqrt{2}} \frac{(3m + \sqrt{9m^2 - 8Q^2})^2}{\sqrt{3m^2 - 2Q^2 + m\sqrt{9m^2 - 8Q^2}}}$$

Hence, the angular size of the Reissner-Nordström BH, as given by equation 23, is:

$$\alpha_{\text{sh}} = \arcsin \left[ \frac{1}{2\sqrt{2}r_O} \frac{\left[ 3m + \sqrt{9m^2 - 8Q^2} \right]^2}{\sqrt{3m^2 - 2Q^2 + m\sqrt{9m^2 - 8Q^2}}} \sqrt{1 - \frac{2m}{r_O} + \frac{Q^2}{r_O^2}} \right] \quad (31)$$

Furthermore, for a distant observer, we can approximate the shadow size using equation 24 as [47]:

$$\alpha_{\text{sh}} = \frac{1}{2\sqrt{2}r_O} \frac{\left[ 3m + \sqrt{9m^2 - 8Q^2} \right]^2}{\sqrt{3m^2 - 2Q^2 + m\sqrt{9m^2 - 8Q^2}}}, \quad \text{for } r_O \gg m. \quad (32)$$

For distant observers, the shadow size has the same  $\propto 1/r_O$  dependence as in the Schwarzschild case. Hence, its effect on the shadow size can be studied from figure 10.

To study the angular size as a function of electric charge, we can fix  $m = 10$  and  $r_O = 10m$ , and plot this dependence in figure 12. Once again, the value of the angular size is not explicitly labelled as it is not of particular relevance. From this figure, we can notice the non-linear dependence of  $\alpha_{\text{sh}}$  on  $Q$ . In fact, the deviation of  $\alpha_{\text{sh}}$  for a Reissner-Nordström BH from the Schwarzschild case is also visualised in figure 13.

## 4.4 Concluding Remarks

Firstly, every photon orbit considered in the above derivations was an unstable one. This can be verified by deriving the effective potential of the orbits and showing that the second derivative at the location of the outer photon sphere is negative. Recall that no photons can be received from stable orbits [17].

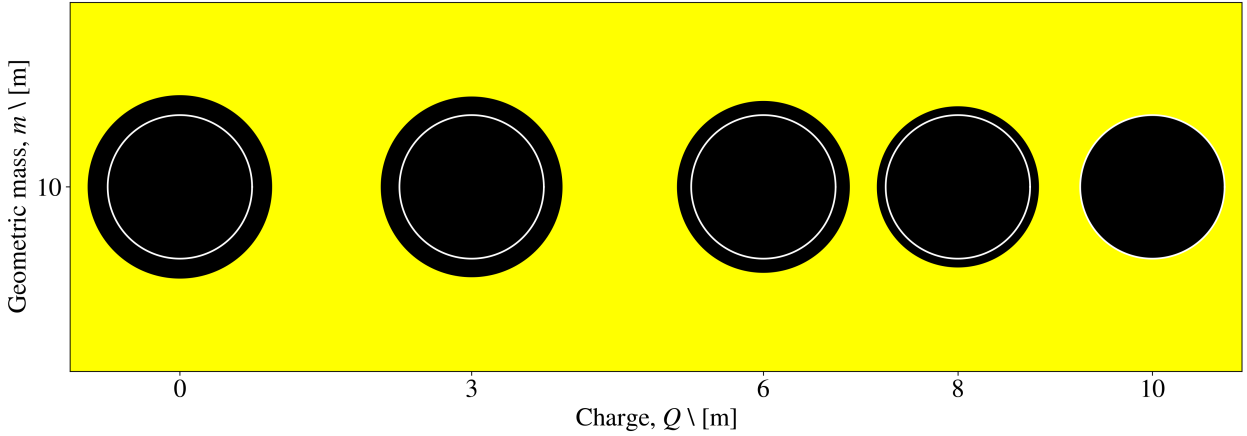


Figure 12: The angular size of a Reissner- Nordström BH shadow as a function of electric charge  $Q$ . This uses the parameters  $r_O = 10\text{m}$  and  $m = 10$ , while  $Q$  varies in the interval  $[0, m]$ . The leftmost shadow having  $Q = 0$  is identical to the Schwarzschild case, while the rightmost is the extremal Reissner-Nordström case. The internal white disk is added to compare each shadow to the extremal case. The program used to plot this figure can be found in appendix B.3.

Despite the difference in angular size between the distant Schwarzschild (equation 28) and Reissner-Nordström (equation 32) BHs, the shape of their shadow remains circular against the backdrop of dense light sources. This is attributed to the static nature of the spacetimes and the spherical symmetry of the BHs themselves. Figure 13 was plotted to directly compare the angular sizes of the two BHs, as a function of charge  $Q$ .

Had more time been allotted, the angular size of the shadow for moving observers could have been derived as part of this section. A time-dependent observer distance will induce magnifying/shrinking effects depending on the direction of motion due to results stemming from Special Relativity. Naturally, if the observer is moving along a circular path with  $r_O = \text{constant}$ , the shadow will look identical to the static case. The concept of moving observers is especially important in the context of an expanding universe. This is discussed more in-depth in [47].

Unfortunately, empirical evidence leads us to suspect that most BHs have a non-zero

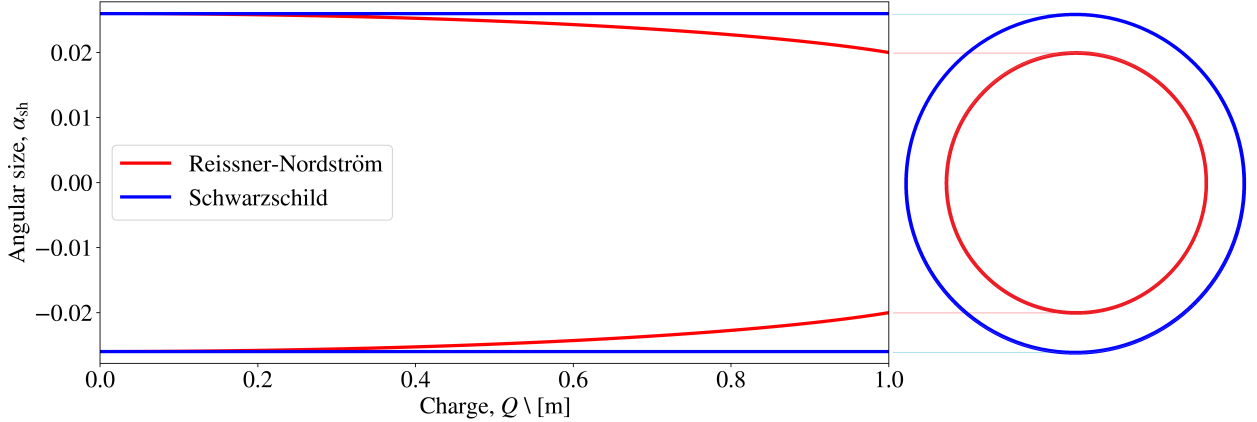


Figure 13: A comparison between the angular size of a Schwarzschild and a Reissner-Nordström BH shadow, in blue and in red, respectively. Here we have set  $m = 1$  and  $r_O = 100m$ , while  $Q \in [0, m]$  is variable. In the extreme case when  $Q = m$ , the Reissner-Nordström BH shadow appears  $\sim 23.5\%$  smaller than the Schwarzschild one. The program used to plot this figure can be found in appendix B.4.

angular momentum and have a negligible electric charge (much like most objects in the universe). For this reason, the Reissner-Nordström spacetime is probably not the most applicable model. We must therefore expand our discussion to include the broader class of rotating BHs.

---

## 5 BH shadows in stationary spacetimes

As we naturally progress towards more applicable and realistic BH models, we must relax some of our previous assumptions, particularly the requirement that the BH spacetime must be static; recall that static spacetimes require the timelike vector field  $\partial_t$  to be hypersurface orthogonal.

Although we will no longer assume a static BH spacetime, we will continue working within the framework of asymptotically flat and stationary spacetimes. This allows us to exploit certain geometric properties, which will not only simplify our analysis but also generalise our previous results. This progression brings us a step closer to a realistic description of BH shadows, particularly for rotating BHs.

As with most celestial bodies in the universe, BHs typically possess a non-zero angular momentum  $J$  about an internal axis of rotation. However, while it is generally sufficient to model slowly rotating bodies using the Schwarzschild metric, the same cannot be done for a small percentage of BHs. Note here that the use of the Schwarzschild metric is only justified for bodies whose angular momentum is negligible when compared to its geometric mass ( $m \gg J$ ), meaning that effects of distortion on the surrounding spacetime due to the rotation are minimal.

Returning to the main point, there is now substantial evidence for the existence of BHs that rotate at a rate much faster than most objects in the universe. Evidence in support of this claim began to emerge in the 1970s, when direct radio observations using interferometry revealed that M87\* – the same BH famously photographed in 2019 – featured prominent jets of ionised material being ejected from its poles, along the axis of rotation, at speeds close to those of light [62]. Since then, these relativistic jets have been extensively studied and determined to be strongly dependent on the rotation of the BH itself [10]. These jets can reach lengths of up to a few million light years, which is an order of magnitude larger

than the diameter of the Milky Way [71]. On this note, figure 14 presents one of the most prominent examples of such relativistic jets emanating from a BH.

To quantify the magnitude of a BH's rotation, we make use of its non-zero angular momentum  $J$  (in units of  $m^2$ ) to introduce the spin parameter:

$$a := \frac{J}{m}, \quad (33)$$

as commonly defined in literature [2]. This is the only additional parameter needed to describe a rotating BH in a stationary spacetime. The study of rotating BHs is primarily motivated by the inertial frame-dragging (Lense-Thirring) effect, which is a phenomenon inherently present in the vicinity of a rotating BH's surface. Due to this effect, spacetime near the BH will be drastically distorted, thereby influencing the trajectories of light and impacting the shape of the BH's shadow fundamentally. Being aware of our interest in photon orbits and their projection on an observer's sky, this effect will be worth investigating further.

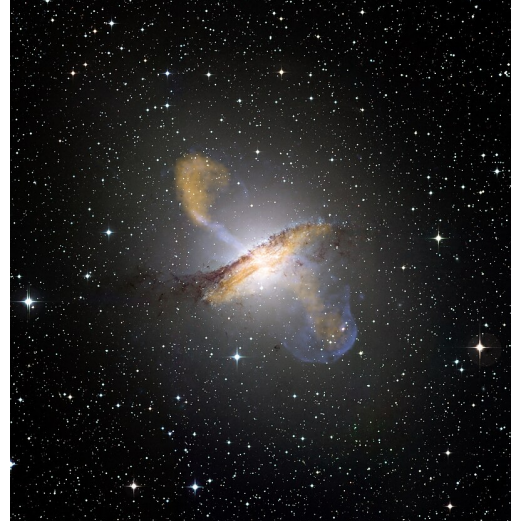


Figure 14: A composite image of Centaurus A, the nearest active radio source to Earth. A fraction of the ionised matter from its accretion disk is continuously ejected at speeds close to that of light along its axis of rotation. The jets extend up to 1.5 million light years from the centre. This is over 15 times the diameter of the Milky Way [71].

## 5.1 The frame-dragging effect

First attempts to derive the spacetime exterior to a rotating BH were made by Lense and Thirring in 1918. Using perturbation theory, they obtained an approximate result that was valid only under weak-field conditions. Despite researchers' best efforts, it was not until 1963 that Kerr derived an exact solution to the problem. Interestingly enough, despite the leap

in complexity, both solutions feature the term that is ultimately responsible for the frame-dragging effect [50]. To further study this phenomenon, we will make direct use of the radial geodesics of a rotating mass (not necessarily a BH), under weak-field conditions. Not only will this assumption yield the required result, but also simplify the derivation significantly. Consider the Lense-Thirring metric [2]:

$$ds^2 = - \left(1 - \frac{2m}{r}\right) dt^2 + \left(1 + \frac{2m}{r}\right) dr^2 + r^2 d\Omega^2 - \frac{4ma}{r} \sin^2 \theta \, d\phi \, dt, \quad (34)$$

where  $ma = J$ , as defined in 33. What is most important to note is that this solution is only valid up to first order in the parameters  $m/r$  and  $a/r$ , meaning that bodies described by this metric should be magnitudes larger than their associated Schwarzschild radius, and not spinning too rapidly [2].

The first step in deriving the radial geodesics for this spacetime is to obtain the equations of motion, which is achieved by using the ELE with  $x^\mu \in \{t, r, \theta, \phi\}$  and  $\mathcal{L} = \frac{1}{2}g_{\mu\nu}x^\mu x^\nu$ . Substituting the coordinates denoted by  $x^\mu$  in the ELE, we find [2]:

$$x^\mu = t \implies \frac{d}{d\lambda} \left[ - \left(1 - \frac{2m}{r}\right) \dot{t} - \frac{2ma}{r} \sin^2 \theta \dot{\phi} \right] = 0, \quad (35)$$

$$\begin{aligned} x^\mu = r \implies & \frac{d}{d\lambda} \left[ \left(1 + \frac{2m}{r}\right) \dot{r} \right] - \\ & \left[ -\frac{m}{r^2}(\dot{t}^2 + \dot{r}^2) + r(\dot{\theta}^2 + \sin^2 \theta \dot{\phi}^2) + \frac{2ma}{r^2} \sin^2 \theta \dot{\phi} \dot{t} \right] = 0, \end{aligned} \quad (36)$$

$$x^\mu = \theta \implies \frac{d}{d\lambda} \left( r^2 \dot{\theta} \right) - \left( r^2 \sin \theta \cos \theta \dot{\phi}^2 - \frac{4ma}{r} \sin \theta \cos \theta \dot{\phi} \dot{t} \right) = 0, \quad (37)$$

$$x^\mu = \phi \implies \frac{d}{d\lambda} \left( r^2 \sin^2 \theta \dot{\phi} - \frac{2ma}{r} \sin^2 \theta \dot{t} \right) = 0. \quad (38)$$

To further simplify our analysis, we shall restrict our search to instantaneous radial geodesics in the equatorial plane ( $\theta = \frac{\pi}{2}$ ). By 'instantaneous' we mean that the condition  $\dot{\phi}(t) = 0$  need only hold for a single instant in time,  $t = t_0$ . This will allow us to derive the strength of the Lense-Thirring effect for an observer at a single instant in time, which is

sufficient. Proceeding with our derivation, we may further process equation 38 to obtain:

$$\begin{aligned} \left[ 2r\dot{r}\dot{\phi} + r^2\ddot{\phi} + \frac{2ma}{r^2}\dot{r}\dot{t} - \frac{2ma}{r}\ddot{t} \right]_{t=t_0} &= 0 \\ \implies r\ddot{\phi} + \frac{2ma}{r^3}\dot{r}\dot{t} - \frac{2ma}{r^2}\ddot{t} &= 0, \quad \text{since } \dot{\phi}(t_0) = 0, \end{aligned} \quad (39)$$

and from equation 35, without needing to differentiate, we may deduce that:

$$\begin{aligned} \frac{d}{d\lambda} \left[ -\left(1 - \frac{2m}{r}\right)\dot{t} - \frac{2ma}{r}\dot{\phi} \right] &= 0 \\ -\left(1 - \frac{2m}{r}\right)\dot{t} - \frac{2ma}{r}\dot{\phi} &= \alpha \quad (\text{constant}) \\ \implies \dot{t} &= -\frac{\alpha}{1 - \frac{2m}{r}}, \text{ with } \dot{\phi}(t_0) = 0. \end{aligned} \quad (40)$$

Actually, equation 35 gives us two useful expressions. One is obtained above, while the other is obtained by going through the process of differentiation. The latter approach yields:

$$\begin{aligned} 0 &= -\left(1 - \frac{2m}{r}\right)\ddot{t} - \frac{2ma}{r}\ddot{\phi} - \frac{2m}{r^2}\dot{r}\dot{t} \\ \implies \ddot{t} &= -\frac{2ma}{r\left(1 - \frac{2m}{r}\right)}\ddot{\phi} - \frac{2m\alpha}{r^2\left(1 - \frac{2m}{r}\right)^2}\dot{r} \end{aligned} \quad (41)$$

By substituting this expression for  $\ddot{t}$ , and equation 40 for  $\dot{t}$  into equation 39, we find:

$$\begin{aligned} r\ddot{\phi} + \frac{2ma}{r^3} \left[ -\frac{\alpha}{1 - \frac{2m}{r}} \right] \dot{r} - \frac{2ma}{r^2} \left[ -\frac{2ma}{r\left(1 - \frac{2m}{r}\right)}\ddot{\phi} - \frac{2m\alpha}{r^2\left(1 - \frac{2m}{r}\right)^2}\dot{r} \right] &= 0 \\ \implies r\ddot{\phi} \left[ 1 + \frac{4m^2a^2}{r^4\left(1 - \frac{2m}{r}\right)} \right] - \frac{2ma\alpha}{r^3\left(1 - \frac{2m}{r}\right)} \left[ 1 + \frac{2m}{r\left(1 - \frac{2m}{r}\right)} \right] \dot{r} &= 0 \end{aligned}$$

Finally, given our assumption that the radius of the mass is much larger than its associated Schwarzschild radius, we have  $r \gg 2m$ , or equivalently,  $1 \gg \frac{m}{r}$ . Additionally, we have also assumed a relatively small angular momentum such that  $1 \gg a := \frac{J}{m}$ , leading to a second weak-field approximation  $1 \gg \frac{a}{r}$ . Combining these two results allows us to use the approximation:

$$\left(1 - \frac{2m}{r}\right)^{-1} \simeq 1 + \frac{2m}{r} + \mathcal{O}\left[\left(\frac{m}{r}\right)^2\right] \quad (42)$$

This simplifies the expression for the radial geodesics in the Lense-Thirring spacetime in 42 to:

$$\begin{aligned} r\ddot{\phi} \left[ 1 + \frac{4m^2a^2}{r^4} \left( 1 + \frac{2m}{r} \right) \mathcal{O}\left[\left(\frac{m}{r}\right)^2\right] \right] - \frac{2ma\alpha}{r^3} \left( 1 + \frac{2m}{r} \right) \left[ 1 + \frac{2m}{r} \left( 1 + \frac{2m}{r} \right) \right] \dot{r} &= 0 \\ r\ddot{\phi} - \frac{2ma\alpha}{r^3} \left( 1 + \frac{4m}{r} + \mathcal{O}\left[\left(\frac{m}{r}\right)^2\right] \right) \dot{r} &= 0 \\ \implies r\ddot{\phi} + \left( -\frac{2ma\alpha}{r^3} \right) \dot{r} &= 0 \quad (43) \end{aligned}$$

By comparing this equation to the classical equation describing the Coriolis force [64]:

$$r\ddot{\phi} + \omega\dot{r} = 0,$$

we immediately begin to observe some similarity. Note here that  $\omega$  is a constant angular velocity related to the relative velocity of an observer's frame with respect to an inertial one.

**Remark 5.1.** While these expressions do share a similar format, we should not overlook the fact that the  $\frac{2ma}{r^3}$  term is not constant along infalling radial geodesics! Its explicit dependence on the radial distance  $r$  implies that as particles are approaching a rotating BH, the force they experience will increase as a function of  $\frac{1}{r^3}$ . Another important distinction we can make is that the frame-dragging effect describes a physical force that alters the trajectory of all objects approaching the BH's surface. This is fundamentally different from the Coriolis force, which, contrary to popular belief, is simply a fictitious force arising from the relative motion of an observer's rotating frame with respect to an inertial one [2, 52].

As a final addition to this section, the spacetime surrounding a rotating BH has been depicted in figure 15. In the figure, the black lines incident on the surface of the BH represent the radial geodesics, whose trajectories were derived in this section, while the concentric circular ones are the (unstable) circular orbits. This diagram is not drawn to scale and is simply used to illustrate the Lense-Thirring effect. It is apparent that the influence of a BH's rotation on the trajectories of null geodesics leads to a distinct change in the shape

of the BH shadow as seen by a distant observer. To derive exact expressions for these null geodesics, we must introduce the Kerr solution.

## 5.2 The Kerr spacetime

The spacetime describing an axisymmetric, uncharged mass rotating with some non-zero angular momentum  $J = ma$  about the  $z$ -axis, embedded in a static universe ( $\Lambda = 0$ ), is given by the Kerr solution. As previously mentioned, this metric generalises the Lense-Thirring metric and is valid in both weak and strong-field regimes as it is an exact solution under the given conditions. Although this analytical result was derived 45 years after the first approximate result, we shall only take a few seconds to state it below.

To describe a rotating BH under the given conditions, we must first select an appropriate set of global spacetime coordinates. Of the many that exist, we will adopt the Boyer-Lindquist coordinates. The use of these coordinates is motivated by the fact that the system Hamiltonian,  $\mathcal{H}$ , will be in fully separable form [16, 17, 24, 52]. This will allow a third necessary constant of motion to arise naturally. Obviously, there are no universally applicable sets of coordinates. In fact, certain patterns are more easily seen under other coordinate systems, such as the Kerr-Schild [52].

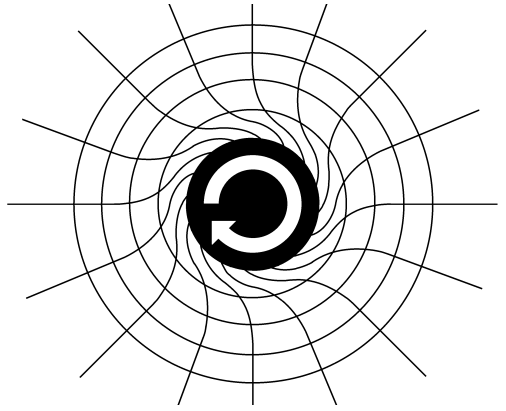


Figure 15: The frame-dragging (Lense-Thirring) effect present in the proximity of a rotating BH. The clockwise rotation of the BH causes the local spacetime around the BH to experience a 'drag' in the direction of the rotation. The geodesics depicted are all found in the equatorial plane.

In the Boyer-Lindquist coordinates [52],

$$x = \sqrt{r^2 + a^2} \sin \theta \cos \phi, \quad y = \sqrt{r^2 + a^2} \sin \theta \sin \phi, \quad z = r \cos \theta,$$

the Kerr metric takes the form [15]:

$$g_{\mu\nu} = - \left( 1 - \frac{2mr}{\rho^2} \right) dt^2 + \frac{\rho^2}{\Delta} dr^2 + \rho^2 d\theta^2 - \frac{4mra \sin^2 \theta}{\rho^2} dt d\phi + \left[ \frac{(r^2 + a^2)^2 - a^2 \Delta \sin^2 \theta}{\rho^2} \right] \sin^2 \theta d\phi^2 \quad (44)$$

where we have explicitly set,

$$\rho^2 := r^2 + a^2 \cos^2 \theta, \text{ and } \Delta := r^2 - 2mr + a^2. \quad (45)$$

One may note that in the limit as  $a \rightarrow 0$ , the metric reduces to the Schwarzschild case. Moreover, in the weak-field limit with only first-order terms in  $\frac{m}{r}$  and  $\frac{ma}{r}$ , we recover the Lense-Thirring metric, as was to be expected. Furthermore,  $\partial_t$  is no longer hypersurface orthogonal to surfaces with  $r = \text{constant}$ , due to the presence of the cross term  $g_{t\phi}$ . This can be confirmed explicitly using equation 9, which shows that the spacetime is not static [15]. There is, however, one vector field which is hypersurface orthogonal and null on the outer event horizon at  $r = r_{\text{eh},+}$ . This is the linear combination [17, 52]:

$$\xi^{(i)} = \partial_t^{(i)} + \frac{a}{r_{\text{eh},+}^2 + a^2} \partial_\phi^{(i)}, \quad (46)$$

where the constant multiplying  $\partial_\phi$  can be interpreted as the angular velocity of the rotating BH at the outer event horizon, and the  $i$  superscript is used to access the components of the Killing vector.

### 5.2.1 Important Surfaces

The presence of the  $\rho$  and  $\Delta$  terms has profound implications on the geometry of this spacetime. These will give rise to several physical surfaces which describe interesting phenomena occurring on or beyond them.

To locate the event horizons of this spacetime, we begin by examining the radial coordinate,  $g_{rr} := \frac{\rho^2}{\Delta}$ . We can deduce the existence of two values for  $r$  that lead to a coordinate singularity with  $0 = \Delta := r^2 - 2mr + a^2$ . Solving for the roots of  $\Delta$  leads to the solutions:

$$r_{\text{eh},\pm} := r = m \pm \sqrt{m^2 - a^2}. \quad (47)$$

To ensure real values of  $r_{\text{eh},\pm}$ , we impose the restriction  $|a| \leq m$ , with  $a = m$  being the *Extremal Kerr BH*, and  $a = 0$  the Schwarzschild case. The existence of two event horizons parallels the structure of the Reissner-Nordström solution, which similarly restricts the magnitude of  $Q$  to be smaller than  $m$ . In this case, the event horizons are found in the interval  $r_{\text{eh},+} \in [m, 2m]$  and  $r_{\text{eh},-} \in [0, m]$ , both obtained by substituting the maximal/minimal values of  $a$  in 47.

Moving on to the curvature singularity of the Kerr BH, we can state the associated Kretschmann scalar as [52]:

$$\kappa_{\text{Kretsch}} = \frac{48m^2(r^2 - a^2 \cos^2 \theta)(\rho^4 - 16a^2r^2 \cos^2 \theta)}{\rho^{12}}, \quad (48)$$

which is singular whenever  $0 = \rho^2 := r^2 + a^2 \cos^2 \theta$ . While this condition is trivially satisfied at  $\theta = \frac{\pi}{2}$  and  $r = 0$ , we should not rush to conclude that this represents a single point in spacetime! In fact, the use of Boyer-Lindquist coordinates introduces ambiguities in describing the singularity's structure, given that the coordinate system fails in the region beyond the outer event horizon. More precisely, this is because  $g_{tt}$  becomes spacelike while  $g_{rr}$  timelike, as with the Schwarzschild case. A clearer representation is obtained with the use of Kerr-Schild coordinates. This new coordinate system  $(t', x, y, z)$ , given by [24] as:

$$x + iy = (r + ia) \sin \theta e^{i\psi}, \quad z = r \cos \theta, \quad t' = t + \tau, \quad (49)$$

where:

$$\psi := \phi + \frac{a}{2\sqrt{m^2 - a^2}} \ln \left| \frac{r - r_{\text{eh},+}}{r - r_{\text{eh},-}} \right|, \quad (50)$$

$$\tau := \frac{mr_{\text{eh},+}}{\sqrt{m^2 - a^2}} \ln \left| \frac{r}{r_{\text{eh},+}} - 1 \right| - \frac{mr_{\text{eh},-}}{\sqrt{m^2 - a^2}} \ln \left| \frac{r}{r_{\text{eh},-}} - 1 \right|, \quad (51)$$

may be used to verify the relationship:

$$\begin{aligned} x^2 + y^2 &= (r^2 + a^2) \sin^2 \theta, \text{ and } z^2 = r^2 \cos^2 \theta \\ \implies \frac{x^2}{r^2 + a^2} + \frac{y^2}{r^2 + a^2} + \frac{z^2}{r^2} &= 1, \end{aligned} \quad (52)$$

which intuitively implies that surfaces with  $r = \text{constant}$ , represent ellipsoids. For the case of the singularity, inputting  $r = 0$  and  $\theta = \frac{\pi}{2}$  yields the condition:

$$x^2 + y^2 = a^2, \quad z = 0 \quad \dots \text{ a ring!} \quad (53)$$

Unlike all previous point-like singularities encountered for non-rotating BHs, the gravitational singularity of a Kerr BH is ring-shaped. This has profound implications as discussed by Chandrasekhar in [17], but omitted for the sake of brevity.

Another region of interest in this spacetime is the so-called ergoregion. Intuitively, the surface of this region (ergosphere) is a static limit surface beyond which static observers (those with  $\dot{r} = \dot{\theta} = \dot{\phi} = 0$ ) cannot exist, i.e. every observer is inevitably forced to co-rotate with the BH due to the extreme frame-dragging effects. More formally,

**Definition 5.1.** A static limit surface corresponds to the surface on which  $g_{tt} \equiv 0$ .

Inside this region, the timelike component of the metric transitions becomes spacelike (positive). Static observers are forbidden from existing within it [17].

While for the Schwarzschild and Reissner-Nordström spacetimes the ergosphere surface was found to coincide with the outer event horizon, this is not the case for the Kerr spacetime. In this case, the timelike killing vector  $\partial_t$  is null at three distinct spatial regions – the two event horizons, and the ergosphere. To determine the location of the ergosphere, we solve

for the radius at which  $g_{tt}(r)$  becomes null [37, 52]:

$$\begin{aligned}
 0 \equiv g_{tt} &= \frac{2mr}{\rho^2} - 1 \\
 2mr &= r^2 + a^2 \cos^2 \theta \equiv r^2 + a^2 \cos^2 \theta + (m^2 - m^2) \\
 0 &= (r^2 - 2mr + m^2) + (a^2 \cos^2 \theta - m^2) \\
 (r - m)^2 &= m^2 - a^2 \cos^2 \theta \\
 \implies r_{\text{es}} &:= r = m + \sqrt{m^2 - a^2 \cos^2 \theta}
 \end{aligned} \tag{54}$$

**Remark 5.2.** At  $\theta = 0, \pi$ , the ergosphere coincides with the outer event horizon, while at  $\theta = \frac{\pi}{2}, \frac{3\pi}{2}$ , the ergosphere is at maximum separation from the event horizon. Unlike an event horizon, however, the ergosphere does not causally disconnect spacetime, i.e. it is not a one-way membrane.

**Remark 5.3.** The ergoregion allows for energy to be extracted from a rotating BH through the Penrose process. A detailed discussion is presented in [24].

The surfaces discussed so far have been illustrated in figures 16 and 21 for various values of  $a$ , and a fixed value of  $m = 1$ . For small  $a$ , there is very little deviation from a Schwarzschild BH, while as  $a$  is increased, the regions become increasingly deformed. At the extremes:

- ✿  $a = 1$ : the outer horizon, inner horizon and singularity coincide at  $r = m$
- ✿  $a = 0$ : the outer horizon and ergosphere coincide at  $r = m$ , and the inner horizon and ring singularity vanish at  $r = 0$ .

Before concluding this subsection, it is important to emphasise the absence of spherical symmetry in the Kerr spacetime, primarily due to the presence of the cross-term  $g_{t\phi}$  that eliminates the two Killing vectors:

$$\psi_1 = \sin \phi \partial_\theta + \cot \theta \cos \phi \partial_\phi \quad \text{and} \quad \psi_2 = -\cos \phi \partial_\theta + \cot \theta \sin \phi \partial_\phi \tag{55}$$

associated with rotational symmetry along the  $x$  and  $y$ -axes, respectively [18, 52, 68]. This term is also responsible for  $\partial_t$  not being hypersurface orthogonal to the surface of the event

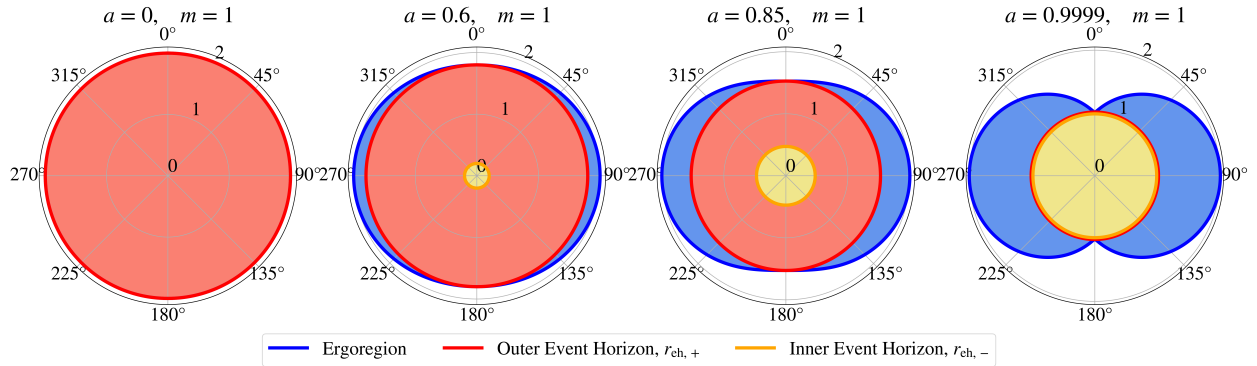


Figure 16: Surfaces characteristic to the Kerr BH in Boyer-Lindquist coordinates. In these plots, the  $r$  coordinate describes the radial distance while the inclination angle  $\theta$  increases clockwise starting from the vertical  $z$ -axis ( $\theta = 0^\circ$ ). The BH is also rotating along the  $z$ -axis. The program used to plot this figure can be found in appendix B.5.

horizons. As previously mentioned, this asymmetry significantly impacts photon orbits around the Kerr BH. Unlike the case for static BHs, where spherical orbits were confined to a 2-sphere with  $\theta = \text{constant}$  (planar), this is not generally the case for stationary BHs. The absence of spherical symmetry means that  $\theta$  (and all trigonometric terms) must be treated as variables, greatly complicating the derivation of the radii for photon orbits. Nevertheless, to build intuition for this concept, we shall begin by discussing equatorial orbits. By generalising these orbits to an arbitrary inclination  $\theta$ , we will eventually deduce the desired shape of the shadow for a rotating BH.

### 5.2.2 Equatorial Photon Orbits

By once again imposing the constraints:  $\theta = \frac{\pi}{2}$  ( $= \text{constant}$ ) and  $\dot{\theta} = 0$ , on the Kerr metric, we shall restrict our search to circular orbits residing on the equatorial plane. To derive our desired result, we may proceed by following an outline of the derivation found in section 4.1. This approach requires the use of the system Lagrangian, which in this case is stated as:

$$\mathcal{L} = \frac{1}{2} \left\{ - \left( 1 - \frac{2m}{r} \right) \dot{t}^2 - \frac{4ma}{r} \dot{t} \dot{\phi} + \frac{r^2}{\Delta} \dot{r}^2 + \left[ (r^2 + a^2) + \frac{2ma^2}{r} \right] \dot{\phi}^2 \right\}. \quad (56)$$

Since  $\partial_t$  and  $\partial_\phi$  are Killing vector fields in this spacetime, their associated conjugate

momenta will be conserved. This fact can also be deduced from the fact that  $t$  and  $\phi$  are cyclic coordinates of the Lagrangian,  $\mathcal{L} \neq \mathcal{L}(t, \phi)$ . This allows us to set:

$$p_t := \frac{\partial \mathcal{L}}{\partial \dot{t}} = -\left(1 - \frac{2m}{r}\right)\dot{t} - \frac{2ma}{r}\dot{\phi} \equiv -E \quad (\text{constant}), \quad (57)$$

and

$$p_\phi := \frac{\partial \mathcal{L}}{\partial \dot{\phi}} = -\frac{2ma}{r}\dot{t} + \left[(r^2 + a^2) + \frac{2ma^2}{r}\right]\dot{\phi} \equiv L \quad (\text{constant}), \quad (58)$$

where  $E$  refers to the total energy of the photon, and  $L$  its angular momentum about the  $z$ -axis, as before. These relations will simplify our upcoming analysis in two distinct ways. Firstly, we may observe that the above equations represent a system of two coupled first-order exact differential equations that can be decoupled into two independent expressions such that both  $\dot{t}$  and  $\dot{\phi}$  become explicitly dependent on  $r$ . Indeed, by converting the system to matrix form, we find:

$$\begin{aligned} & \begin{pmatrix} \left(1 - \frac{2m}{r}\right) & \frac{2ma}{r} \\ -\frac{2ma}{r} & \left[(r^2 + a^2) + \frac{2ma^2}{r}\right] \end{pmatrix} \begin{pmatrix} \dot{t} \\ \dot{\phi} \end{pmatrix} = \begin{pmatrix} E \\ L \end{pmatrix} \\ & \begin{pmatrix} \dot{t} \\ \dot{\phi} \end{pmatrix} = \begin{pmatrix} \left(1 - \frac{2m}{r}\right) & \frac{2ma}{r} \\ -\frac{2ma}{r} & \left[(r^2 + a^2) + \frac{2ma^2}{r}\right] \end{pmatrix}^{-1} \begin{pmatrix} E \\ L \end{pmatrix} \\ & \Rightarrow \begin{pmatrix} \dot{t} \\ \dot{\phi} \end{pmatrix} = \frac{1}{\Delta} \begin{pmatrix} \left[(r^2 + a^2) + \frac{2ma^2}{r}\right] & -\frac{2ma}{r} \\ \frac{2ma}{r} & \left(1 - \frac{2m}{r}\right) \end{pmatrix} \begin{pmatrix} E \\ L \end{pmatrix}, \end{aligned} \quad (59)$$

where  $\Delta := r^2 - 2mr + a^2$  represents the determinant of the above  $2 \times 2$  matrix. This term constrains our matrix to be singular only at the event horizons,  $r_{\text{eh},\pm}$ , which are not of particular concern to us, since photon orbits are not found on these surfaces anyway. This mini-derivation allows us to finally conclude that:

$$\dot{t} = \frac{1}{\Delta} \left[ \left[(r^2 + a^2) + \frac{2ma^2}{r}\right] E - \frac{2ma}{r} L \right] \quad (60)$$

$$\dot{\phi} = \frac{1}{\Delta} \left[ \frac{2ma}{r} E + \left(1 - \frac{2m}{r}\right) L \right] \quad (61)$$

At this point, we can proceed in two ways. The first option is to use the integral of the line element:

$$0 \equiv g_{\mu\nu}\dot{x}^\mu\dot{x}^\nu = -\left(1 - \frac{2m}{r}\right)\dot{t}^2 - \frac{4ma}{r}\dot{t}\dot{\phi} + \frac{r^2}{\Delta}\dot{r}^2 + \left[(r^2 + a^2) + \frac{2ma^2}{r}\right]\dot{\phi}^2, \quad (62)$$

in which case, the geodesics can easily be derived by substituting equations 57, 58, 60, and 61, and applying some algebraic manipulation. Alternatively, we can also use the system Hamiltonian,  $\mathcal{H}$ . While the first method is definitely more straightforward in this case, the Hamiltonian approach offers a more general framework. In view of this, it makes more sense to derive the geodesic equation using the latter method. To achieve this, we must perform a Legendre transformation on the Lagrangian,  $\mathcal{L}$ , as defined in 7. This yields [17, 24]:

$$\begin{aligned} \mathcal{H} &= p_t\dot{t} + p_r\dot{r} + p_\phi\dot{\phi} - \mathcal{L} \\ &= \left[2\left(1 - \frac{2m}{r}\right)\dot{t} + \frac{4ma}{r}\dot{\phi}\right]\dot{t} + \left[\frac{r^2\dot{r}}{2\Delta}\right]\dot{r} \\ &\quad + \left\{-\frac{4ma}{r}\dot{t} + 2\left[(r^2 + a^2) + \frac{2ma^2}{r}\right]\dot{\phi}\right\}\dot{\phi} - \mathcal{L}. \end{aligned} \quad (63)$$

Substituting the Lagrangian from equation 56 into the above expression gives:

$$\begin{aligned} \mathcal{H} &= -\frac{1}{2}\left(1 - \frac{2m}{r}\right)\dot{t}^2 - \frac{2ma}{r}\dot{t}\dot{\phi} + \frac{r^2}{2\Delta}\dot{r}^2 + \frac{1}{2}\left[(r^2 + a^2) + \frac{2ma^2}{r}\right]\dot{\phi}^2 \\ &= \frac{1}{2}\left(-E\dot{t} + \frac{r^2}{\Delta}\dot{r}^2 + L\dot{\phi}\right), \end{aligned} \quad (64)$$

with the last step following swiftly through substitution and rearrangement, but omitted for the sake of brevity. To proceed further, we note from definition 7 that we have  $\mathcal{H} = 0$  for null geodesics. This result comes from substituting the explicit form of the Lagrangian,  $\mathcal{L} = \frac{1}{2}g_{\mu\nu}\dot{x}^\mu\dot{x}^\nu$ , into definition 7, together with an expanded form of the conjugate momenta:

$$\begin{aligned} p_{x_\mu} &:= \frac{\partial\mathcal{L}}{\partial\dot{x}^\mu} = \frac{\partial}{\partial\dot{x}^\mu}\left(\frac{1}{2}g_{\mu\nu}\dot{x}^\mu\dot{x}^\nu\right) \\ &\implies p_{x_\mu} = g_{\mu\nu}\dot{x}^\nu. \end{aligned} \quad (65)$$

This results in the Hamiltonian:

$$\begin{aligned} \mathcal{H} &:= p_{x_\mu} \dot{x}^\mu - \mathcal{L} \\ \mathcal{H} &= (g_{\mu\nu} \dot{x}^\nu) \dot{x}^\mu - \frac{1}{2} g_{\mu\nu} \dot{x}^\nu \dot{x}^\mu = \frac{1}{2} g_{\mu\nu} \dot{x}^\nu \dot{x}^\mu \\ \implies \mathcal{H} &= \frac{1}{2} g_{\mu\nu} \dot{x}^\nu \dot{x}^\mu = \begin{cases} 0, & \dot{x}^\mu \text{ is null} \\ -1, & \dot{x}^\mu \text{ is timelike} \end{cases} \end{aligned} \quad (66)$$

With the above result following by the definition of the 4-velocity along an arbitrary space-time curve [68]. Imposing  $\mathcal{H} = 0$  for the null geodesics in the Kerr metric, we can further simplify equation 64 to obtain the required geodesic equation as:

$$\begin{aligned} 0 \equiv \mathcal{H} &= \frac{1}{2} \left( -E\dot{t} + \frac{r^2}{\Delta} \dot{r}^2 + L\dot{\phi} \right) \\ &= -E \left\{ \left[ (r^2 + a^2) + \frac{2ma^2}{r} \right] E - \frac{2ma}{r} L \right\} + r^2 \dot{r}^2 \\ &\quad + L \left[ \frac{2ma}{r} E + \left( 1 - \frac{2m}{r} \right) L \right] \\ \implies r^2 \dot{r}^2 &= E^2 \left[ (r^2 + a^2) + \frac{2ma^2}{r} \right] - 2EL \left[ \frac{2ma}{r} \right] - L^2 \left[ 1 - \frac{2m}{r} \right]. \end{aligned} \quad (67)$$

While the general geodesic equation fully describes photon trajectories with  $\dot{\theta} = 0$ , we will focus exclusively on the circular orbits, which also satisfy  $\dot{r} = 0 = \ddot{r}$  by definition. At this stage, we are once again presented with two distinct approaches to derive the radii of the unstable equatorial photon orbits.

The first approach, as outlined in [24], solves for the roots of the above quadratic in  $E$ , yielding two potentials  $V_\pm(r)$ , which correspond to the potential energy of a photon orbit as a function of radial distance. This is because the LHS of equation 67 encompasses the kinetic energy of the orbit, while the RHS contains the potential energy contributions. Although this method does not directly provide the orbital radii, these can be derived from the locations of the maximal turning points of  $V_\pm(r)$ . At these maxima, the net force on the photon will

be zero since the gradient of the potential,  $\frac{d}{dr}V_{\pm}(r)$ , represents a force. Hence the condition,

$$\left. \frac{d}{dr}V_{\pm}(r) \right|_{r=r_{ps}} = 0$$

This equilibrium condition implies that the photon is in a circular orbit. By setting  $\dot{r} = 0$  in equation 67, the roots of the polynomial in  $E$ , i.e. the potential curves, can be expressed as [2, 24]:

$$V_{\pm}(r) = \frac{2mar \pm r^2\sqrt{\Delta}}{(r^2 + a^2)^2 - a^2\Delta} L, \quad (68)$$

one for each of the two possible photon orbits in the equatorial plane. A natural question that arises is the orientation of these orbits: are they co-rotating or counter-rotating with the BH's own rotation?

**Remark 5.4.** Intuitively, a photon orbiting in the same direction as the BH's rotation (co-rotating) will experience less frame-dragging, while a photon orbiting in opposition to the BH (counter-rotating) will experience more drag. Thus, we expect to find that co-rotating orbits will be found closer to the BH than their counter-rotating counterparts.

To quantify this, we must examine the product  $La \equiv \frac{LJ}{m}$  present in the above potential terms. Indeed,

- ⌘ if  $La < 0$ : the photon and BH are counter-rotating, since  $L$  and  $J$  have opposite signs
- ⌘ if  $La > 0$ : the photon and BH are co-rotating, since  $L$  and  $J$  have the same sign.

To maintain the convention  $V_+ \geq V_-$ , regardless of whether or not the orbit is co- or counter-rotating, we may, without loss of generality, redefine the effective potentials as:

$$V_{\pm}^{\text{eff}}(r) = \frac{2mrLa \pm |L|r^2\sqrt{\Delta}}{(r^2 + a^2)^2 - a^2\Delta}. \quad (69)$$

This allows us to describe the effective gravitation potential barrier for both orbital orientations only using  $V_+^{\text{eff}}(r)$ , while  $V_-^{\text{eff}}(r)$  remains redundant, but still relevant for other analyses. Furthermore, while the previous definition introduced an interchange between  $V_+(r)$  and  $V_-(r)$  whenever  $L$  and  $a$  were both negative (but  $La > 0$ ), this case has been

resolved [24]. Plots of  $V_{\pm}^{\text{eff}}(r)$  as functions of  $r$  are showcased in figure 17, with the orbital parameters:  $m = 1$ ,  $|a| = 0.8$ , and  $L = 1$ .

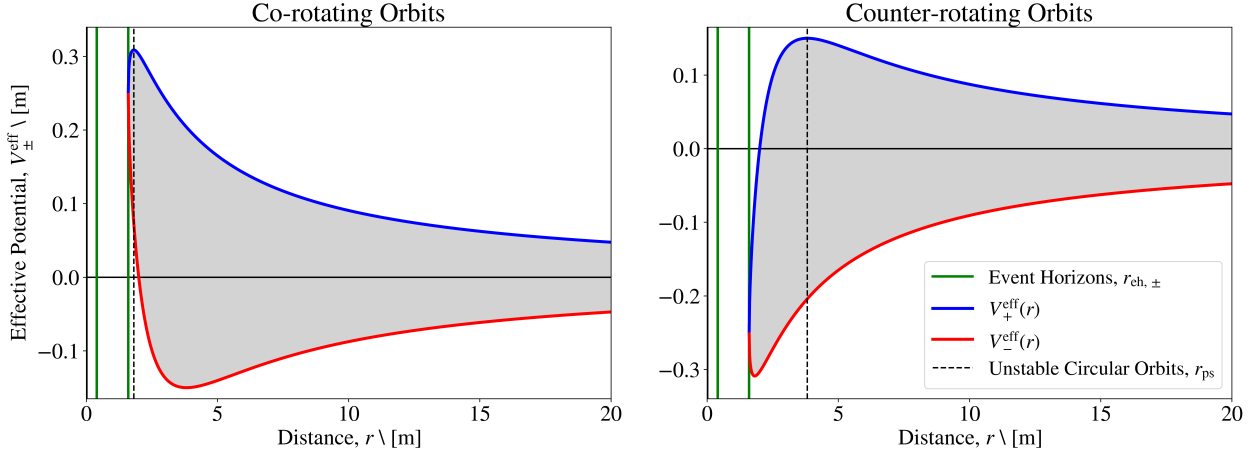


Figure 17: Plots of  $V_{\pm}^{\text{eff}}(r)$  as functions of the radial orbital distance,  $r$ . The left plot corresponds to the co-rotating case, while the right plot corresponds to the counter-rotating case. We have set  $m = L = 1$ , and  $|a| = 0.8$ . The two green vertical lines correspond to the locations of the two event horizons (found from 47), while the dashed line highlights the exact turning point of  $V_+^{\text{eff}}(r)$ . The grey region is forbidden for equatorial photon orbits. The program used to plot this figure can be found in appendix B.6.

To study the fate of a photon in this spacetime we must examine the relationship between its total (kinetic plus potential) energy and the effective radial potential of the BH. Consider a photon with some fixed total radial energy  $E$ , and suppose that  $V_+^{\text{eff}}(r)$  is maximal for some  $r = r_{\text{max}}$ . With the help of figure 18, we note that:

- ✿ if  $E > V_+^{\text{eff}}(r_{\text{max}})$  (in orange) – the total radial energy of the photon will be greater than the BH's potential barrier. Such photons have too much energy to be captured into a circular orbit. They can easily overcome the potential barrier and enter the event horizon since they will always have a non-zero radial kinetic energy towards the singularity.
- ✿ if  $E = V_+^{\text{eff}}(r_{\text{max}})$  (in red) – the radial energy of the photon is just enough for it to be captured in an unstable circular orbit at a distance  $r = r_{\text{max}}$  from the BH. At  $r = r_{\text{max}}$ ,

all its radial kinetic energy is converted to potential energy.

- ✿ if  $V_+^{\text{eff}}(r) < E < V_+^{\text{eff}}(r_{\max})$  (in brown) – the incoming photon reaches some minimum radial distance  $R > r_{\max}$  before receding to infinity. Its total energy is not sufficient to overcome the potential barrier. At the closest approach, the photon's energy will momentarily be entirely potential, before transitioning back to outgoing kinetic.
- ✿ if  $V_-^{\text{eff}}(r) < E < V_+^{\text{eff}}(r)$  – the photon's total energy is in the grey-shaded region of the plots in diagram 17. In this region, its square velocity becomes  $\dot{r}^2 < 0$ , which is impossible. This region is forbidden for equatorial photon motion.
- ✿ if  $E < 0$  – this photon does not exist since  $E$  is a strictly positive quantity [24].

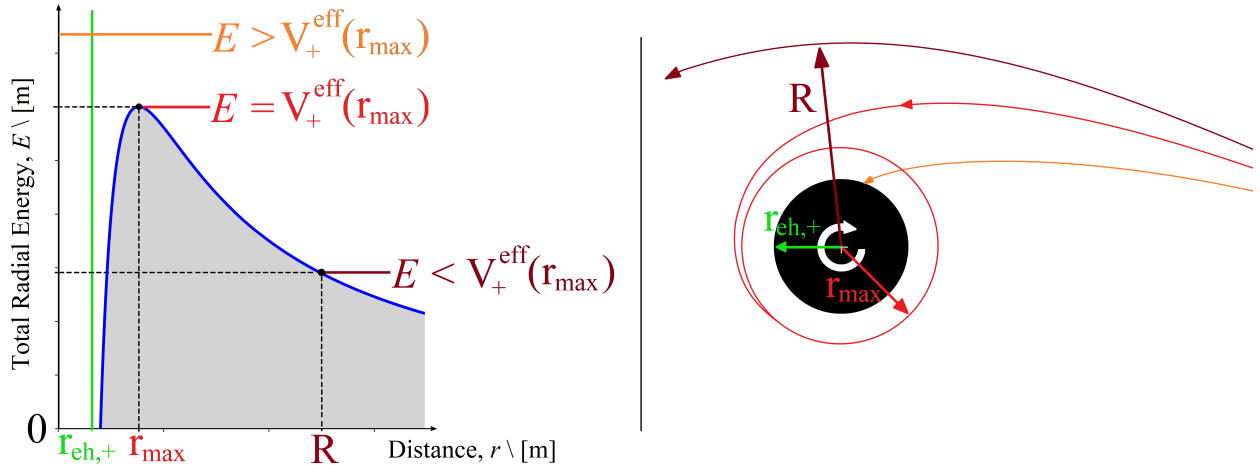


Figure 18: Visualisation of photon trajectories for three distinct values of the total radial energy,  $E$ . The blue curve on the plot corresponds to  $V_+^{\text{eff}}(r)$  for the counter-rotating case. The colour of each energy level corresponds to a photon trajectory on the RHS.

Unfortunately, using the effective potential in equation 69 to deduce the radius of the unstable equatorial orbits is not an elegant procedure. In a nutshell, this approach requires us to differentiate  $V_+^{\text{eff}}(r)$  and set it equal to zero at the photon orbit  $r = r_{\text{ps}}$ . This will yield a high-degree polynomial in  $r_{\text{ps}}$ , whose roots can be found using non-trivial analytical or numerical methods [18]. Instead, we shall adopt the more intuitive approach as presented

by Chandrasekhar in [17].

This method requires us to backtrack and reconsider the radial geodesic given in 67, with the condition  $\dot{r} = 0$ , to obtain the first expression:

$$0 = E^2 + \frac{2m}{r_{\text{ps}}^3}(L - aE)^2 - \frac{1}{r_{\text{ps}}^2}(L^2 - a^2E^2), \quad (70)$$

which holds at the radii of the unstable photon orbits,  $r = r_{\text{ps}}$ . Differentiating with respect to  $r$  once again, and imposing the second condition for circular motion  $\ddot{r} = 0$ , will provide us with a second expression:

$$0 = -\frac{6m}{r_{\text{ps}}^4}(L - aE)^2 + \frac{2}{r_{\text{ps}}^3}(L^2 - a^2E^2). \quad (71)$$

Examining the latter equation further, we deduce an initial result:

$$0 = \frac{1}{r_{\text{ps}}^4} [-6m(L - aE)^2 + 2r_{\text{ps}}(L^2 - a^2E^2)], \text{ with } r_{\text{ps}} \neq 0$$

$$\begin{aligned} 2r_{\text{ps}}(L^2 - a^2E^2) &= 6m(L - aE)^2 \\ \implies r_{\text{ps}} &= 3m \frac{L - aE}{L + aE}. \end{aligned} \quad (72)$$

Although this is an exact result, it is not particularly useful in practice because the constants of motion,  $E$  and  $L$ , are not trivial quantities to measure. This result would prove more useful once  $r_{\text{ps}}$  is expressed solely as a function of  $a$ . To remove this dependence, we can substitute the initial expression for  $r_{\text{ps}}$  into equation 70 to deduce:

$$\begin{aligned} 0 &= E^2 + \frac{2m}{r_{\text{ps}}^3}(L - aE)^2 - \frac{1}{r_{\text{ps}}^2}(L^2 - a^2E^2) \\ &= E^2 + 2m(L - aE)^2 \left[ \frac{L + aE}{3m(L - aE)} \right]^3 - (L^2 - a^2E^2) \left[ \frac{L + aE}{3m(L - aE)} \right]^2 \\ &= E^2 + \frac{(L + aE)^2}{9m^2(L - aE)} \left[ \frac{2}{3}(L + aE) - \frac{L - a^2E^2}{L - aE} \right] = E^2 - \frac{(L + aE)^3}{27m^2(L - aE)} \\ \implies 0 &= 27m^2(L - aE)E^2 - (L + aE)^3. \end{aligned} \quad (73)$$

From the previous section, we may invoke the definition of the impact parameter,  $b := \frac{L}{E}$ , which will help simplify our cubic in  $\frac{L}{E}$  to:

$$(b + a)^3 - 27m^2(b + a) + 54am^2 = 0.$$

This cubic is characterised as having two complex and one real root, with only the real root being of physical relevance. This root will be of the form [17]:

$$b = \begin{cases} -6m \cos(\theta + \frac{2\pi}{3}) - a & \text{and } \cos 3\theta = \frac{a}{m}, \text{ if } a \geq 0 \\ 6m \cos \theta - a & \text{and } \cos 3\theta = \frac{|a|}{m}, \text{ if } a < 0 \end{cases}$$

Finally, by substituting this value of the impact parameter into equation 72, we obtain the radii of the two equatorial photon orbits as [17, 24, 28, 63]:

$$r_{\text{ps},\pm} = 2m \left\{ 1 + \cos \left[ \frac{2}{3} \arccos \left( \pm \frac{a}{m} \right) \right] \right\}, \quad (74)$$

with the plus case corresponding to the counter-rotating equatorial orbits, and the minus case for the co-rotating.

By setting  $m = 1$ , we can visually study the radial distance of the equatorial orbital radii and event horizons as functions of  $a$ . Figure 19 includes the two photon orbits in red and blue, and the two event horizons in black and orange. In the limiting case for  $a$ :

- ✿  $a = m$ : we find that the counter-rotating orbit asymptotically increases in size until its maximal value of  $r_{\text{ps},+} = 4m$ , while the co-rotating becomes incident with the two event horizons at  $r_{\text{ps},-} = m$ .
- ✿  $a = 0$ : the system reduces to the Schwarzschild spacetime. In this case, the inner horizon is at  $r_{\text{eh},-} = 0$ , and the outer is at the Schwarzschild radius  $r_{\text{eh},+} = 2m$ . There is only one circular orbit at  $r_{\text{ps},\pm} = 3m$ .

**Remark 5.5.** In general, the frame-dragging effect is not uniform around the BH. In fact, it is strongest for equatorial orbits, and weakest for polar ones, as can be visually deduced from the size of the ergosphere in figure 16. This claim can easily be verified analytically by considering the angular velocity of a zero-angular-momentum observer (ZAMO) who is co-rotating with the BH.

To quantify the strength of the frame-dragging effect, we may use a ZAMO.

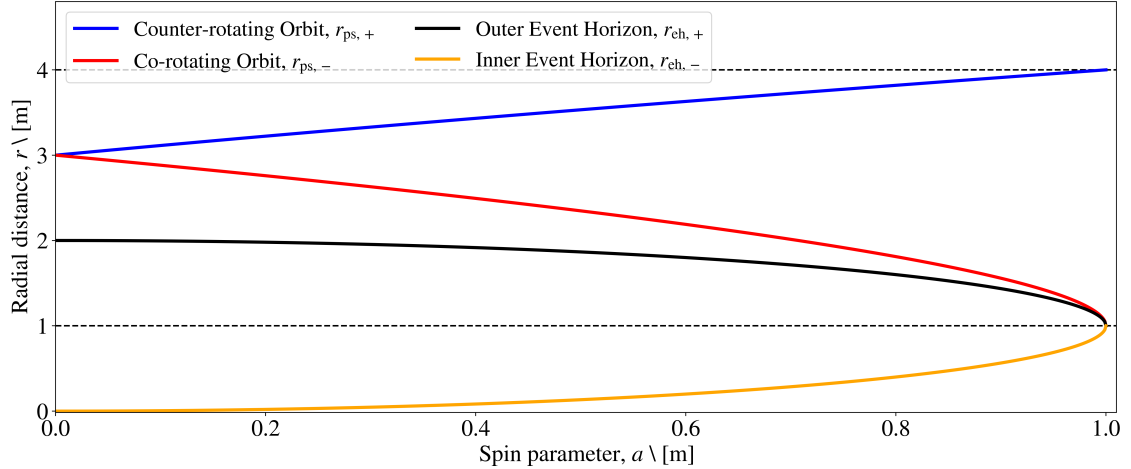


Figure 19: Plot of radial distance for equatorial photon orbits,  $r_{ps,\pm}$ , and event horizons,  $r_{eh,\pm}$ , against the spin parameter,  $a$ , for a Kerr BH of geometric mass  $m = 1$ . The program used to plot this figure can be found in appendix B.7.

**Definition 5.2.** A Zero Angular Momentum Observer (ZAMO) is an observer whose trajectory in spacetime has a constant null angular momentum,  $L \equiv 0$ .

Consider a ZAMO in circular orbit around the BH with a 4-velocity  $u^\mu$ , and a constant of motion  $L = 0$ . Then, by generalising equation 58 to non-equatorial orbits, we can obtain the exact angular velocity,  $\frac{d\phi}{dt}$ , for every circular orbit. Removing the restriction  $\theta = \frac{\pi}{2}$  allows us to derive a ZAMO's angular velocity as [52]:

$$\begin{aligned} 0 = L &\equiv g_{\phi t} \dot{t} + g_{\phi\phi} \dot{\phi} \\ \implies \Omega_{\text{ZAMO}} &:= \frac{\dot{\phi}}{\dot{t}} = -\frac{g_{\phi t}}{g_{\phi\phi}}, \end{aligned} \quad (75)$$

or, more explicitly [15, 17, 52]:

$$\Omega_{\text{ZAMO}} := \frac{2mra}{(r^2 + a^2)^2 - a^2 \sin^2 \theta}, \quad (76)$$

which can be verified to be maximal on the equator with  $\theta = \frac{\pi}{2}, \frac{3\pi}{2}$ , and minimal at poles with  $\theta = 0, \pi$ . This striking result motivates us to generalise the discussion on null geodesics beyond simply the equatorial case.

### 5.2.3 General Photon Orbits

As we have already hinted at in the previous section, there is another constant of motion associated with the Kerr spacetime – the Carter constant.

**Definition 5.3.** The Carter constant,  $K$ , is the third constant of motion in the Kerr spacetime. It is given as:

$$K := p_\theta^2 + \left( \frac{L^2}{\sin^2 \theta} - a^2 E^2 \right) \cos^2 \theta, \quad \text{with } p_\theta := \frac{\partial \mathcal{L}}{\partial \dot{\theta}} = \rho^2 \dot{\theta} \quad (77)$$

Unlike the previous constants of motion, the Carter constant is not attached to any physical property, despite representing a conservation law. This is because it is not related to a spacetime symmetry, and hence, not associated with a Killing vector field [17, 18, 38, 68]. Instead, the Carter constant is associated with a symmetric rank-two Killing tensor field,  $K^{\mu\nu}$ , which can be shown to satisfy the rank-two Killing equation [17]:

$$\nabla_{(\alpha} K_{\mu\nu)} = 0. \quad (78)$$

While the derivation of this constant is beyond the scope of this section, this can usually be shown through the separability of the Hamilton-Jacobi equation, as is thoroughly discussed in [17, 46].

**Remark 5.6.** We may also proceed by using the *modified Carter constant*:

$$\mathcal{K} := K + (L - aE)^2, \quad (79)$$

which has the properties of being [16, 17, 18, 38, 46]:

⌘ Always non-negative. Since  $p_\theta^2, \cos^2 \theta \geq 0$ , then we can show that:

$$\begin{aligned} (L - aE)^2 &\geq \left| p_\theta^2 + \left( \frac{L^2}{\sin^2 \theta} - a^2 E^2 \right) \cos^2 \theta \right| \equiv |K| \geq 0 \\ \implies (L - aE)^2 &\geq -K \quad \therefore \mathcal{K} \geq 0 \end{aligned}$$

⌘ A constant of motion. Since it is derived from other constants  $E, L$ , and  $K$ .

Lastly, one may note that the Carter constant was not introduced in the section on equatorial orbits since it was trivially zero on every equatorial orbit. There are other non-equatorial orbits which are also characterised by  $K = 0$  as discussed in [18].

By keeping  $\theta$  variable in the Kerr metric and following the same procedure outlined in the previous section, we will arrive at the following general null geodesic equations [17, 18, 38, 52]:

$$\rho^2 \dot{t} = \frac{1}{\Delta} [E(r^2 + a^2)^2 - 2mrLa] - a^2 E \sin^2 \theta \quad (80)$$

$$\rho^4 \dot{r}^2 = R(r) \quad (81)$$

$$\rho^4 \dot{\theta}^2 = \Theta(\theta) \quad (82)$$

$$\rho^2 \dot{\phi} = \frac{L}{\sin^2 \theta} + \frac{a}{\Delta} (2mrE - aL), \quad (83)$$

where  $\rho$  and  $\Delta$  have the usual meanings, and

$$R(r) = -K\Delta + [(r^2 + a^2)E - aL]^2 \quad (84)$$

$$\Theta(\theta) = K - \left( \frac{L}{\sin \theta} - aE \sin \theta \right)^2. \quad (85)$$

The geodesic equations involving  $\dot{t}$  and  $\dot{\phi}$  will not be used in our analysis as they do not reveal any particular features about the photon orbits [17]. By once again imposing  $\dot{r} = 0 = \ddot{r}$ , for spherical orbits with  $r = \text{constant}$ , we use equation 81 and its derivative under these conditions to obtain:

$$\dot{r} = 0 = R(r) := -K\Delta + [(r^2 + a^2)E - aL]^2, \quad (86)$$

and

$$\begin{aligned} \ddot{r} = 0 &= \frac{d}{dr} R(r) = -K(2r - 2m) + 2[(r^2 + a^2)E - aL](2rE) \\ &\implies 0 = -K(r - m) + 2rE [(r^2 + a^2)E - aL]. \end{aligned} \quad (87)$$

From here, we can subtract  $(\frac{r-m}{\Delta})$  times equation 86 from equation 87 to obtain:

$$\begin{aligned}
 0 &= \frac{(r-m)}{\Delta} \left\{ -K\Delta + [(r^2 + a^2)E - aL]^2 \right\} \\
 &\quad - \left\{ -K(r-m) + 2rE [(r^2 + a^2)E - aL] \right\} \\
 0 &= \left\{ \frac{[(r^2 + a^2)E - aL]}{\Delta} \right\} [(r-m) [(r^2 + a^2)E - aL] - 2rE\Delta] \\
 \implies 2rE\Delta &= (r-m) [(r^2 + a^2)E - aL], \text{ since leading term is non-zero} \\
 \implies \xi(r) &:= \frac{L}{E} = \frac{1}{a} \left[ r^2 + a^2 - \frac{2r\Delta(r)}{r-m} \right]. \tag{88}
 \end{aligned}$$

The equivalence between the impact parameter for equatorial orbits,  $b$ , and the newly defined impact parameter  $\xi(r)$  can be drawn. The different symbol is used for the sole purpose of staying consistent with present-day literature [17, 18, 46]. Another similar impact parameter can be deduced by substituting 88 back into 87 to obtain:

$$\begin{aligned}
 0 &= -K(r-m) + 2rE \left[ (r^2 + a^2) - a \frac{L}{E} \right] E \\
 &= -K(r-m) + 2rE \left[ \frac{2r\Delta}{r-m} \right] E \\
 \implies \eta(r) &:= \frac{K}{E^2} = \frac{4r^2\Delta(r)}{(r-m)^2}. \tag{89}
 \end{aligned}$$

The pair of impact parameters  $(\xi(r), \eta(r))$  will replace the sole impact parameter,  $b(r)$ , which was reserved for spherically symmetric spacetimes and planar photon orbits. As was previously the case, these impact parameters will aid in distinguishing the nature of the past-emitted photon rays. In particular, there exist critical values for  $(\xi(r), \eta(r))$ , say  $(\xi_c, \eta_c)$ , for which the past-emitted photons will spiral asymptotically into an unstable circular orbit. For values smaller than the critical, the photons will impinge on the surface of the BH, and for values greater, they will recede to infinity.

**Remark 5.7.** We can generally interpret  $\xi(r)$  as quantifying a photon's motion about the BH's rotational axis since it is dependent on  $L$ . Similarly,  $\eta(r)$  usually quantifies the motion in the  $\theta$  direction due to the presence of the Carter constant, which vanishes along the equatorial plane.

Unlike the equatorial case, general photon orbits are possible in an enclosed region around the BH. The width of this region depends on the inclination angle  $\theta$ . Spherical photon orbits are typically allowed whenever  $\Theta(\theta) \geq 0$ , so that  $\dot{\theta} \in \mathbb{R}$  (from equation 82). More explicitly, this condition implies that photon orbits exist as long as:

$$\begin{aligned}\Theta(\theta) &= K - \left( \frac{L}{\sin \theta} - aE \sin \theta \right)^2 \geq 0 \\ K &- \frac{E^2}{a^2 \sin^2 \theta} \left( \frac{aL}{E} - a^2 \sin^2 \theta \right)^2 \geq 0 \\ a^2 \sin^2 \theta \left[ \frac{4r^2 \Delta}{(r-m)^2} \right] &- \left[ \left( r^2 + a^2 - \frac{2r\Delta}{r-m} \right) - a^2 \sin^2 \theta \right]^2 \geq 0 \\ \implies 4r^2 \Delta a^2 \sin^2 \theta &\geq [\rho^2(r-m) - 2r\Delta]^2.\end{aligned}\quad (90)$$

This expression defines a sextic polynomial whose roots in  $r$  will indicate the radial distance of the  $r = \text{constant}$ , spherical photon orbits. These orbits will naturally oscillate between a minimum and maximum value of  $\theta$ , since they are not planar and have a non-zero Carter constant [46].

It is generally known, through the Abel-Ruffini theorem [49], that the solution of a polynomial with a degree higher than 4 in radicals is impossible. However, this does not prevent us from obtaining numerical solutions for the roots of 90, as will be done further on. Furthermore, this issue has fortunately been resolved for certain special cases such as equatorial orbits ( $\theta = \frac{\pi}{2}$ ), polar orbits ( $\theta = 0$ ), and a small number of subcases as discussed in [18, 63], where analytical expressions for the radii of null geodesics were obtained.

For a non-extremal Kerr BH ( $|a| < m$ ), the photon region is separated into three distinct components. However, only one of these photon regions will be external to the outer event horizon with  $r > r_{\text{eh},+}$ . The other two will be located inside  $r_{\text{eh},+}$ , and therefore remain hidden from the observer. Although the interior region admits both stable and unstable photon orbit configurations, the outer photon region only allows the existence of unstable photon orbits. This fact can be verified by considering the second derivative of 81 to show

that  $\frac{d^2R(r)}{dr^2} < 0$  in the exterior photon region.

Figures 20 and 21 were plotted as an extension to figure 16, with the addition of the photon regions for various values of  $a$ , in pink. These regions were obtained by numerically solving the inequality in equation 90 using the `scipy` library in Python. By discretising and iterating over the values of  $\theta \in [0, 2\pi]$ , we obtain the maximum and minimum radial distances at which photon orbits can exist. When  $a \rightarrow 0$ , the photon region reduces to a single photon sphere identical to the Schwarzschild case, while as  $a \rightarrow m$ , the region intersects the ergoregion. The locus of intersection between the ergoregion and photon region will not be studied; however, a suitable discussion can be found in [44].

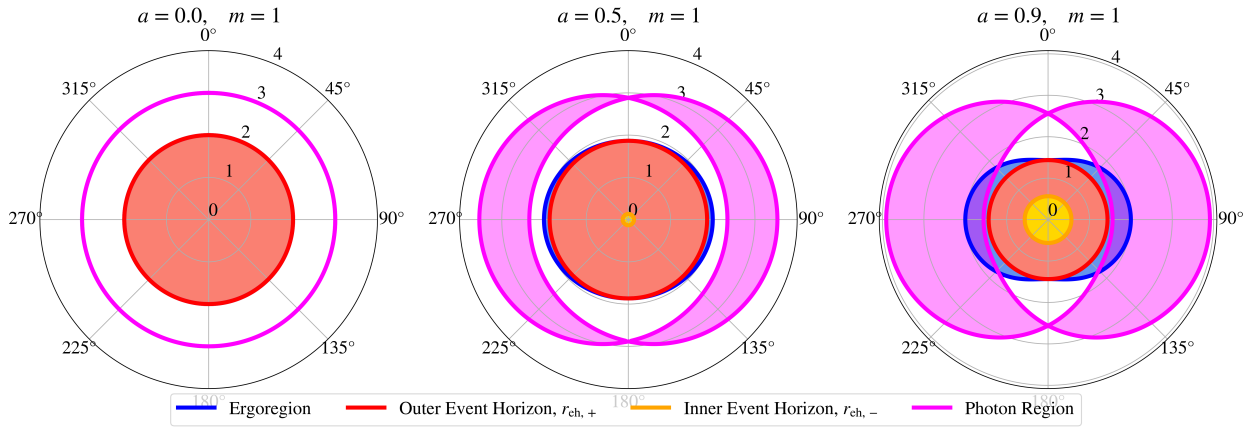


Figure 20: The important surfaces of a Kerr BH, together with a corresponding photon region, in Boyer-Lindquist coordinates. The volume encapsulated by the photon regions (in pink) was obtained numerically by following [27, 44, 46]. The boundary of the photon region is characterised by  $\Theta(\theta) = 0$ . The program used to plot this figure can be found in appendix B.8.

Figure 22 shows three examples of spherical orbits found in the photon region of a Kerr BH. These were obtained numerically through the `Black Hole Perturbation Toolkit` package in Mathematica [1]. By projecting the image of all such spherical orbits found in this region onto an observer's sky, we will obtain the boundary curve of the Kerr BH shadow.

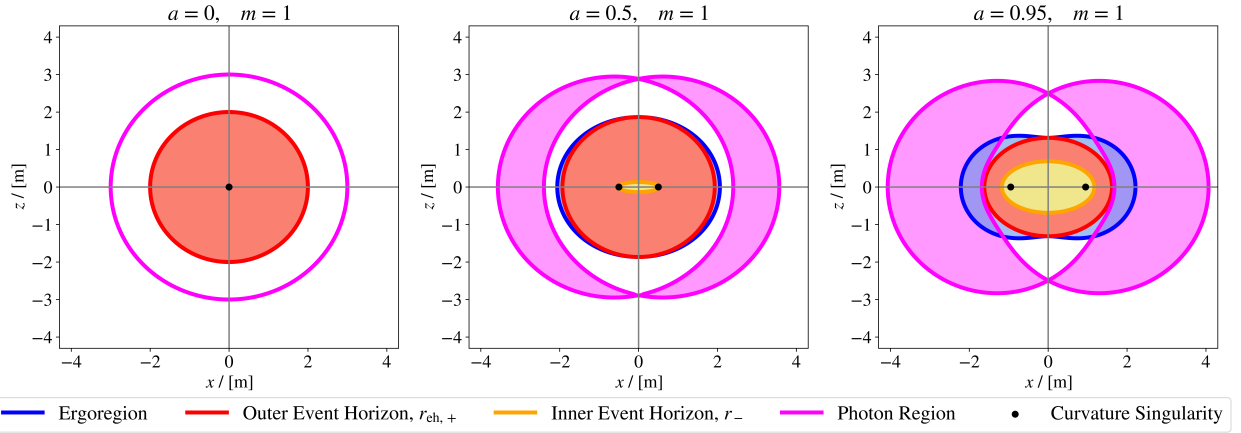


Figure 21: The important surfaces of a Kerr BH in Kerr-Schild coordinates. The plot is obtained by transforming the surfaces in figure 20 using equation 49. The program used to plot this figure can be found in appendix B.8.

### 5.2.4 BH shadow in Kerr spacetime

Consider a ZAMO co-rotating with the BH and located at the spatial coordinates  $(r_O, \theta_O)$  in Boyer-Lindquist coordinates, where  $r_O \gg m$  denotes the observer's radial distance, and  $\theta_O$  their polar inclination relative to the  $z$ -axis of the BH. From the observer's perspective, every past-emitted photon from their location can be described by a colatitude angle,  $\gamma$ , and an azimuthal angle,  $\psi$ , on their celestial sphere,  $\mathbb{S}^2$  (see figures 23 and 24). Here, the colatitude has a range  $[-\frac{\pi}{2}, \frac{\pi}{2}]$  (or  $[0, \pi]$  equivalently) and measures the angle between the past-emitted photon's tangent and the local zenith direction, which is along the vector  $e_3$ . Similarly, the azimuthal angle has a range  $[0, 2\pi]$  and specifies the angle between the photon's tangent and the fixed vector  $e_1$ . With respect to these angles, the direction of  $e_3$  corresponds to the celestial angle  $\gamma = 0$ , and  $e_1$  corresponds to  $\psi = 0$ .

To map photon directions in terms of  $(\gamma, \psi)$  onto the observer's sky, we project the tangent vector of the photon path onto a local orthonormal tetrad [68].

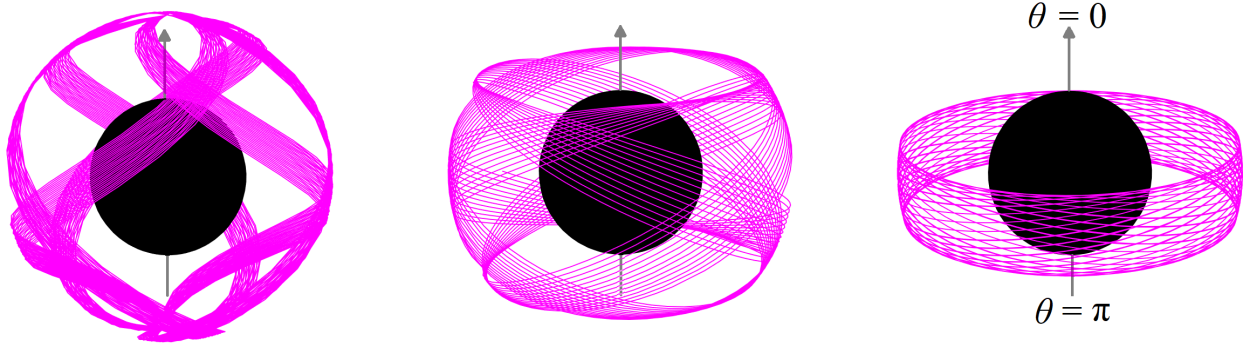


Figure 22: Three different spherical photon orbits around a Kerr BH with  $a = 0.9m$  and  $m = 1$ . The black circle corresponding to the BH itself is not to scale! The orbits have different bounds on their inclination angle  $\theta$  – as measured from the axis of rotation (grey arrow). The LHS plot has  $\theta \in [0, \pi]$ , the middle has  $\theta \in [\frac{3\pi}{10}, \frac{7\pi}{10}]$ , and the RHS has  $\theta \in [\frac{3\pi}{7}, \frac{4\pi}{7}]$ . Since the photon paths do not start and end at the same point, 60 revolutions around the BH were plotted.

**Definition 5.4.** A tetrad (vierbein) is a local orthonormal reference frame for an observer in spacetime. Every tetrad  $\{e_0, e_1, e_2, e_3\}$  has a timelike vector  $e_0$ , and a spacelike basis for 3-space  $\{e_1, e_2, e_3\}$  satisfying:

$$g_{\mu\nu} e_{(i)}^\mu e_{(j)}^\nu = \eta_{ij},$$

where  $\eta_{ij} = \text{diag}(-1, 1, 1, 1)$  is the flat spacetime metric, and  $i, j$  are the free indices.

In the context of a ZAMO in the Kerr spacetime – parametrised in terms of Boyer-Lindquist coordinates, we use the tetrad [27, 46, 47, 63]:

$$e_0 = \left[ \frac{r^2 + a^2}{\sqrt{\rho^2 \Delta}} \partial_t + \frac{a}{\sqrt{\rho^2 \Delta}} \partial_\phi \right]_{(r_O, \theta_O)}, \quad e_1 = \frac{1}{\sqrt{\rho^2}} \partial_\theta \Big|_{(r_O, \theta_O)} \quad (91)$$

$$e_2 = \left[ -\frac{a \sin^2 \theta}{\sqrt{\rho^2 \Delta}} \partial_t - \frac{1}{\sqrt{\rho^2 \Delta}} \partial_\phi \right]_{(r_O, \theta_O)}, \quad e_3 = -\sqrt{\frac{\Delta}{\rho^2}} \partial_r \Big|_{(r_O, \theta_O)} \quad (92)$$

The motivation behind the use of this specific tetrad comes from several factors. Firstly, the timelike vector  $e_0$  is equivalent to the observer's four-velocity. Secondly, the vector  $e_3$  is spatially along the direction of the BH's centre. Lastly, the observer remains a ZAMO in this coordinate system. By combining the first two motivating factors, we deduce that the

vector  $e_0 \pm e_3$  is tangential to the principal null ray. This is embodied by an ingoing photon ray with a colatitude  $\gamma = 0$  for the plus case, and an outgoing photon ray with  $\gamma = \pi$  for the minus case [27]. Figures 23 and 24 illustrate the tetrad system and the observer's celestial coordinates, respectively.

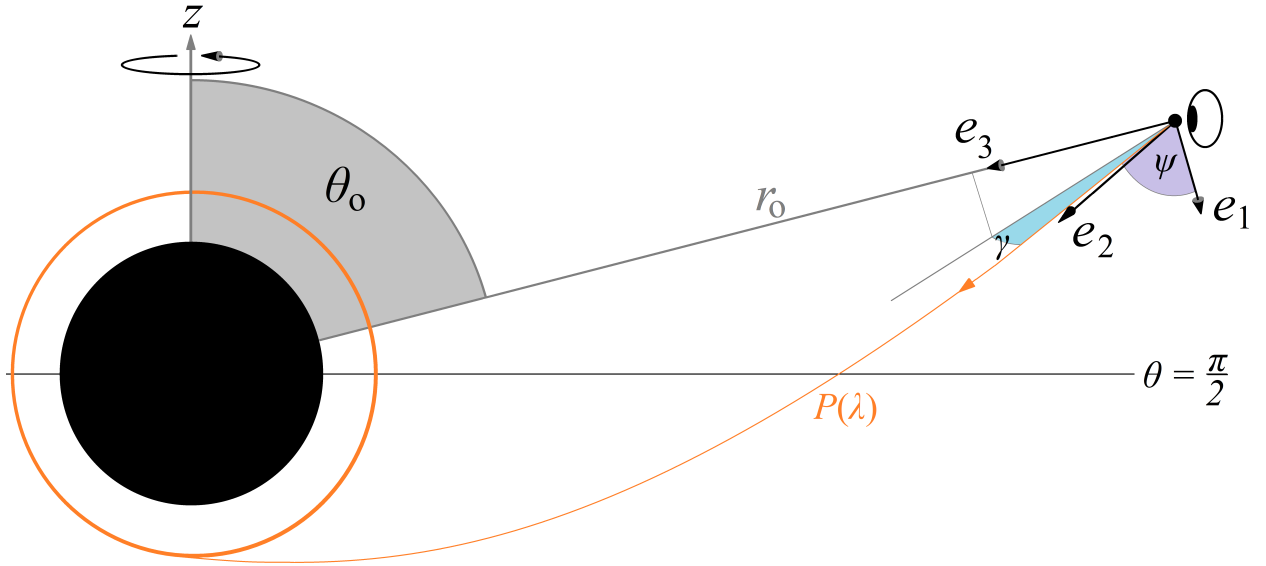


Figure 23: A distant observer at spatial coordinates  $(r_0, \theta_0)$  with respect to a Kerr BH rotating about the  $z$ -axis. The three spatial axes  $\{e_1, e_2, e_3\}$  belonging to the distant observer are also depicted together with a past-emitted photon ray with celestial coordinates  $(\gamma, \psi)$ , which spirals into unstable spherical orbit at some fixed  $r = r_{ps}$ . Such photons will be used to construct the BH shadow. The diagram is adapted from figure 7 in [27].

In our selected  $(t, r, \theta, \phi)$  coordinate system, every photon path  $\mathcal{P}(\lambda)$ , parametrised by an affine parameter  $\lambda$ , will have a tangent vector given by [26, 27]:

$$\dot{\mathcal{P}}(\lambda) = \dot{t} \partial_t + \dot{r} \partial_r + \dot{\theta} \partial_\theta + \dot{\phi} \partial_\phi, \quad (93)$$

which, in our tetrad formalism, will be equivalent to stating the tangent vector in terms of

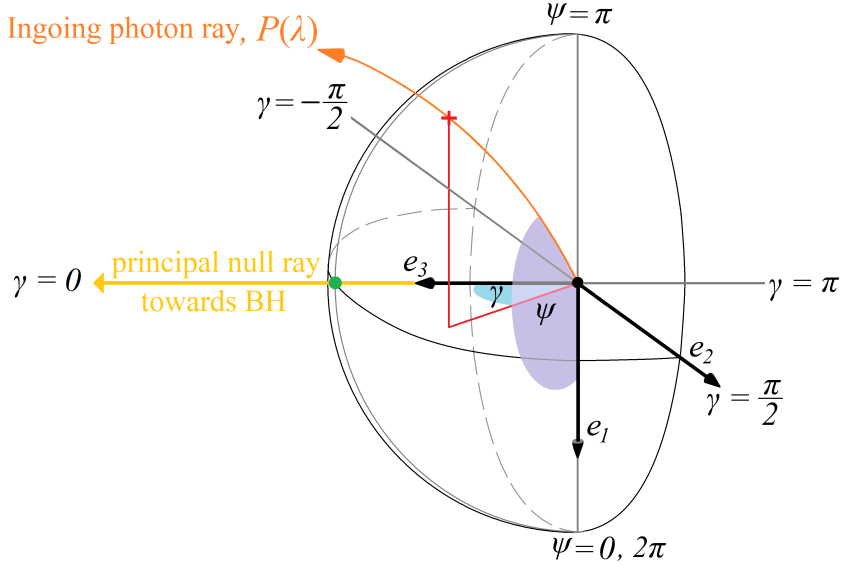


Figure 24: The parametrisation of an observer’s sky,  $\mathbb{S}^2$ . Every past-emitted photon ray has associated celestial coordinates  $(\gamma, \psi)$ . Some directions corresponding to specific values of  $\gamma$  and  $\psi$  are also depicted to aid the visualisation. The diagram is adapted from figure 8 in [27].

the pair of celestial coordinates  $(\gamma, \psi)$  on our observer’s sky as [26, 27]:

$$\begin{aligned} \dot{\mathcal{P}}(\lambda) &= \alpha(-e_0 + e_1 \sin \gamma \cos \psi + e_2 \sin \gamma \sin \psi + e_3 \cos \gamma) \\ &= \alpha \left\{ - \left[ \frac{r^2 + a^2}{\sqrt{\rho^2 \Delta}} \partial_t + \frac{a}{\sqrt{\rho^2 \Delta}} \partial_\phi \right]_{(r_O, \theta_O)} + \sin \gamma \cos \psi \left[ \frac{1}{\sqrt{\rho^2}} \partial_\theta \right]_{(r_O, \theta_O)} + \right. \\ &\quad \left. \sin \gamma \sin \psi \left[ -\frac{a \sin^2 \theta}{\sqrt{\rho^2 \Delta}} \partial_t - \frac{1}{\sqrt{\rho^2 \Delta}} \partial_\phi \right]_{(r_O, \theta_O)} + \cos \gamma \left[ -\sqrt{\frac{\Delta}{\rho^2}} \partial_r \right]_{(r_O, \theta_O)} \right\}, \end{aligned} \quad (94)$$

with the scaling factor being equal to the projection of the tangent vector on the timelike component  $e_0$ :

$$\alpha := g_{\mu\nu} \dot{\mathcal{P}}(\lambda)^\mu e_0^\nu = \frac{aL - (r^2 + a^2)E}{\sqrt{\rho^2 \Delta}},$$

linking the two coordinate systems together. To avoid complicating matters, we will directly compare the coefficients of the two directional derivatives,  $\partial_r$  and  $\partial_\phi$ , to find explicit

relationships for  $(\gamma, \psi)$ . We start by comparing  $\partial_r$  from 93 and 94:

$$\begin{aligned} -\alpha \sqrt{\frac{\Delta}{\rho^2}} \cos \gamma &= \dot{r} \\ \cos \gamma &= -\sqrt{\frac{\rho^2}{\Delta}} \left[ \frac{\sqrt{\rho^2 \Delta}}{aL - (r^2 + a^2)E} \right] \dot{r}, \text{ using definition of } \alpha \\ \cos \gamma &= -\frac{\dot{r} \rho^2}{aL - (r^2 + a^2)E} \\ \implies \cos \gamma &= \frac{\sqrt{K\Delta - [(r^2 + a^2)E - aL]^2}}{(r^2 + a^2)E - aL}, \text{ using equation 81.} \end{aligned}$$

Geometrically, a right-angled triangle with an adjacent of  $\sqrt{K\Delta - [(r^2 + a^2)E - aL]^2}$  and hypotenuse of  $(r^2 + a^2)E - aL$ , will have an opposite side of length  $\sqrt{K\Delta}$ . Hence, we may also write

$$\begin{aligned} \sin \gamma &= \frac{\sqrt{K\Delta}}{(r^2 + a^2)E - aL} \\ \implies \sin \gamma(r) &= \frac{\sqrt{\eta(r)\Delta(r)}}{r^2 - a\xi(r) + a^2}, \text{ after dividing by } E. \end{aligned} \quad (95)$$

Similarly, for the more cumbersome coefficient of  $\partial_\phi$ , we find:

$$\sin \psi(r) = \frac{\xi(r) - a \sin^2 \theta_O}{\sin \theta_O \sqrt{\eta(r)}}. \quad (96)$$

**Remark 5.8.** For every azimuthal angle  $\psi \in [0, 2\pi)$  (equivalently  $(-\frac{\pi}{2}, \frac{3\pi}{2}]$ ) on the observer's celestial sphere  $\mathbb{S}^2$ , there exists a unique spherical orbit at a fixed radius  $r = r_{ps}$  around the BH, towards which a photon with some suitable colatitude  $\gamma$ , will spiral asymptotically into unstable orbit [27] (see figure 23).

Under standard time flow, a photon emitted from a spherical orbit towards the observer will create a single bright point on their celestial sky. Due to the axisymmetry of the Kerr spacetime, the shadow will actually be identical in the azimuthal intervals  $[-\frac{\pi}{2}, \frac{\pi}{2}]$  and  $[\frac{\pi}{2}, \frac{3\pi}{2}]$ , corresponding to the lower-half and upper-half, respectively. In either of these intervals, the shadow is a continuous curve over  $\mathbb{S}^2$  that accepts every value of  $\psi$ . To obtain the entire boundary curve of the BH shadow on the observer's sky, we may proceed in one of two ways.

Firstly, we may choose to vary  $\psi \in [-\frac{\pi}{2}, \frac{\pi}{2}]$  and invert equation 96 to derive the unique photon sphere radius  $r = r_{\text{ps}}(\psi)$ , for this value of  $\psi$ . Substituting  $r_{\text{ps}}(\psi)$  in equation 95 will yield the second celestial angle  $\gamma(r_{\text{ps}}(\psi))$ . This procedure gives the parametrised curve  $(\sin \gamma(\psi), \sin \psi)$  on the observer's celestial sphere.

The second method involves deducing the smallest ( $r_{\text{ps, min}}$ ) and largest ( $r_{\text{ps, max}}$ ) radius of the photon region's extent (solid pink outline in diagram 20), and parametrising the boundary curve  $(\sin \gamma(r_{\text{ps}}), \sin \psi(r_{\text{ps}})) \subset \mathbb{S}^2$  by varying  $r_{\text{ps}} \in [r_{\text{ps, min}}, r_{\text{ps, max}}]$ . To deduce these extremal radii, we may note from equation 96 that a maximal radius is obtained when  $\psi = -\frac{\pi}{2}$ , and a minimal when  $\psi = \frac{\pi}{2}$  [26, 27, 47]. This leads to the conditions:

$$\underbrace{\sin \psi(r_{\text{ps, min}})}_{=\frac{\pi}{2}} = 1, \quad \text{and} \quad \underbrace{\sin \psi(r_{\text{ps, max}})}_{=-\frac{\pi}{2}} = -1, \quad (97)$$

which, when solved numerically through equation 96, will yield the required extremal orbital radii. Throughout the following discussion, the latter method will be adopted because it is easier to implement and is personally more intuitive.

Before we are able to proceed, we must obtain explicit expressions for our impact parameters,  $\xi(r)$  and  $\eta(r)$ , since they are dependent on each individual photon orbit being considered. According to equations 88 and 89, the constants of motion take the form [47]:

$$\begin{aligned} \eta(r_{\text{ps}}) &= \frac{4r_{\text{ps}}^2 \Delta(r_{\text{ps}})}{(r_{\text{ps}} - m)^2} \\ &= \frac{4r_{\text{ps}}^2(r_{\text{ps}}^2 - 2mr_{\text{ps}} + a^2)}{(r_{\text{ps}} - m)^2}, \end{aligned} \quad (98)$$

and,

$$\begin{aligned} \xi(r_{\text{ps}}) &= \frac{1}{a} \left[ r_{\text{ps}}^2 + a^2 - \frac{2r_{\text{ps}} \Delta(r_{\text{ps}})}{r_{\text{ps}} - m} \right] \\ &= \frac{-r_{\text{ps}}^2(r_{\text{ps}} - 3m) - r_{\text{ps}} a^2 - a^2 m}{a(r_{\text{ps}} - m)}, \end{aligned} \quad (99)$$

on every photon orbit  $r_{\text{ps}} \in [r_{\text{ps, min}}, r_{\text{ps, max}}]$ .

At this point, we are stuck with the analytic boundary curve  $(\sin \gamma(r_{\text{ps}}), \sin \psi(r_{\text{ps}})) \subset \mathbb{S}^2$  located on the observer's celestial sphere, which represents the BH shadow. This, however, is still not possible to visualise on a 2d diagram, unless it is first transformed via a planar projection  $\mathbb{S}^2 \rightarrow \mathbb{R}^2$ . This motivates the use of a stereographic projection to map the celestial sky onto a plane that is spatially orthogonal to  $e_3$  (the principal null ray), and tangential to the sphere at  $\gamma = 0$  (green dot in figure 24). This is done by using the dimensionless Cartesian coordinates [17, 27, 47]:

$$x(r_{\text{ps}}) = -2 \tan\left(\frac{\gamma(r_{\text{ps}})}{2}\right) \sin \psi(r_{\text{ps}}), \quad \text{and} \quad y(r_{\text{ps}}) = -2 \tan\left(\frac{\gamma(r_{\text{ps}})}{2}\right) \cos \psi(r_{\text{ps}}) \quad (100)$$

Finally, this allows us to visualise the Kerr BH shadow. Since there are four parameters  $(r_0, \theta_0, a, m)$  which influence the shape and size of the shadow, their dependence has been individually depicted in figure 25. In each of the four subplots, the origin  $(0,0)$  corresponds to the spatial direction towards the BH ( $\gamma = 0$ ).

In the top-left subplot of figure 25, the mass takes values from  $\{1, 2, 5, 10, 20\}$ , with  $a = 0.999m$ ,  $r_0 = 100$ , and  $\theta_0 = \frac{\pi}{2}$  being fixed constants. In general, the shadow not only shrinks with a decreasing mass but also exhibits a less distorted shape. This distortion is attributed to the strong-field conditions associated with the fact that  $m$  and  $r$  are of comparable order, especially for  $m > 10$ . Moreover, the distortion is magnified by the near-extremal spin parameter and equatorial viewing angle.

In the top-right subplot, the mass takes a fixed value of  $m = 1$ , and the spin parameter is instead varied from the near-Schwarzschild case of  $a = 0.01m$ , to the near-extremal of  $a = 0.999m$ . It should be noted that for  $a = 0$ , equation 99 becomes singular. This is because for the Schwarzschild case,  $r_{\text{ps}, \min} = r_{\text{ps}, \max} = 3m$ , so the parametrisation fails. Regardless, arbitrarily small values of  $a$  can still be used. The diagram confirms that  $a$  is strongly correlated to the distortion of the shadow. Not only does this shadow become more blunt on one side, but it also exhibits a translation to the right.

In the bottom-left subplot, the dependence on the observer distance is studied. It can be noted that the subplot closely resembles the top-left one, where  $m$  was instead varied. Once again, the distortion of the shadow is greater when  $r_0$  and  $m$  are of comparable order, while for larger  $r_0$ , the shadow is smaller and more circular. For the Schwarzschild case  $a = 0$ , diagram 10 shows the explicit relationship between shadow size and  $r_0$ .

The dependence on the viewing angle  $\theta_0$  is shown in the bottom-right subplot. Note that when  $\theta_0 = 0$ , the observer is located along the axis of rotation, and hence observes no distortion. This, however, poses an issue since equation 96 becomes singular at for this angle. In general, as the inclination grows, the shadow deformation grows due to the increased frame-dragging effect, until the maximum deformation is encountered at  $\theta_0 = \frac{\pi}{2}$ . There is also a small growth in the shadow size as the observer approaches the equatorial plane.

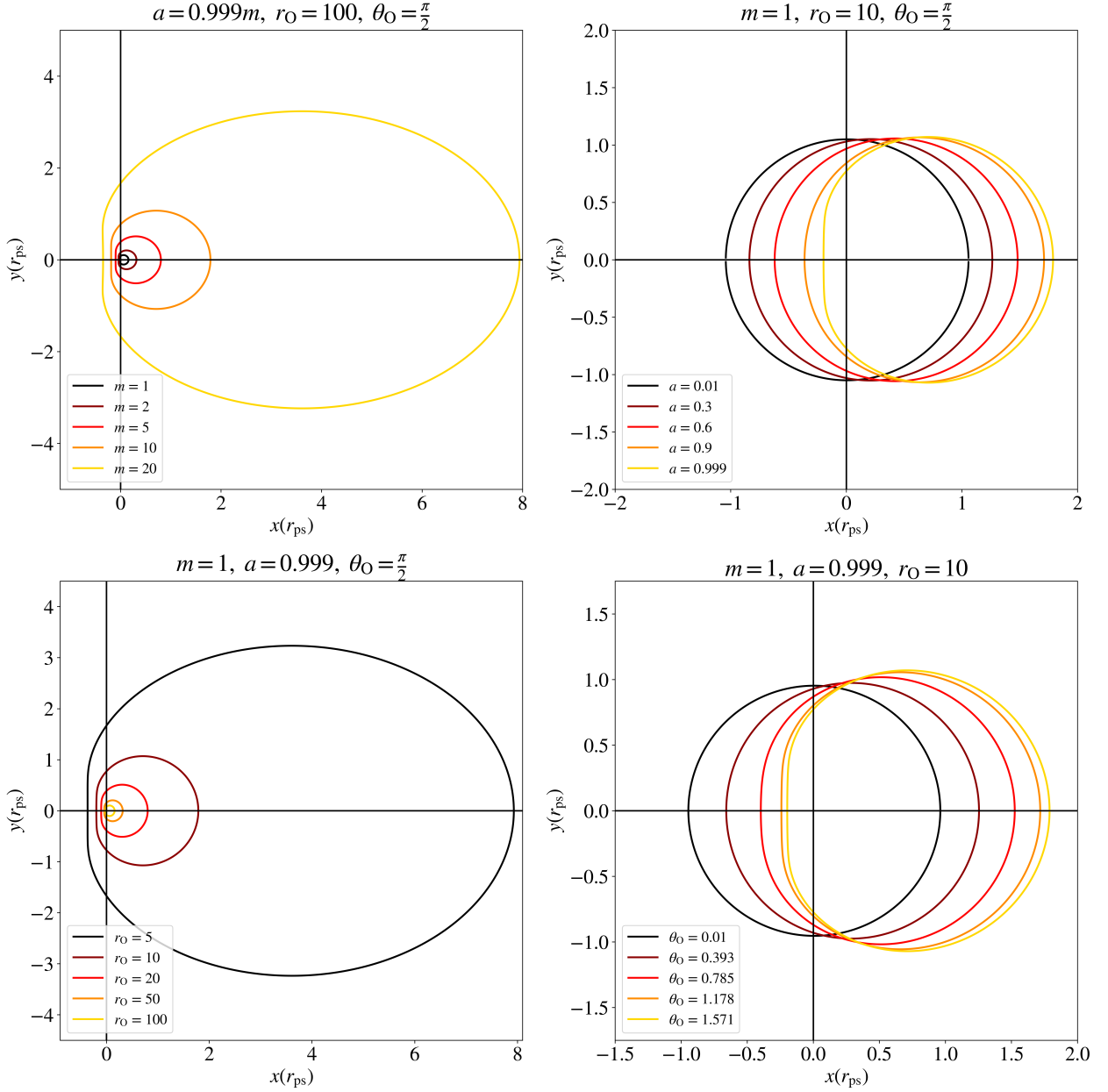


Figure 25: Four subplots each showcasing the effects of a parameter on the shape and size of the Kerr BH shadow, as seen by a ZAMO. For each subplot, three out of the four parameters ( $r_0, \theta_0, a, m$ ) were kept constant, usually in a near-extremal regime. The program used to plot this figure can be found in appendix B.9.

### 5.3 Concluding Remarks

In this lengthy section, a detailed but necessary discussion on the Kerr spacetime structure was provided. We rigorously investigated the frame-dragging effect, derived the important surfaces, and calculated the shadow size for a ZAMO. The study of photon orbits further enriched the analysis.

This discussion can be extended to several other broader cases. On one hand, we can investigate the shadow size of a Kerr BH for distant observers ( $r_O \gg m$ ), particularly by approximating equations 96 and 95, as was done for the Schwarzschild and Reissner-Nordström BH shadows. However, this is not strictly necessary, as the top-right subplot in figure 25 already illustrates the shadow for an observer at  $r_O = 10m$ , which is sufficiently far to be considered distant. Moreover, at very large distances, effects of cosmological expansion will become significant enough to render the approximation useless, given that it is unlikely to match physical reality.

Another generalisation involves extending the discussion to the class of Kerr-Newmann BHs, which describe rotating, charged singularities embedded in a static universe. Here, the charge parameter  $Q$  will certainly have an impact on the shadow size, analogous to the Reissner-Nordström case. However, this extension is also not of particular importance, as BHs are not expected to possess a significant net charge.

Without further delay, the subsequent sections will focus on cosmological BHs, with their shadows being our ultimate interest.

---

## 6 BH shadows at cosmological distances

### 6.1 The expanding universe... and the FLRW metric

So far, we have only considered solutions to the EFEs with a vanishing cosmological constant, leading to spacetimes describing a static universe (unchanging with time). The universe in reality is expanding, and it is doing so at an accelerating rate due to the presence of large amounts of dark energy. Generally, cosmic expansion has profound physical effects on the geodesics of light, significantly influencing how BH shadows appear to distant observers. Studying BHs in an expanding universe will create the most realistic picture of their appearance up to now.

Beyond the cosmic expansion, the universe also has other important characteristics which must be incorporated when devising any analytical model. In particular, when considering the large-scale structure of the universe, we observe [15, 38]:

- ✿ Homogeneity: At scales over 100 megaparsecs ( $\simeq 326$  million light years), the matter distribution of the universe becomes statistically uniform. Consequently, there is no preferred region of the universe where matter tends to reside.
- ✿ Isotropy: The properties of the universe are the same in every direction. It looks the same along any line of sight. Thus, there is no preferred observational direction.

Together, these two conditions form what is known as the Cosmological Principle (CP). Any spacetime attempting to create a realistic model of the universe must satisfy the CP.

The most general metric describing an expanding background universe that satisfies both homogeneity and isotropy was developed independently by Friedmann, Lemaître, Robertson, and Walker, hereafter abbreviated as FLRW.

**Definition 6.1.** The FLRW in the spherical coordinates  $(t, r, \theta, \phi)$  is given by [15, 38]:

$$ds^2 = -dt^2 + a(t)^2 \left( \frac{1}{1 - \kappa r^2} dr^2 + r^2 d\Omega^2 \right), \text{ with } \kappa = \frac{k}{R_0^2}, \quad (101)$$

where  $a(t) \in [0, 1]$  is a dimensionless scale factor dependent on time, and  $k$  is the curvature term which takes the values:

$$k = \begin{cases} -1 & \text{Open universe -- ve spatial curvature, infinite volume} \\ 0 & \text{Flat universe -- null spatial curvature, infinite volume} \\ 1 & \text{Closed universe -- +ve spatial curvature, finite volume} \end{cases}$$

Note that the  $R_0$  constant has units of length and denotes the current scale of the universe (not of particular importance). We set the scale factor of the present-day universe to  $a(t_O) = 1$ .

The central challenge with using the FLRW metric is determining the precise analytical form of  $a(t)$ . This requires us to account for the exact contributions due to matter (baryonic and dark), radiation, and dark energy. As it stands, there is currently no known exact form for  $a(t)$  that provides an accurate record of these contributions (starting from the Big Bang). This flaw necessitates the use of approximations, which will provide simplified models valid only at certain scales or eras of the universe. Nevertheless, such models are still very relevant to our research on BH shadows.

In particular, the two important cosmological BH spacetimes which will be discussed in this section are the Kottler and McVittie. The former describes a Schwarzschild BH embedded in a universe whose expansion is entirely dark energy-dominated via  $\Lambda$ . This leads to an asymptotically de Sitter universe, which is not representative of our universe in current times. As for the latter, the McVittie metric generalises the Kottler by being asymptotically FLRW, as opposed to de Sitter. This provides a much more realistic model of the background geometry of the universe.

Unfortunately, there is still a large gap in our understanding of BHs embedded in a realistic cosmology. This is exemplified by the severe scarcity of spacetimes which describe more complex cosmological BHs. This remains an active area of research [47, 48, 58].

## 6.2 Cosmology in brief

**Definition 6.2.** The dynamics of a homogeneous and isotropic universe are dictated by the Friedmann Equations (FE) [15, 68]. These are derived by assuming matter and energy to be modelled by a perfect fluid having a certain energy density,  $\rho \equiv -T^{00}$ , and pressure,  $p$ . The FEs are given by:

$$(FE1) \quad H(t)^2 := \left( \frac{\dot{a}(t)}{a(t)} \right)^2 = \frac{8\pi}{3} \rho(t) - \frac{k}{a(t)^2} \quad (102)$$

$$(FE2) \quad \dot{H}(t) + H(t)^2 = \frac{\ddot{a}(t)}{a(t)} = -\frac{4\pi}{3} (\rho(t) + 3p) \quad (103)$$

Here,  $H(t)$  is the Hubble parameter, with  $H_0 := \frac{\dot{a}(t_{\text{O}})}{a(t_{\text{O}})}$  denoting its modern day value.

The Hubble parameter assumes different forms in each cosmological model. For the FLRW background:

**Definition 6.3.** The Hubble parameter within the FLRW model, as a function of redshift, is defined as:

$$H(z) := H_0 [\Omega_{m0}(1+z)^3 + \Omega_{r0}(1+z)^4 + \Omega_{\Lambda0}]^{1/2}, \quad (104)$$

where  $H_0$  = constant, is the modern-day value of the Hubble parameter, and  $(\Omega_{m0}, \Omega_{r0}, \Omega_{\Lambda0})$  are the present-day density parameters of matter, radiation, and dark energy in our universe. Currently, these are observed to be  $(\Omega_{m0}, \Omega_{r0}, \Omega_{\Lambda0}) = (0.289, 2.47 \times 10^{-5}, 0.73,)$  [34]. The fact that  $\Omega_{m0} + \Omega_{r0} + \Omega_{\Lambda0} \simeq 1$  shows that the universe is flat ( $k = 0$ ).

It should be noted that the interstellar pressure,  $p$ , is related to the energy density through

the equation of state:

$$p = w\rho, \quad (105)$$

with  $|w| \leq 1$  being a constant of proportionality, which, depending on the assumptions made about the contents of the universe, will take an appropriate value. A few of the main assumptions lead to:

- ⌘ Matter-dominated: Since matter is observed to be pressureless, we have  $w = 0$
- ⌘ Radiation-dominated: relativistic particles have  $w = \frac{1}{3}$
- ⌘ Dark energy-dominated: the cosmological constant implies  $w = -1$

The Hubble parameter tracks the expansion of the universe through the three cosmological parameters, and the scale factor  $a(t)$ . This implies that universal expansion is highly dependent on its matter and energy contents. The current consensus is that our universe is made up of 5% ordinary matter, 26.8% dark matter, and 68.2% dark energy [34].

The scale factor  $a(t)$  is also used to define the redshift,  $z$ . This is a ratio of the universe's scale factors at a time when a photon was emitted, and when it was received at the current time. The wavelength of the photon would shift according to this scale factor [15].

**Definition 6.4.** A photon emitted at a time  $t_{\text{emission}}$  and received at a time  $t_0$  will have a redshift of:

$$z := \frac{a(t_0)}{a(t_{\text{emission}})} - 1 \equiv \frac{1 - a(t_{\text{emission}})}{a(t_{\text{emission}})} \quad (106)$$

**Remark 6.1.** Consider a celestial body emitting photons towards us. By knowing the redshift of this object, we can determine the scale factor of the universe at the instant when the received photons were emitted from its surface.

The expansion of the universe poses problems with the measurements of distance, since physical distances are continuously being inflated. This necessitates the definition of a new measure of distance to remove some degree of measurement ambiguity. Of the many types

of distances used throughout literature, we will make use of the angular diameter distance  $d_A(z)$ . This is a measure of distance inferred from the intrinsic and observed size of an object as it appears on our sky [15, 34, 41].

**Definition 6.5.** For a body at a redshift  $z$ , the angular diameter distance is given by:

$$d_A(z) := \frac{R}{\alpha} \equiv \frac{1}{1+z} \int_0^z \frac{d\bar{z}}{H(\bar{z})} \quad (107)$$

where  $R$  is its radius,  $\alpha$  is its observed angular size on our sky, and  $H(\bar{z})$  is the Hubble parameter. See construction in diagram 26.

As the name implies,  $d_A(z)$  should naturally relate angular size with the intrinsic *diameter*, and not *radius*. However, as per our convention,  $\alpha$  actually measures half the angular size (see figure 9), so we are justified in replacing the intrinsic diameter with radius.

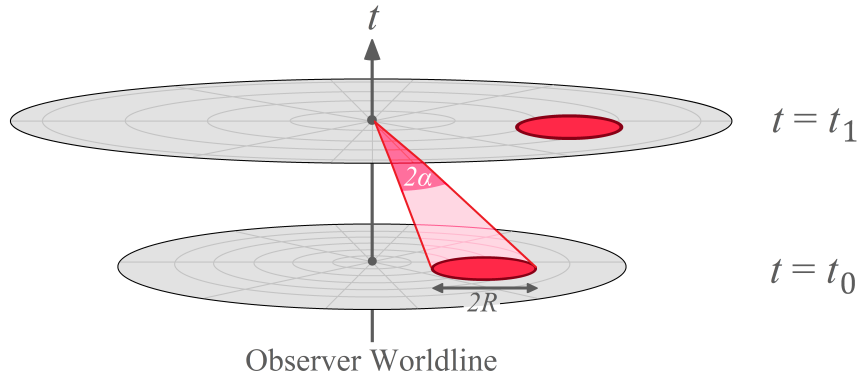


Figure 26: An observer located at  $t = t_1$  in an expanding universe measures angular sizes of cosmological objects (in red) as they appeared in the past ( $t_0 < t_1$ ) since the speed of light is finite. Although the diameter  $2R$  of the red object cannot be measured through direct observation, this can be inferred from other factors such as its mass or gravitational effects.

### 6.3 The Kottler spacetime

As a first example of a cosmological BH, we shall consider a Schwarzschild BH embedded in an expanding universe with a positive cosmological constant,  $\Lambda$ . While this spacetime is named after Friedrich Kottler, who first proposed it in 1918, it is also known throughout

literature as the Schwarzschild-de Sitter solution since it precisely describes a Schwarzschild BH in an asymptotically de Sitter universe.

Although this spacetime is not asymptotically FLRW, it can still provide valuable insight into the effects of  $\Lambda$  on the shadow of a BH. In part, this deviation from the background FLRW expansion comes from the fact that this spacetime neglects all contributions to the expansion due to matter and radiation. In reality, such a spacetime is only applicable to the very late universe, when the expansion is almost entirely dark energy-dominated. This is definitely not the case for present times [48]. Regardless, the dependence on  $\Lambda$  is of paramount importance to our general discussion on cosmological BHs.

By solving the EFEs with a non-zero cosmological constant under vacuum conditions:

$$G_{\mu\nu} + \Lambda g_{\mu\nu} = 0,$$

we obtain the unique [13] metric tensor in spherical  $(t, r, \theta, \phi)$  coordinates as [47]:

$$g_{\mu\nu} = -\left(1 - \frac{2m}{r} - \frac{\Lambda}{3}r^2\right)dt^2 + \left(1 - \frac{2m}{r} - \frac{\Lambda}{3}r^2\right)^{-1}dr^2 + r^2d\Omega^2 \quad (108)$$

Upon closer inspection, we notice that the metric takes the familiar form:  $ds^2 = g_{tt}(r, t)dt^2 + g_{rr}^{-1}(r, t)dr^2 + g_\Omega(r, t)d\Omega^2$ , which was encountered in the earlier section on static and spherically symmetric BHs. This already allows us to infer several properties of the spacetime and use plenty of readily-derived results.

### 6.3.1 Structure and important surfaces

Before analysing the properties of the BH itself, it is useful to study the general structure of the spacetime they are embedded in. Although the spacetime admits both positive and negative values for the cosmological constant  $\Lambda$ , a universe with  $\Lambda < 0$  – also known as an anti-de Sitter universe, is not of particular relevance to us since it is not descriptive of our physical reality. Such a universe will possess a negative Kretschmann scalar, which is not

compatible with current observations on the large-scale dynamics of the universe. In contrast, a positive cosmological constant corresponds to an accelerating expansion driven by the energy density of vacuum, which more closely resembles our universe at this point. For this reason, we shall impose  $\Lambda$  to be strictly positive, formally describing a de Sitter universe.

The de Sitter universe is known to be a maximally symmetric spacetime possessing 10 Killing vectors in total. In other words, this spacetime contains the largest possible amount of symmetries. Such a spacetime must necessarily have a constant normalised Ricci curvature  $\kappa_{\text{Ricci}}$ , as defined in equation 2. For 4d de Sitter spacetime, its value is quoted as [15, 57]:

$$\kappa_{\text{Ricci}} = \frac{4\Lambda}{(4)(4-1)} = \frac{\Lambda}{3}. \quad (109)$$

Kottler BHs feature a rather interesting profile due to the presence of the cosmological constant, particularly in the structure of their event horizons, which are located at the radial positions where the metric component  $g_{rr}$  vanishes. Deriving the analytical positions of these null hypersurfaces requires solving for the roots of the cubic polynomial obtained from:

$$\begin{aligned} 0 &\equiv g_{rr} = 1 - \frac{2m}{r} - \frac{\Lambda}{3}r^2 \\ \implies 0 &= -\frac{\Lambda}{3}r^3 + r - 2m. \end{aligned}$$

This polynomial exhibits distinct behaviour depending on the coefficient of  $r^3$ , namely  $-\frac{\Lambda}{3}$ , as discussed in [58]. Although  $\Lambda$  can take any value from  $\mathbb{R}$ , the polynomial will admit three real and distinct roots only when it is constrained to the interval  $0 < \Lambda < \frac{1}{9m^2}$ . This condition presents the only physically relevant scenario. In fact, by using the cubic formula, the three roots are given by [48, 58]:

$$r_{\text{eh},\pm} := r = \frac{2}{\sqrt{\Lambda}} \cos \left[ \frac{1}{3} \arccos(3m\sqrt{\Lambda}) \mp \frac{\pi}{3} \right], \text{ and } r_0 := r = -\frac{2}{\sqrt{\Lambda}} \cos \left[ \frac{1}{3} \arccos(3m\sqrt{\Lambda}) \right] \quad (110)$$

Here, it is observed that the roots are ordered according to:  $r_0 < 0 < r_{\text{eh},-} < r_{\text{eh},+}$ , which shows that  $r_0$  has no physical meaning since the curvature singularity at  $r = 0$  prohibits an extension of our coordinate system to negative distances. In particular, the fact that  $r = 0$  represents a point of infinite curvature can be deduced from the Kretschmann scalar of this spacetime [32]:

$$\kappa_{\text{Kretsch}} = \frac{48m^2}{r^6} + \frac{8\Lambda^2}{3} \quad (111)$$

From here, it is not only easy to deduce that  $\kappa_{\text{Kretsch}} \xrightarrow[r \rightarrow 0]{} \infty$ , but that the asymptotic curvature of the spacetime as  $r \rightarrow \infty$  reduces to the constant curvature of de Sitter space in four dimensions,  $\kappa_{\text{Kretsch}} \xrightarrow[r \rightarrow \infty]{} \frac{8\Lambda^2}{3}$  [32].

Before moving on to discuss the photon sphere, it is worth mentioning the properties of the two event horizons,  $r_{\text{eh},\pm}$ . Particularly, we may note that the Killing vector  $\partial_t$  is timelike only in the region  $0 < r_{\text{eh},-} < r < r_{\text{eh},+} < \infty$ , which is unlike any of the previously discussed BHs [48]. Recall that previously, the outer event horizon provided a lower bound for the radial distance at which  $\partial_t$  is timelike, while in this case, this represents an upper bound. Hence, our spacetime is characterised by:

- ✿  $0 < r < r_{\text{eh},-}$ : Since  $\partial_t$  is spacelike, this region is located inside the BH. An observer in this region is causally disconnected from the outside of the event horizon.
- ✿  $r = r_{\text{eh},-}$ : This null hypersurface represents the surface of our Kottler BH.
- ✿  $r_{\text{eh},-} < r < r_{\text{eh},+}$ : Since  $\partial_t$  is timelike only in this region, then static observers can only exist and communicate in this interval. This is the region of outer communication for the Kottler spacetime.
- ✿  $r_{\text{eh},+} = r$ : Represents the cosmological horizon. Beyond this surface, the expansion of the universe is great enough to bar communication with observers in the region of outer communication.

- ⌘  $r_{\text{eh},+} < r$ : In this region,  $\partial_t$  is spacelike, so static observers can not exist. Every observer is forced to move with the expansion of the universe. Hence, a BH with a curvature singularity at  $r = 0$  can not be seen on an observer's sky.

The Kottler BH shadow will be derived for both static and comoving observers within the region of outer communication  $r_{\text{eh},-} < r < r_{\text{eh},+}$  [47]. By first deriving the shadow for static observers, we can then generalise the result suitably to the more important class of comoving observers.

Another important surface in this spacetime is the unstable outer photon sphere. Deriving its radius is a rather simple task if we make use of expression 20, which was derived earlier on. This leads to a photon sphere located at the radius:

$$\begin{aligned}
 \frac{dh(r)^2}{dr} \Big|_{r=r_{\text{ps}}} &= 0 \\
 \frac{d}{dr} \left[ \frac{r^2}{1 - 2m/r - \Lambda r^2/3} \right] \Big|_{r=r_{\text{ps}}} &= 0 \\
 \frac{2r_{\text{ps}}(1 - 2m/r_{\text{ps}} - \Lambda r_{\text{ps}}^2/3) - r_{\text{ps}}^2(2m/r_{\text{ps}}^2 - 2\Lambda r_{\text{ps}}/3)}{(1 - 2m/r_{\text{ps}} - \Lambda r_{\text{ps}}^2/3)^2} &= 0 \\
 \implies 2r_{\text{ps}}(1 - 2m/r_{\text{ps}} - \Lambda r_{\text{ps}}^2/3) - r_{\text{ps}}^2(2m/r_{\text{ps}}^2 - 2\Lambda r_{\text{ps}}/3) &= 0 \\
 \therefore r_{\text{ps}} &= 0, 3m \tag{112}
 \end{aligned}$$

Despite the presence of a photon sphere which coincides with the geometric singularity at  $r = 0$ , this result will be suppressed since only the photon sphere located in the region of outer communication will be visible to the observer.

Another striking result is that the photon sphere of the Kottler BH ( $\Lambda \neq 0$ ) is located at the same radial coordinate ( $r_{\text{ps}} = 3m$ ) as in the Schwarzschild case ( $\Lambda = 0$ ). Although this might appear counterintuitive, it is actually not a coincidence that the cosmological term cancelled in the derivation of expression 112. This result is attributed to the fact that these two spacetimes have identical,  $\Lambda$ -independent geodesics. A more detailed discussion on this matter can be found in [30], whose author was the first to identify this property in 1983.

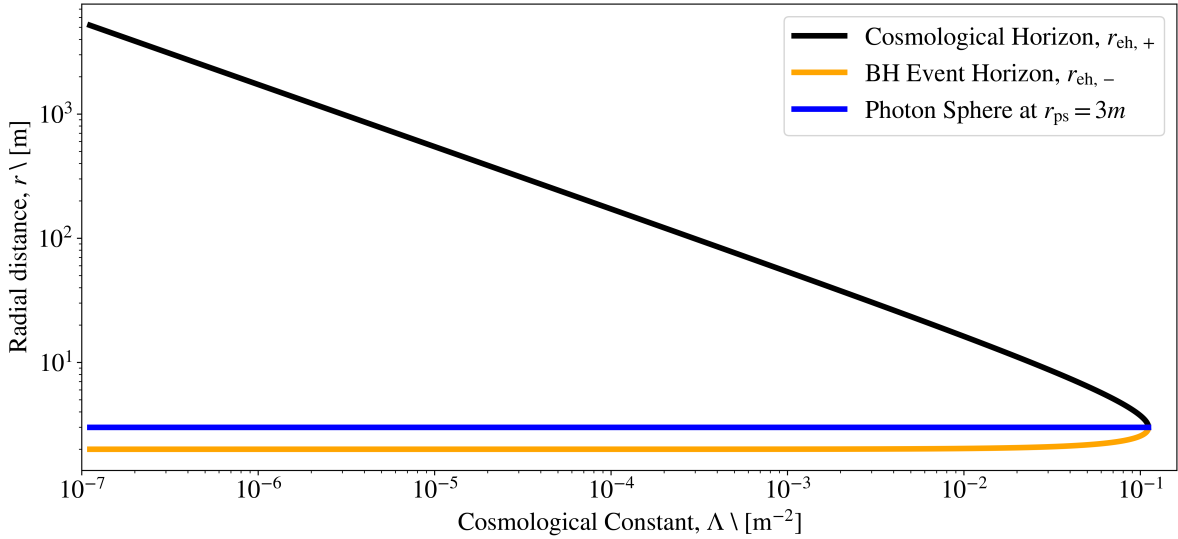


Figure 27: The locations of the event horizons and photon sphere for a Kottler BH of mass  $m = 1$ , as a function of  $\Lambda$ . A logarithmic scale was used to visualise the asymptotic nature of  $r_{\text{eh},+}$ , which diverges as  $\Lambda \rightarrow 0$ . Moreover, the inner event horizon coincides with the Schwarzschild one (at  $2m$ ) as  $\Lambda \rightarrow 0$ . Expectedly, the photon sphere has a constant radial distance for any  $\Lambda$ . The three surfaces coincide in the extremal case when  $\Lambda = \frac{1}{9m^2}$ . The program used to plot this figure can be found in appendix B.10.

### 6.3.2 BH shadow in Kottler spacetime for static observers

The fact that the metric is  $t$ -independent, in addition to having a timelike component satisfying the hypersurface orthogonality condition in equation 9, implies that the metric is locally static in the region of outer communication [58].

Proceeding with the same method used to treat the other static BHs, we will make explicit use of the photon sphere at  $r_{\text{ps}} = 3m$  to derive the angular size of the Kottler BH shadow assuming a static observer (see diagram 28). By inputting this value into equation

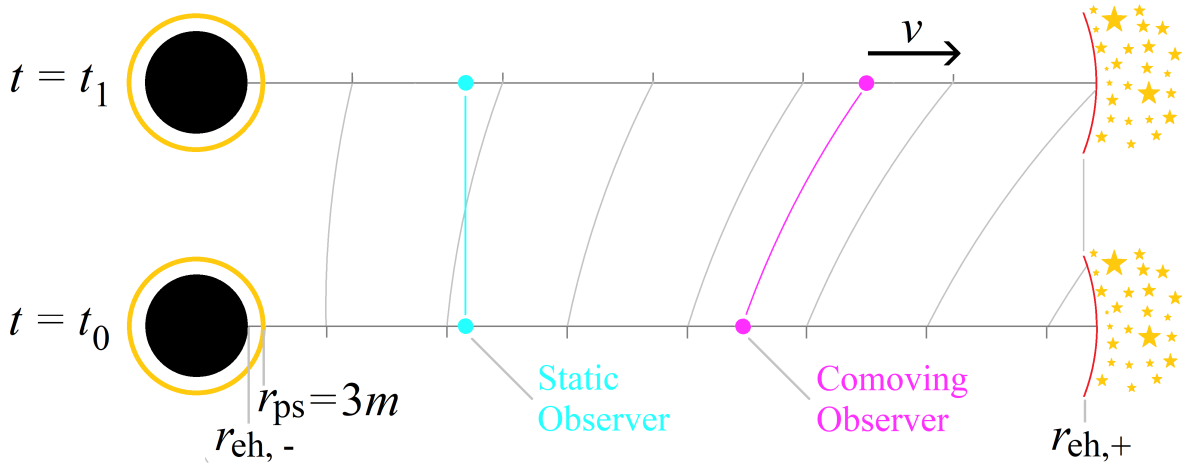


Figure 28: A diagram showing the expansion of the universe using two snapshots at  $t = t_0, t_1$ . A static observer will not change their position with respect to their initial one, while a comoving observer will allow themselves to be dragged with the expansion. A comoving observer will have an associated 4-velocity away from the BH, which induces redshift effects.

21, we find the critical impact parameter to be [47, 48]:

$$\begin{aligned} b_{\text{cr}} &= \frac{3m}{\sqrt{1 - 2m/r_{\text{ps}} - \Lambda r_{\text{ps}}^2/3}} \\ &= \frac{3m}{\sqrt{1 - 2m/3m - \Lambda(9m^2)/3}} \\ \implies b_{\text{cr}} &= \frac{3\sqrt{3}m}{\sqrt{1 - 9\Lambda m^2}}, \end{aligned}$$

which only exists if the cosmological constant is in the interval  $0 < \Lambda < \frac{1}{9m^2}$ , as we have already imposed. The BH will not be visible for  $\Lambda \geq \frac{1}{9m^2}$ . Furthermore, we cannot make any approximations which are valid for distant observers since the metric is not asymptotically flat, this is specifically in reference to the use of equation 24. Although the Schwarzschild metric reduces to flat spacetime with  $-g_{tt}, g_{rr} \xrightarrow[r \rightarrow \infty]{} 1$ , we observe that for the Kottler metric, neither

$$-g_{tt}(r) = 1 - 2m/r - \Lambda r^2/3 \xrightarrow[r \rightarrow \infty]{} \infty$$

nor,

$$g_{rr}(r) = \frac{1}{1 - 2m/r - \Lambda r^2/3} \xrightarrow[r \rightarrow \infty]{} 0,$$

satisfy the conditions for being asymptotically flat. This means that we have to settle for the use of equation 23 to derive the shadow's angular size,  $\alpha_{\text{sh, stat}}$ , as measured by a static observer. The expression for angular size can then be derived as [47]:

$$\begin{aligned} \sin \alpha_{\text{sh, stat}} &= \frac{b_{\text{cr}}}{h(r_O)} = \sqrt{-\frac{g_{tt}(r_O)}{g_\Omega(r_O)}} \frac{3\sqrt{3}m}{\sqrt{1-9\Lambda m^2}} \\ &= \sqrt{\frac{1-2m/r_O - \Lambda r_O^2/3}{r_O^2}} \frac{3\sqrt{3}m}{\sqrt{1-9\Lambda m^2}} \\ \implies \alpha_{\text{sh, stat}} &= \arcsin \left[ \frac{3\sqrt{3}m}{r_O} \sqrt{\frac{1-2m/r_O - \Lambda r_O^2/3}{1-9\Lambda m^2}} \right]. \end{aligned} \quad (113)$$

By setting  $\Lambda = 0$  and assuming a static observer with  $r_O \gg 1$ , we recover the distant observer approximation for the angular size of a Schwarzschild BH, identical to equation 27.

The first subplot in figure 29 showcases the angular size of a Kottler BH with mass of  $m = 1$ , as seen by a static observer. This figure is presented in the upcoming section because a comparison with comoving observers must be made – especially in the context of cosmological BHs. In the subplot, the angular size is plotted as a function of observer distance, for a variety of fixed cosmological constants. Although the most up-to-date measurements of the cosmological constant estimate its value to be on the order of  $\Lambda_{\text{modern}} \sim 10^{-122}$  (in natural units where the Planck's constant was set to  $\hbar = 1$ ) [9], this value was too insignificant to perform computations with. However, even for a cosmological constant of  $\Lambda \sim 10^{-7}$  (yellow line), the expansion of the universe is so insignificant that the BH shadow is nearly identical to the Schwarzschild one (blue line). This suggests that if we were to use the actual modern-day cosmological constant  $\Lambda_{\text{modern}}$ , then the resulting angular size profile would effectively match that of a Schwarzschild BH's shadow. Finally, the radial distance at which the static observer's shadow becomes  $\alpha_{\text{sh, stat}} = 0$  corresponds to the cosmological horizon. For larger values of  $\Lambda$ , the universe expands at a faster rate, which imposes stricter constraints on how far away a static observer can remain before being overcome by cosmic expansion.

### 6.3.3 BH shadow in Kottler spacetime for comoving observers

In the previous subsection, we derived the angular size of a Kottler BH for an observer whose position is time-independent. Hence, the effects of an expanding universe on the BH shadow were not fully explored. This section extends the discussion on the Kottler BH shadow to observers who are comoving along with the expansion of the universe (see diagram 28).

We start by transforming our spherical coordinates  $\{t, r, \theta, \phi\}$  into the more suitable McVittie coordinate system  $\{\tilde{t}, \tilde{r}, \tilde{\theta} = \theta, \tilde{\phi} = \phi\}$ , where [48]:

$$r = \tilde{r} e^{H_0 \tilde{t}} \left(1 + \frac{m}{2\tilde{r}} e^{-H_0 \tilde{t}}\right)^2, \quad t = \tilde{t} + \int_{w_0}^{\tilde{r} e^{H_0 \tilde{t}}} \frac{H_0 \left(1 + \frac{m}{2w}\right)^6 w dw}{\left(1 - \frac{m}{2w}\right)^2 - H_0^2 w^2 \left(1 + \frac{m}{2w}\right)^6}, \quad (114)$$

with  $w_0$  an integration factor, and the Hubble constant:

$$H_0 = \sqrt{\frac{\Lambda}{3}} \quad (115)$$

The McVittie coordinates have associated basis vector fields  $\{\partial_{\tilde{t}}, \partial_{\tilde{r}}, \partial_{\theta}, \partial_{\phi}\}$  which are different from the ones given by the spherical coordinate system. To obtain these new basis vectors, we can use the transformation rule to conclude that  $\partial_{\theta}$  and  $\partial_{\phi}$  remain unchanged, while:

$$\partial_{\tilde{t}} = \frac{1 - \frac{2m}{r}}{1 - \frac{2m}{r} - H_0^2 r^2} \partial_t + H_0 r \sqrt{1 - \frac{2m}{r}} \partial_r, \quad (116)$$

and,

$$\tilde{r} \partial_{\tilde{r}} = \frac{H_0 r^2}{1 - \frac{2m}{r} - H_0^2 r^2} \partial_t + r \sqrt{1 - \frac{2m}{r}} \partial_r, \quad (117)$$

which will prove useful in due time.

By inverting the relationships in equation 114, we allow ourselves to express the Kottler metric in the special time-dependent form, which resembles the FLRW metric closely. This is given by [48, 58]:

$$ds^2 = - \left(\frac{1 - \mu}{1 + \mu}\right)^2 d\tilde{t}^2 + e^{2H_0 \tilde{t}} (1 + \mu)^4 (d\tilde{r}^2 + \tilde{r}^2 d\Omega^2), \quad (118)$$

where we have substituted:

$$\mu := \frac{m}{2\tilde{r}a(\tilde{t})} \quad \text{and} \quad a(\tilde{t}) = e^{H_0\tilde{t}}. \quad (119)$$

The motivation for choosing to perform this change of coordinates comes from the fact that observers travelling along timelike  $\tilde{r} = \text{constant}$  paths will now be comoving with the exponentially expanding universe. The rate of this expansion is suitably quantified by the constant parameter  $H_0$  [20].

Furthermore, for such comoving observers, the angular size of their BH shadow,  $\alpha_{\text{sh, comov}}$ , can be related to the static one through the use of the standard aberration formula borrowed from special relativity, under the assumption that spacetime is locally flat at the position of the observer. This result is quoted without derivation from [20, 35, 48] as:

$$\cos \alpha_{\text{sh, comov}} = \frac{\cos \alpha_{\text{sh, stat}} - v}{1 - v \cos \alpha_{\text{sh, stat}}}, \quad (120)$$

where  $v$  is the relative spatial 3-velocity of the comoving observer with respect to the static one (see figure 28). This is bounded above by the speed of light, which was set to 1 throughout. Although this result can be readily used in its current form, we prefer to express it purely in terms of sine functions. By squaring both sides of 120 :

$$\begin{aligned} \frac{(\cos \alpha_{\text{sh, stat}} - v)^2}{(1 - v \cos \alpha_{\text{sh, stat}})^2} &= \cos^2 \alpha_{\text{sh, comov}} \equiv 1 - \sin^2 \alpha_{\text{sh, comov}} \\ \frac{(1 - v \cos \alpha_{\text{sh, stat}})^2 - (\cos \alpha_{\text{sh, stat}} - v)^2}{(1 - v \cos \alpha_{\text{sh, stat}})^2} &= \sin^2 \alpha_{\text{sh, comov}} \end{aligned}$$

Hence, we obtain the more applicable result encountered in [35] as:

$$\sin^2 \alpha_{\text{sh, comov}} = (1 - v^2) \cdot \frac{\sin^2 \alpha_{\text{sh, stat}}}{\left(1 - v \sqrt{1 - \sin^2 \alpha_{\text{sh, stat}}}\right)^2}, \quad (121)$$

which is valid in the region beyond the photon sphere,  $3m < r_O$ , and most accurate is the region where the spacetime is approximately flat. Furthermore, given that the observer is not necessarily static, then they can be located beyond the cosmological horizon without loss of generality. This leaves us with the much broader interval for shadow observation:

$3m < r_0 < \infty$ .

To derive an explicit expression for the 3-velocity  $v$ , we must use the 4-velocity vectors for the static and comoving observers,  $V_{\text{stat}}^\mu \partial_\mu = V_{\text{stat}}^t \partial_t + V_{\text{stat}}^r \partial_r + V_{\text{stat}}^\theta \partial_\theta + V_{\text{stat}}^\phi \partial_\phi$  and  $V_{\text{comov}}^\mu \partial_\mu = V_{\text{comov}}^t \partial_t + V_{\text{comov}}^r \partial_r + V_{\text{comov}}^\theta \partial_\theta + V_{\text{comov}}^\phi \partial_\phi$ , respectively. These both satisfy the universal normalisation conditions common to all 4-velocities:

$$g_{\mu\nu} V_{\text{stat}}^\mu V_{\text{stat}}^\nu = -1, \quad \text{and} \quad g_{\mu\nu} V_{\text{comov}}^\mu V_{\text{comov}}^\nu = -1,$$

where  $g_{\mu\nu}$  denotes the Kottler metric in static coordinates. We can conclude that since a static observer experiences no spatial movement ( $r = \text{constant}$ ), then their 4-velocity will be proportional to  $\partial_t$  only. Dually, since the comoving observer is at rest in the second metric ( $\tilde{r}_0 = \text{constant}$ ), despite appearing in motion with respect to the first, then his 4-velocity is proportional to  $\partial_{\tilde{t}}$ . More specifically, there exists two time-independent coefficients:  $q, \tilde{q} \in \mathbb{R}$  such that [48]:

$$V_{\text{stat}}^\mu \partial_\mu = q \partial_t + 0 \partial_r + 0 \partial_\theta + 0 \partial_\phi, \quad (122)$$

and,

$$\begin{aligned} V_{\text{comov}}^\mu \partial_\mu &= \tilde{q} \partial_{\tilde{t}} + 0 \partial_{\tilde{r}} + 0 \partial_\theta + 0 \partial_\phi \\ &= \tilde{q} \left[ \frac{1 - \frac{2m}{r}}{1 - \frac{2m}{r} - H_0^2 r^2} \partial_t + H_0 r \sqrt{1 - \frac{2m}{r}} \partial_r \right] + 0 \partial_{\tilde{r}} + 0 \partial_\theta + 0 \partial_\phi, \text{ using equation 116} \\ \implies V_{\text{comov}}^\mu \partial_\mu &= \frac{1 - \frac{2m}{r}}{1 - \frac{2m}{r} - H_0^2 r^2} \tilde{q} \partial_t + H_0 r \tilde{q} \sqrt{1 - \frac{2m}{r}} \partial_r + 0 \partial_\theta + 0 \partial_\phi, \end{aligned} \quad (123)$$

in static coordinates. This allows us to swiftly substitute these relationships back into the normalisation conditions above and directly determine the constants appropriately. Starting with  $q$ :

$$\begin{aligned} -1 &= g_{\mu\nu} V_{\text{stat}}^\mu V_{\text{stat}}^\nu = g_{tt} V_{\text{stat}}^t V_{\text{stat}}^t = \left( 1 - \frac{2m}{r} - H_0^2 r^2 \right) q^2 \\ \implies q &= \frac{1}{\sqrt{1 - \frac{2m}{r} - H_0^2 r^2}}. \end{aligned} \quad (124)$$

Similarly, for the value of  $\tilde{q}$ :

$$\begin{aligned}
 -1 &= g_{\mu\nu} V_{\text{comov}}^\mu V_{\text{comov}}^\nu = g_{tt} V_{\text{comov}}^t V_{\text{comov}}^t + g_{rr} V_{\text{comov}}^r V_{\text{comov}}^r \\
 &= -\left(1 - \frac{2m}{r} - H_0^2 r^2\right) \tilde{q}^2 \left(\frac{1 - \frac{2m}{r}}{1 - \frac{2m}{r} - H_0^2 r^2}\right)^2 + \left(1 - \frac{2m}{r} - H_0^2 r^2\right)^{-1} \tilde{q}^2 \left(H_0 r \sqrt{1 - \frac{2m}{r}}\right)^2 \\
 &= \tilde{q}^2 \left(\frac{1 - \frac{2m}{r}}{1 - \frac{2m}{r} - H_0^2 r^2}\right) \left[-\left(1 - \frac{2m}{r}\right) + H_0 r\right] \\
 \implies -1 &= \tilde{q}^2 \left(\frac{2m}{r} - 1\right) \quad \therefore \tilde{q} = \frac{1}{\sqrt{1 - \frac{2m}{r}}} \tag{125}
 \end{aligned}$$

When substituted back into equations 122 and 123, we obtain the explicit 4-velocities of the observers in static coordinates as [48]:

$$V_{\text{stat}}^\mu \partial_\mu = \frac{1}{\sqrt{1 - \frac{2m}{r} - H_0^2 r^2}} \partial_t + 0 \partial_r + 0 \partial_\theta + 0 \partial_\phi, \tag{126}$$

and,

$$\begin{aligned}
 V_{\text{comov}}^\mu \partial_\mu &= \frac{1}{\sqrt{1 - \frac{2m}{r}}} \partial_{\tilde{t}} \\
 \implies V_{\text{comov}}^\mu \partial_\mu &= \frac{\sqrt{1 - \frac{2m}{r}}}{1 - \frac{2m}{r} - H_0^2 r^2} \partial_t + H_0 r \partial_r + 0 \partial_\theta + 0 \partial_\phi, \tag{127}
 \end{aligned}$$

where we have conveniently used equation 116 to convert  $\partial_{\tilde{t}}$ , into the directional derivatives in our initial spherical coordinates. Knowing the values of  $V_{\text{stat}}^\mu \partial_\mu$  and  $V_{\text{comov}}^\mu \partial_\mu$  allows us to relate them to our quantity of interest,  $v$ .

To relate any two 4-velocities  $U^\mu = (1, u) = (1, u^0, u^1, u^3)$  and  $W^\mu = (1, w) = (1, w^0, w^1, w^3)$  together, we make use of the special relativistic result [38, 48]:

$$g_{\mu\nu} U^\mu W^\nu = \frac{u \cdot w - 1}{\sqrt{1 - u^2} \sqrt{1 - w^2}}, \tag{128}$$

which, when adapted to our case, will reduce to:

$$g_{\mu\nu} V_{\text{stat}}^\mu V_{\text{comov}}^\nu = -\frac{1}{\sqrt{1 - v^2}}, \tag{129}$$

since  $V_{\text{stat}}^\mu = (1, 0, 0, 0)$ , i.e. the 3-velocity of the static observer is zero by definition. Moreover, we have  $V_{\text{comov}}^\mu = (1, v) = (1, v^0, v^1, v^2)$ , with the 3-velocity of the comoving observer equivalent to the relative spatial velocity between the two observers. Since we have obtained the general expressions for  $V_{\text{stat}}^\mu$  and  $V_{\text{comov}}^\nu$ , we can evaluate the left-hand side of the equation and finally determine  $v$ . This procedure yields:

$$\begin{aligned} -\frac{1}{\sqrt{1-v^2}} &= g_{tt} V_{\text{stat}}^t V_{\text{comov}}^t = \left[ 1 - \frac{2m}{r} - H_0^2 r^2 \right] \left[ \frac{1}{\sqrt{1 - \frac{2m}{r} - H_0^2 r^2}} \right] \left[ \frac{\sqrt{1 - \frac{2m}{r}}}{1 - \frac{2m}{r} - H_0^2 r^2} \right] \\ \implies 1 - v^2 &= \frac{1 - \frac{2m}{r} - H_0^2 r^2}{1 - \frac{2m}{r}}, \text{ squaring and inverting both sides} \\ \therefore v(r) &= \frac{H_0 r}{\sqrt{1 - \frac{2m}{r}}} \end{aligned} \quad (130)$$

This allows us to finally express equation 121 into explicit form by using the above result for  $v$ , as well as equation 113 for  $\sin \alpha_{\text{sh, comov}}$ :

$$\alpha_{\text{sh, comov}} = \arcsin \left[ \frac{3\sqrt{3}m}{r_O} \sqrt{1 - \frac{2m}{r_O}} \sqrt{1 - 27H_0^2 m^2} + 3\sqrt{3}m H_0 \sqrt{1 - \frac{27m^2}{r_O^2} \left( 1 - \frac{2m}{r_O} \right)} \right] \quad (131)$$

The second subplot in figure 29 shows the Kottler BH shadow's dependence on  $\Lambda$  and the instantaneous observer distance  $r_O$ , for a comoving observer. Surprisingly, the BH shadow actually grows for larger cosmological constants, rather than shrinking. This is best explained by the fact that relativistic aberration acts to magnify angular sizes of objects in other reference frames (see equation 121). This means that the shadow is not impeded by the cosmological horizon, and can be seen for all  $3m < r_O < \infty$ . A more in-depth discussion on this phenomenon is found in [8].

#### 6.3.4 Asymptotic limit of Kottler BH shadow

Although figure 29 already presents several visual differences in the shadow's size as seen by static and comoving observers, several other phenomena can be derived analytically. In particular, the section serves to showcase the interesting difference in shadow size for observers

at large distances  $r_O \rightarrow \infty$ .

In general, special attention can be drawn to the shadow size at large observer distances with  $r_O, \tilde{r}_O \gg 3m$ . For a static observer bound by a cosmological horizon at  $r_{\text{eh},+}$ , we must have  $r_{\text{eh},+} > r_O \gg m$ , which is satisfied when the cosmological constant satisfies  $\Lambda m^2 \ll 1$ . These conditions allow us to approximate equation 113 to first order in  $\mathcal{O}(\frac{m}{r})$  and  $\mathcal{O}(\Lambda m^2)$  as [48]:

$$\alpha_{\text{sh, stat}} \simeq \frac{3\sqrt{3}m}{r_O} \sqrt{1 - H_0^2 r_O^2}, \quad \text{for } r_{\text{eh},+} > r_O \gg m. \quad (132)$$

With the same reasoning applied to comoving observers, equation 131 can be approximated by [48]:

$$\alpha_{\text{sh, comov}} \simeq \frac{3\sqrt{3}m}{r_O} \left( \sqrt{1 - 27H_0^2 m^2} + H_0 r_O \right), \quad \text{for } r_O \gg m. \quad (133)$$

The key difference arises when considering the limiting behaviour as  $r_O$  approaches the upper bound in each case:

$$\alpha_{\text{sh, stat}} \xrightarrow[r_O \rightarrow r_{\text{eh},+}]{} 0, \quad \text{and} \quad \alpha_{\text{sh, comov}} \xrightarrow[r_O \rightarrow \infty]{} 3\sqrt{3}mH_0 \dots \text{a finite size!} \quad (134)$$

This surprisingly implies that in an asymptotically de Sitter universe, a comoving observer will be able to observe the BH from every point in the universe, while for a static observer, the shadow vanishes from their sky at infinity. Actually, the shadow of a Kottler BH as seen by a static observer vanishes for finite values of  $r_O$ . Indeed, since  $r_{\text{eh},+} \gg m$  is a null hypersurface, then:

$$0 = g_{tt}(r_{\text{eh},+}) = 1 - \frac{2m}{r_{\text{eh},+}} - H_0^2 r_{\text{eh},+}^2 \simeq 1 - H_0^2 r_{\text{eh},+}^2 + \mathcal{O}\left(\frac{m}{r_{\text{eh},+}}\right)$$

So at  $r_O = r_{\text{eh},+} = \frac{1}{H_0}$ , we find that from the approximation in 132,  $\alpha_{\text{sh, stat}} \simeq 0$ .

The visibility of the shadow for a comoving observer depends mainly on the brightness of the dense background light sources. The effect of a de Sitter universe on the background brightness was not considered, but is essential for a more detailed description of the shadow. Moreover, the unphysical nature of dark energy-driven expansion necessitates the use of a more realistic spacetime. The McVittie is one such generalising metric suitable for discussion.

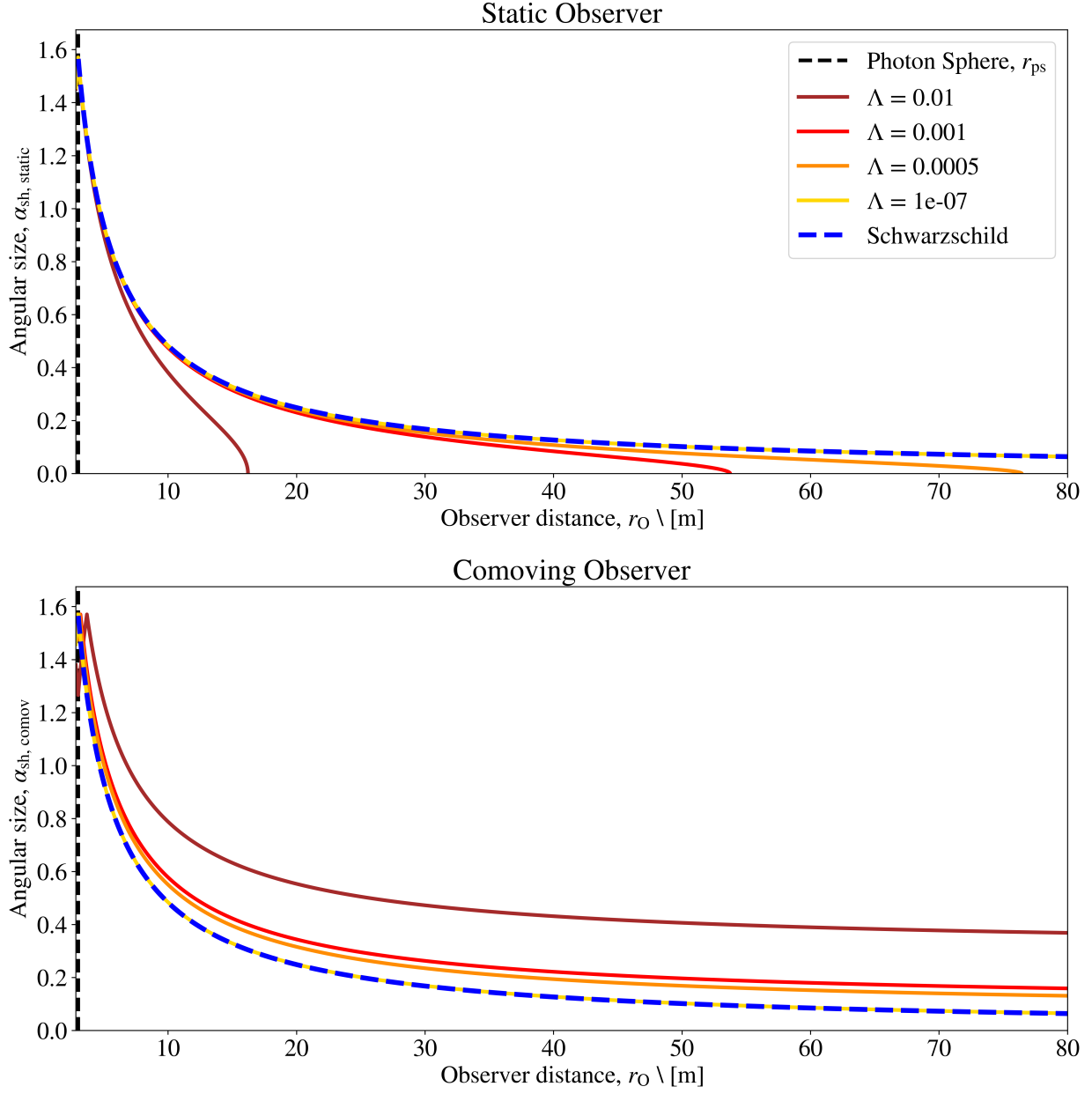


Figure 29: Plots showcasing the angular size of Kottler BH shadows against radial distance, for both static and comoving observers, using equations 113 and 131. The mass of the BH is fixed at  $m = 1$ . Each curve represents the shadow profile characterised by some fixed  $\Lambda$ . These plots generalise figure 4 from [48], and figure 7 from [20]. The program used to plot this figure can be found in appendix B.11.

## 6.4 The McVittie spacetime

This is the last specific example of a cosmological BH which will be tackled. The McVittie metric is an exact solution to the EFEs describing a Schwarzschild BH embedded in a spatially flat ( $k = 0$ ) FLRW background universe. While it shares similarities with the Kottler metric for comoving observers, it significantly generalises the spacetime to include other drivers of expansion. The metric in isotropic comoving coordinates  $(t, r, \theta, \phi)$  is given by [23, 53, 65]:

$$ds^2 = - \left( \frac{1 - \mu(t, r)}{1 + \mu(t, r)} \right)^2 dt^2 + a(t)^2 (1 + \mu(t, r))^4 (dr^2 + r^2 d\Omega^2), \quad (135)$$

where  $\mu(t, r) = \frac{m}{2a(t)r}$  just as before. This metric is distinguished from the Kottler solution given that  $a(t)$  is generally obtained by solving FE1 and FE2 (see definition 6.2) using a general expression for the Hubble parameter  $H(z)$ . To ensure that  $a(t)$  can be obtained analytically, simplifying assumptions about the contents of the universe must be made – such as assuming a matter-dominated, or dark energy-dominated universe. Furthermore, to simplify our analysis, we shall assume that there is no net radial outflow of energy from the central Schwarzschild BH – this is known as the no-accretion condition,  $G_t^r = 0 = T_t^r$  [23].

We can see that when  $H(t) = H_0$  ( $=$  constant), we recover the Kottler metric, which corresponds to a dark energy-dominated universe. Furthermore, if  $m = 0$ , we recover the FLRW background metric, while if  $a(t) = \text{constant}$ , we obtain the Schwarzschild metric. At first glance, this metric seems to fit our requirements for a cosmological BH spacetime perfectly. However, this is not the case.

### 6.4.1 Structure and Flaws

The event horizon of this metric occurs when  $g_{tt}$  vanishes. This condition yields:

$$\begin{aligned} 0 \equiv g_{tt} &= \left( \frac{1 - \mu(t, r)}{1 + \mu(t, r)} \right)^2 \implies \mu(t, r) = 1 \\ \therefore r_{\text{eh}} &:= r = \frac{m}{2a(t)} \end{aligned}$$

Unlike previous examples, the McVittie spacetime exhibits an irremovable curvature singularity at the event horizon. This is demonstrated by the diverging curvature invariants [23, 53]:

$$p = -\frac{1}{8\pi} \left[ 3H(t)^2 + 2\dot{H}(t) \frac{1+\mu}{1-\mu} \right], \quad (136)$$

$$R = 12H(t)^2 + 6\dot{H}(t) \frac{1+\mu}{1-\mu} \quad (137)$$

and,

$$\begin{aligned} \kappa_{\text{Kretsch}} = & \frac{12}{a(t)^4(m-2ra(t))^2(m+2ra(t))^{12}} \left[ 5m^{14}\dot{a}(t)^4 + 114688mr^{13}a(t)^{15}\ddot{a}(t)^2 \right. \\ & + 16384r^{14}a(t)^{16}\ddot{a}(t)^2 - 4m^{13}a(t)\dot{a}(t)^2(-29r\dot{a}(t)^2 + m\ddot{a}(t)) \\ & + m^{12}a(t)^2(1228r^2\dot{a}(t)^4 - 104mr\dot{a}(t)^2\ddot{a}(t) + m^2\ddot{a}(t)^2) \\ & + 4m^{11}ra(t)^3(1960r^2\dot{a}(t)^4 - 312mr\dot{a}(t)^2\ddot{a}(t) + 7m^2\ddot{a}(t)^2) \\ & + 11264m^5r^7a(t)^9(41r^2\dot{a}(t)^4 - 117mr\dot{a}(t)^2\ddot{a}(t) + 39m^2\ddot{a}(t)^2) \\ & + 4m^{10}r^2a(t)^4(8404r^2\dot{a}(t)^4 - 2288mr\dot{a}(t)^2\ddot{a}(t) + 91m^2\ddot{a}(t)^2) \\ & + 32m^9r^3a(t)^5(3190r^2\dot{a}(t)^4 - 1430mr\dot{a}(t)^2\ddot{a}(t) + 91m^2\ddot{a}(t)^2) \\ & + 176m^8r^4a(t)^6(1284r^2\dot{a}(t)^4 - 936mr\dot{a}(t)^2\ddot{a}(t) + 91m^2\ddot{a}(t)^2) \\ & + 704m^7r^5a(t)^7(528r^2\dot{a}(t)^4 - 624mr\dot{a}(t)^2\ddot{a}(t) + 91m^2\ddot{a}(t)^2) \\ & + 2112m^6r^6a(t)^8(220r^2\dot{a}(t)^4 - 416mr\dot{a}(t)^2\ddot{a}(t) + 91m^2\ddot{a}(t)^2) \\ & + 8192mr^{11}a(t)^{13}(10r^2\dot{a}(t)^4 - 26mr\dot{a}(t)^2\ddot{a}(t) + 91m^2\ddot{a}(t)^2) \\ & + 4096r^{12}a(t)^{14}(4r^2\dot{a}(t)^4 - 8mr\dot{a}(t)^2\ddot{a}(t) + 91m^2\ddot{a}(t)^2) \\ & + 1024m^3r^7a(t)^{11}(-64 + 296r^4\dot{a}(t)^4 - 1144mr^3\dot{a}(t)^2\ddot{a}(t) + 1001m^2r^2\ddot{a}(t)^2) \\ & + 1024m^2r^8a(t)^{12}(64 + 188r^4\dot{a}(t)^4 - 624mr^3\dot{a}(t)^2\ddot{a}(t) + 1001m^2r^2\ddot{a}(t)^2) \\ & \left. + 256m^4r^6a(t)^{10}(64 + 1540r^4\dot{a}(t)^4 - 5720mr^3\dot{a}(t)^2\ddot{a}(t) + 3003m^2r^2\ddot{a}(t)^2) \right] \quad (138) \end{aligned}$$

Detailed derivations for these scalars can be found in appendix A. These can be shown to all diverge at the event horizon  $r_{\text{eh}} = \frac{m}{2a(t)}$ , which shows that the null hypersurface also satisfies the defining property of a gravitational singularity [53].

We should note from the weak cosmic censorship conjecture [45] that every gravitational singularity must be enshrouded by an event horizon. However, the general McVittie solution violates this principle since the event horizon and curvature singularity clearly coincide. This leads many to dismiss this spacetime as not being representative of a physical BH. One of the possible resolutions to this major flaw would be to impose  $\dot{H}(t) = 0$ , which will reduce the McVittie metric to the Kottler in comoving coordinates. This will once again correspond to a universe expanding solely under the influence of dark energy, which is not representative of our current universe [41, 53]. In any case, discussing the shadow in such a spacetime is nonetheless beneficial since we do not particularly concern ourselves with such causal defects.

Another method used to tackle this flaw is to introduce a new scale factor  $a(t, r)$  which is dependent on both the time and radial coordinate. In this case, we will allow the scale factor to vary with the radial coordinate, leading to local inhomogeneity near the BH. However, far from the BH, in the region of significant cosmic expansion, the effect of  $r$  should vanish such that the CP is not violated. The Tolman metric explores this type of parameter dependence of  $a(t, r)$  [53].

#### 6.4.2 BH shadow in the McVittie spacetime

Unfortunately, studying the null trajectories in this spacetime is no easy task due to the explicit time-dependence of the metric in comoving coordinates [43]. More specifically, since the metric is not static,  $\partial_t$  is not a Killing vector, meaning that we can neither associate it with a symmetry, nor with the conservation of the total energy  $E$ . This barrier removes one of the most crucial constants of motion, and leads to an insufficient amount required to integrate the Lagrangian of the spacetime. There are, however, methods to obtain the geodesics both numerically [12] and also analytically under weak-field conditions [51].

Consider an observer comoving with the expanding universe at the spacetime coordinates  $(t = t_O, r = r_O)$ . The structure of this spacetime will allow us to study the motion of light in

two distinct regimes separately. These are characterised by (i) a strong gravitational region near the BH ( $r_O \sim m$ ), and (ii) an FLRW background in the radially asymptotic region ( $r_O \gg m$ ). Moreover, in some intermediary region between these two asymptotic regimes, we can demonstrate the existence of a region characterised as being flat. Its existence is attributed to the fact that the gravitational pull due to the BH and the repulsion due to the FLRW expansion will be equal and opposite, thereby creating a locally flat spacetime [12, 65]. Hence, to derive a global expression for the angular size of the BH shadow, we can derive separate expressions valid in the respective gravitational regimes. These will naturally match on the intermediate flat spacetime.

#### 6.4.3 The (inner) Schwarzschild region

The existence of this region can be demonstrated by showing that in the low redshift regime  $z \ll 1$ , the scale factor  $a(t)$  can be approximated to be constant. This will reduce the McVittie metric to the Schwarzschild one, for which we have already conveniently derived the angular size of the BH shadow.

In the vicinity of the BH, we have a region of negligible redshift  $z \ll 1$ , which yields the approximation:

$$0 \simeq z \implies \frac{a(t_O)}{a(t)} \simeq 1, \quad \text{with } t_O \simeq t.$$

By performing a Taylor expansion of  $a(t)$  at the time of observation  $t = t_O$  (using equation 106), we show that:

$$\begin{aligned} a(t) &= a(t_O) - (t_O - t)\dot{a}(t_O) + \mathcal{O}[(t_O - t)^2] \\ &= a(t_O) [1 - (t_O - t)H(t_O) + \mathcal{O}[(t_O - t)^2]], \end{aligned} \quad (139)$$

If we further assume that  $(t_O - t)H(t_O) \ll 1$ , or more specifically that  $(t_O - t) \ll H(t_O)^{-1}$ , then we are well within our right to approximate  $a(t) \simeq a(t_O) = \text{constant}$ . In this case, the radial transformation [65]:

$$R = a(t_O)r \left(1 + \frac{2m}{a(t_O)r}\right)^2, \quad \text{with } R_O = a(t_O)r_O \left(1 + \frac{2m}{a(t_O)r_O}\right)^2, \quad (140)$$

will reduce the McVittie metric in comoving coordinates to the Schwarzschild metric found in equation 25. The coordinate  $R$  corresponds to the measure of radial distance in the Schwarzschild spacetime. For this BH model, the angular size of the shadow was already calculated in equation 27 as:

$$\alpha_{\text{inner}} = \arcsin \left[ \frac{3\sqrt{3}m}{R_O} \sqrt{1 - \frac{2m}{R_O}} \right], \text{ for } R_O > 3m. \quad (141)$$

#### 6.4.4 The (outer) FLRW region

In the asymptotic region when  $r_O \gg m$ , the high value of redshift will imply that the gravitational field strength of the BH will become negligible, and the influence of the FLRW background will become dominant.

In this case, the angular size of the shadow can be described by the angular diameter distance expression in 107:

$$\alpha_{\text{outer}} = \frac{R_{\text{sh}}}{d_A(z)}, \quad (142)$$

where  $R_{\text{sh}}$  is the effective linear radius of the cosmological BH. In its current state, this identity is not particularly useful since it relates our BH shadow size to the redshift. A more useful identity will be obtained by changing this dependence to the proper observer distance  $R_O$  instead. In particular, using equation (2.65) from [41] allows us to precisely relate the comoving observer distance,  $r_O$ , with redshift using:

$$r_O(z) = \frac{1}{a(t_O)} \int_0^z \frac{d\bar{z}}{H(\bar{z})}. \quad (143)$$

This expression can be more suitably adapted by using the definition of  $R_O$  from equation 140. Applying this to a distant observer will imply that:

$$R_O := a(t_O)r_O \left( 1 + \frac{2m}{a(t_O)r_O} \right)^2 \xrightarrow{r_O \gg m} R_O \simeq a(t_O)r_O,$$

such that by substituting  $R_O$  in equation 143, we derive the radial distance as:

$$R_O = \int_0^z \frac{d\bar{z}}{H(\bar{z})}. \quad (144)$$

Finally, this expression allows us to simplify the integral encountered in the definition of the angular diameter distance  $d_A(z)$ . After substituting  $R_O$  into this definition, we obtain the distant observer approximation:  $d_A(z) \simeq \frac{R_O}{1+z}$ , which gives us an estimate for equation 142 as [12]:

$$\alpha_{\text{outer}} = \frac{R_{\text{sh}}}{d_A(z)} \simeq \frac{R_{\text{sh}}}{R_O} (1+z), \text{ for } R_O \gg m. \quad (145)$$

To determine the value of  $R_{\text{sh}}$ , we must identify an intermediary region in which both expressions for the BH shadow in the inner and outer regions are valid. This will allow us to match the solutions and determine  $R_{\text{sh}}$ .

**Remark 6.2.** Unlike other cosmological BH solutions, the McVittie spacetime connects the inner and outer regions through a continuous interpolation. This ensures a smooth transition such that paths do not need to be computed in a piecewise manner [47].

#### 6.4.5 The intermediate region

Let  $r_{\text{inner}}$  denote the scale at which the result in equation 141 for  $\alpha_{\text{inner}}$  holds, and let  $r_{\text{outer}}$  be the length scale at which the cosmological shadow  $\alpha_{\text{outer}}$  in equation 147 is valid. Then there must exist some intermediate region  $\bar{r}$  in which the results from both regions give the same angular size, i.e.  $\alpha_{\text{inner}}(\bar{r}) = \alpha_{\text{outer}}(\bar{r})$ , for a universe whose expansion is sufficiently small [12, 47, 65]. This region is subject to the inequality:

$$r_{\text{inner}} \ll \bar{r} \ll r_{\text{outer}},$$

and is characterised by having insignificant effects of cosmic expansion, and also a negligible gravitational influence from the central BH. The left inequality leads to the further assumption that  $m \sim r_{\text{inner}} \ll \bar{r}$ , while the right yields  $\bar{r} \ll \frac{1}{H_0}$ , since  $1 \ll z$  [65].

In the former region, we can approximate our result in 141 for an observer at  $\bar{r} \gg m$  [65]:

$$\alpha_{\text{inner}}(\bar{r}) \simeq \frac{3\sqrt{3}m}{\bar{r}}, \text{ for } \bar{r} \gg m, \quad (146)$$

while the angular size using equation 145 becomes:

$$\alpha_{\text{outer}}(\bar{r}) = \frac{R_{\text{sh}}}{\bar{r}}, \text{ for } z \ll 1. \quad (147)$$

In this simple analysis, the validity of both results in the intermediate region will imply that the intrinsic radius of the locally Schwarzschild BH will be  $R_{\text{sh}} = 3\sqrt{3}m \equiv b_{\text{cr}}$ , as was to be expected.

**Remark 6.3.** The equivalence between the intrinsic radius and the critical impact parameter of the BH is intuitive to grasp. Since the critical impact parameter describes the apparent angular size due to light-bending effects, which are always present, it is only fair to say that this can also be interpreted as the actual radius of the BH. Light rays are always interpreted as originating from a sphere with radius  $b_{\text{cr}}$  [12].

To describe the approximate size of the shadow, valid for any observer distance  $R_O$ , we can sum the individual solutions and subtract a term which corresponds to the angular size in the overlap region between the two asymptotic regions. More specifically, the solution will take the form [29, 65]:

$$\alpha_{\text{sh}}(R_O) = \alpha_{\text{inner}}(R_O) + \alpha_{\text{outer}}(R_O) - \alpha_{\text{overlap}}(R_O),$$

where  $\alpha_{\text{overlap}}$  is obtained from the intermediary region conditions:

$$\alpha_{\text{overlap}}(\bar{r}) = \alpha_{\text{inner}}(\bar{r}) = \alpha_{\text{outer}}(\bar{r}) = \frac{3\sqrt{3}m}{\bar{r}}.$$

Hence, we obtain an approximate general expression for the shadow of a McVittie BH as [65]:

$$\alpha_{\text{sh}}(R_O) = \arcsin \left[ \frac{3\sqrt{3}m}{R_O} \sqrt{1 - \frac{2m}{R_O}} \right] + \frac{3\sqrt{3}m}{d_A(z)} - \frac{3\sqrt{3}m}{R_O}. \quad (148)$$

Unfortunately, showcasing the angular size of this shadow as a function of distance, will require us to determine  $d_A(z)$  analytically by computing  $\int \frac{dz}{H(\bar{z})}$ , which is usually not possible without making any simplifying assumptions [15]. For this reason, we shall assume that

the universe is matter-dominated, since we have already explored the dynamics of a dark energy-dominated universe when we studied the Kottler spacetime.

A flat matter-dominated FLRW universe is characterised by the parameters:  $(\Omega_{m0}, \Omega_{r0}, \Omega_{\Lambda0}) = (1, 0, 0)$ . Our universe likely experienced such an epoch in its earlier life, as discussed in [6]. Under the dominance of matter, we find that:

$$\begin{aligned} d_{A,m}(z) &= \frac{1}{1+z} \int_0^z \frac{d\bar{z}}{H_0 \sqrt{1(1+\bar{z})^3 + 0(1+\bar{z})^4 + 0}} \\ &\Rightarrow = \frac{1}{1+z} \frac{2}{H_0} [(1+z)^{-1/2}] \Big|_{\bar{z}=0}^{\bar{z}=z} = \frac{1}{1+z} \frac{2}{H_0} [1 - (1+z)^{-1/2}] \end{aligned} \quad (149)$$

Once again, since the angular diameter distance becomes relevant in the high redshift regime of the background cosmology, we can estimate using 144 and 145:

$$R_O = \frac{2}{H_0} [1 - (1+z)^{-1/2}], \text{ and } \alpha_{\text{outer}} \simeq \frac{3\sqrt{3}m}{R_O} (1+z), \text{ for } R_O \gg m.$$

Substituting  $R_O$  in the latter equation and removing any  $z$  dependence leads us to the angular size of a BH shadow in a matter-dominated FLRW universe:

$$\begin{aligned} \alpha_{\text{sh}}(R_O) &= \arcsin \left[ \frac{3\sqrt{3}m}{R_O} \sqrt{1 - \frac{2m}{R_O}} \right] + \frac{3\sqrt{3}m}{R_O} \left( 1 - \frac{H_0 R_O}{2} \right)^{-2} - \frac{3\sqrt{3}m}{R_O} \\ &\Rightarrow \alpha_{\text{sh}}(R_O) = \arcsin \left[ \frac{3\sqrt{3}m}{R_O} \sqrt{1 - \frac{2m}{R_O}} \right] + \frac{3\sqrt{3}m}{R_O} \left[ \left( 1 - \frac{H_0 R_O}{2} \right)^{-2} - 1 \right] \end{aligned} \quad (150)$$

A plot of BH shadow angular size against observer distance is shown in figure 30, for the Schwarzschild BH embedded in a matter-dominated FLRW cosmology. In contrast to a dark energy-dominated universe, the shadow not only remains finite as observer distance increases, but actually grows in size. This can be explained by closely examining the behaviour of the angular diameter distance from equation 149, with respect to a variable redshift:

$$d_{A,m}(z) = \frac{1}{1+z} \frac{2}{H_0} [1 - (1+z)^{-1/2}] \mapsto \frac{d}{dz} d_{A,m}(z) = \frac{1}{(1+z)^2} \frac{2}{H_0} \left[ \frac{3/2}{\sqrt{1+z}} - 1 \right]$$

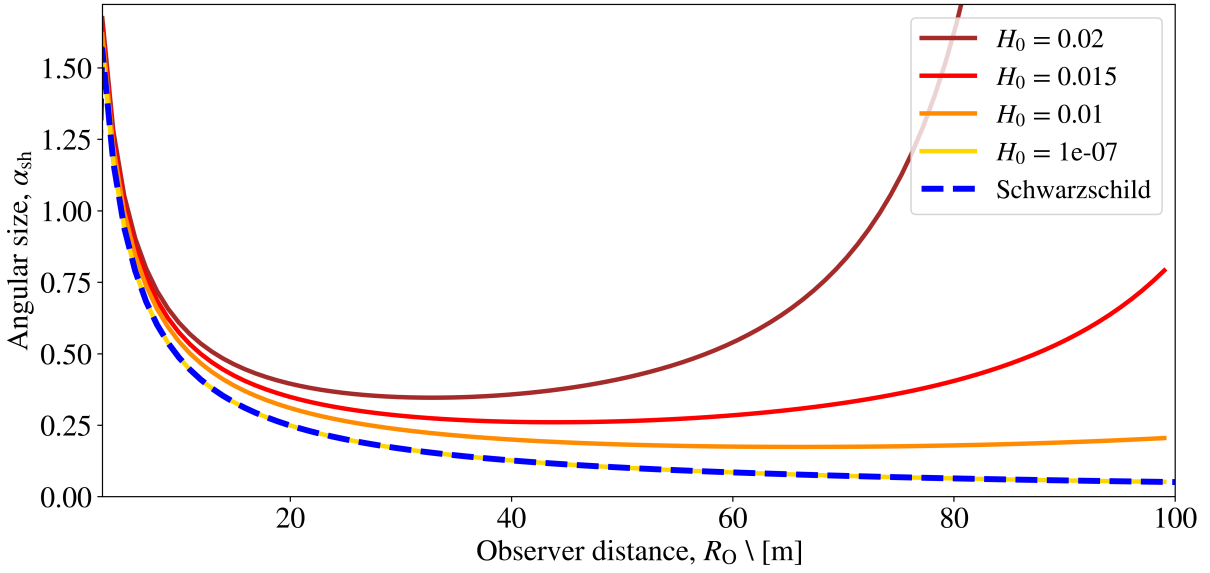


Figure 30: Plot showcasing the angular sizes of BH shadows in a McVittie spacetime. In particular, it was assumed that the Schwarzschild BH of mass  $m = 1$  was embedded in a matter-dominated FLRW cosmology. The Hubble constant was varied to distinguish the effects of rapid expansion on the shadow. While the shadow coincides with the Schwarzschild shadow close to the photon sphere, it diverges as  $R_O$  is increased. This plot generalises figure 2 from [65]. The program used to plot this figure can be found in appendix B.12.

By setting the derivative equal to zero, we can deduce that there is a maximum turning point at  $z = \frac{5}{4}$ , beyond which  $d_{A,m}(z)$  decreases asymptotically to zero. Hence, in the region of significant cosmological expansion, where the angular size of the BH shadow is approximated as  $\alpha_{\text{sh}} \simeq \alpha_{\text{outer}} = \frac{3\sqrt{3}m}{d_{A,m}(z)}$ , we see that this begins to increase indefinitely due to the  $\frac{1}{d_{A,m}(z)}$  term. A plot of  $d_{A,m}(z)$  and  $\alpha_{\text{outer}}(z)$  against redshift has been plotted in figure 31.

**Remark 6.4.** Compare this to a Kottler BH in a dark energy-dominated universe, whose shadow was found to asymptotically decrease to  $3\sqrt{3}mH_0$  (see equation 134).

## 6.5 BH shadows in a general cosmology

Our universe has undergone a few epochs of distinct cosmological expansion. In its current state, the universe is exhibiting a dark energy-driven expansion, with traces of matter

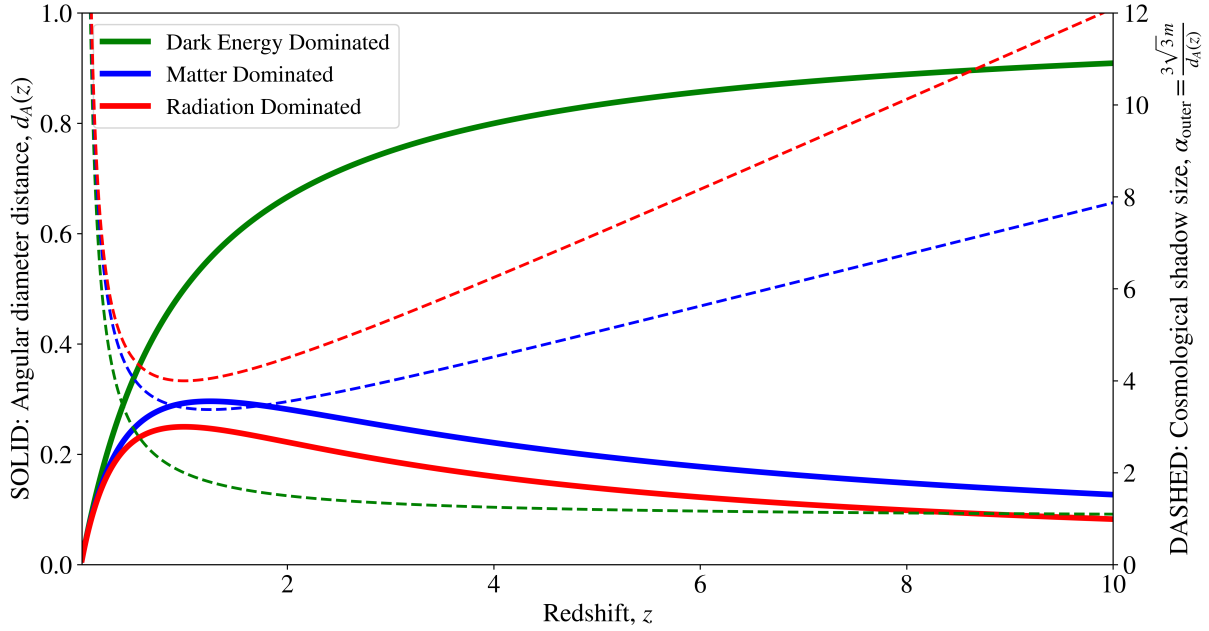


Figure 31: Plot of angular diameter distance (solid line) and BH shadow size in the outer cosmological region (dashed line). This plot describes a BH of mass  $m = 1$  embedded in an expanding McVittie spacetime with  $H_0 = 1$ . Note that in the region of low redshift,  $\alpha_{\text{outer}}$  is not representative of the actual BH shadow size since  $\alpha_{\text{inner}}$  and  $\alpha_{\text{overlap}}$  are non-negligible! The program used to plot this figure can be found in appendix B.13.

contribution [15, 38, 41]. We have already seen how the effects of this expansion lead to a lensing of the BH shadow. In particular, it is also worth deriving the cosmological term in the angular size of a BH shadow,  $\alpha_{\text{outer}}$ , for a radiation and a dark energy-dominated universe.

For a purely radiation-driven expansion, we derive:

$$d_{A,r}(z) = \frac{1}{1+z} \frac{1}{H_0} [1 - (1+z)^{-1}],$$

which is found through the same method employed previously, with  $(\Omega_{m0}, \Omega_{r0}, \Omega_{\Lambda0}) = (0, 1, 0)$ . On the other hand, a dark energy-dominated universe with  $(\Omega_{m0}, \Omega_{r0}, \Omega_{\Lambda0}) = (0, 0, 1)$  gives:

$$d_{A,\Lambda}(z) = \frac{1}{H_0} \frac{z}{1+z},$$

which is monotonically increasing to  $d_{A,\Lambda}(z) = \frac{1}{H_0}$ , as  $z \rightarrow \infty$ . These have also been plotted

in figure 31, together with the  $\alpha_{\text{outer}}(z)$  function they define. Although we have only studied the expansion in terms of the isolated components that contribute to it, in reality, the expansion is a combination of all three factors. Integrating  $\frac{1}{H(\bar{z})}$  using generalised cosmological parameters will provide the most applicable expansion model.

Studying lightlike geodesics in cosmological BH spacetimes is inherently complex, as both strong-field gravity near the BH and the large-scale expansion of the universe must be considered simultaneously. At present, there is no general analytical solution for the null geodesics of arbitrary BHs embedded in arbitrary cosmological backgrounds, especially for observers at arbitrary locations. Moreover, for any physical expansion history, the angular size of the BH shadow observed by a comoving observer remains finite, despite the increasing observer distance. This initially counterintuitive result arises from the fact that the notion of “distance” in an FLRW universe is ambiguous. Actually, this motivated our use of the more appropriate angular diameter distance,  $d_A(z)$ , as opposed to simply the radial coordinate  $R_O$  [38].

As illustrated in figure 31, the angular diameter distance is neither a monotonic function of redshift, nor of cosmic time. More specifically, we found that in a flat FLRW background,  $d_A(z)$  increased up to a certain value of  $z$ , beyond which it began to decrease again. This result stems from the fact that although at large comoving distances, the physical separation between an object and an observer leads to a smaller angular size, there will come a point at which very distant objects will appear to us as they did when the universe was much smaller and more local to us. Hence, objects of particular size appeared larger on our observable sky. This turning point is characteristic of the FLRW background model, with its specific influence directed by the contributions to energy density. The study of BH shadows in other cosmologies should be ideally be investigated so as to obtain a broader picture. Such analysis could also lead to fruitful results which can aid in identifying whether a model is well-constrained.

This might not be the case for other cosmological models.

It is important to note, however, that the intrinsic angular radius  $R_{\text{sh}}$  associated with the critical impact parameter does not correspond to the actual physical radius of the shadow. Therefore, while  $d_A(z)$  provides a useful approximation for the shadow's size at large distances, it should not be interpreted as an exact analytical method for determining the shadow in all regimes. This approximation is only valid when a spacetime can be separated into two distinct regions: an inner, gravitationally intense regime near the BH, and an outer region where the FLRW background dominates [47, 65]. Fortunately, the expansion of our universe is only significant at very large scales; in the intermediate region between these two asymptotic domains, the spacetime is approximately spatially flat [12, 15, 47].

Although we mainly concerned ourselves with deriving the shadow size in the McVittie spacetime, our approach can easily be generalised to other cosmological BH spacetimes which satisfy the assumptions made during our analysis. In such cases, the shadow size can be approximated to be Schwarzschild near the BH, and

$$\alpha_{\text{sh}}(z) \simeq \alpha_{\text{outer}}(z) = \frac{3\sqrt{3}m}{d_A(z)}, \quad (151)$$

in a region far from it. However, we are still tasked with finding a feasible analytical (or numerical) expression for the integral of  $\frac{1}{H(\bar{z})}$ . Nonetheless, equations 148 and 151 remain invaluable to our method of deriving angular sizes of general cosmological BHs [47].

---

## 7 Conclusion

In this dissertation, we have taken a detailed look at the properties of BH shadows generated in several well-known spacetimes. In particular, our discussion began by deriving the angular size of the BH shadow for two static and spherically symmetric spacetimes—the Schwarzschild and Reissner–Nordström solutions. We then considered the impact of a rotating mass, analysing both the general effects of rotation and its specific influence on the shape of the BH shadow in the Kerr geometry. This naturally led to a more physically motivated investigation of BHs embedded in an expanding universe, with the Kottler and McVittie spacetimes being studied as concrete examples of such spacetimes. A summary of these results is presented in table 2, for the reader’s convenience.

Spacetime	Observer at $(r_O, \theta_O, t_O)$	Distant observer at $r_O \gg m$
Schwarzschild	$\arcsin\left[\frac{3\sqrt{3}m}{r_O}\sqrt{1-\frac{2m}{r_O}}\right]$	$\frac{3\sqrt{3}m}{r_O}$
Reissner-Nordström	$\arcsin\left[\frac{1}{2\sqrt{2}r_O}\frac{\left[3m+\sqrt{9m^2-8Q^2}\right]^2}{\sqrt{3m^2-2Q^2+m\sqrt{9m^2-8Q^2}}}\sqrt{1-\frac{2m}{r_O}+\frac{Q^2}{r_O^2}}\right]$	$\frac{1}{2\sqrt{2}r_O}\frac{\left[3m+\sqrt{9m^2-8Q^2}\right]^2}{\sqrt{3m^2-2Q^2+m\sqrt{9m^2-8Q^2}}}$
Kerr	$-2\tan\left(\frac{\gamma(r_{ps})}{2}\right)(\sin\psi(r_{ps}), \cos\psi(r_{ps}))$	$\frac{1}{r_O}\left(\frac{a\sin^2\theta_O-\xi(r_{ps})}{\sin\theta_O}, \sqrt{\eta(r_{ps})-\frac{(\eta(r_{ps})-a\sin^2\theta_O)^2}{\sin^2\theta_O}}\right)$ [47]
Kottler (Static)	$\arcsin\left[\frac{3\sqrt{3}m}{r_O}\sqrt{\frac{1-2m/r_O-\Lambda r_O^2/3}{1-9\Lambda m^2}}\right]$	$\frac{3\sqrt{3}m}{r_O}\sqrt{1-H_0^2 r_O^2}$
Kottler (Comoving)	$\arcsin\left[\frac{3\sqrt{3}m}{r_O}\sqrt{1-\frac{2m}{r_O}}\sqrt{1-27H_0^2 m^2} + 3\sqrt{3}m H_0 \sqrt{1-\frac{27m^2}{r_O^2}}\left(1-\frac{2m}{r_O}\right)\right]$	$\frac{3\sqrt{3}m}{r_O}\left(\sqrt{1-27H_0^2 m^2} + H_0 r_O\right)$
McVittie	$\arcsin\left[\frac{3\sqrt{3}m}{r_O}\sqrt{1-\frac{2m}{r_O}} + \frac{3\sqrt{3}m}{d_A(z)} - \frac{3\sqrt{3}m}{r_O}\right]$	$\frac{3\sqrt{3}m}{d_A(z)}$

Table 2: A summary of the results obtained from our discussion, in regards to the angular sizes of BH shadows. In the case of the Kerr spacetime, this is given as a parametric curve due to the non-circular nature of the BH shadow. Moreover, its distant observer approximation was taken from [47].

It should be noted, however, that neither the Kottler nor the McVittie spacetimes pro-

---

vided entirely realistic models of cosmological BHs. Recall that the Kottler spacetime described a universe dominated entirely by a positive cosmological constant, neglecting the matter and radiation content that dominated most of cosmic expansion historically. Meanwhile, the McVittie spacetime, while incorporating a realistic FLRW background, possessed a curvature singularity at the location of its event horizon, limiting its physical applicability. These drawbacks suggest that future research should investigate more physically consistent cosmological BH solutions.

One way to expand our research on BH shadows would be to investigate the effects of BH rotation in a cosmological background. The simplest metric describing such a universe is the Kerr–de Sitter, which has already been investigated extensively. In particular, [60] provides a detailed study on the size of its BH shadow (light escape cone) and also its general photon trajectories. Furthermore, more general solutions such as the Kerr–Newman–NUT–de Sitter can also be considered, given that they exhibit a much more complex and rich shadow structure [26, 27]. In either case, however, the cosmic expansion is once again driven solely by dark energy. This highlights the large lack of cosmological spacetimes describing rotating BHs, especially ones that provide a realistic cosmological background model.

As for generalising our discussion to other cosmological backgrounds, we can consider BHs embedded in alternate theories of gravity such as the  $f(R)$ , where particular examples include the Starobinsky and Hu–Sawicki  $f(R)$  homogeneous cosmological background models. These particular spacetimes are derived by modifying the Einstein–Hilbert action in a way to incorporate a function of the Ricci scalar  $f(R)$ . This procedure alters the EFEs in a way which allows for them to be independent of  $\Lambda$ . Such models are becoming increasingly of interest since they show good conformity with late-time cosmic data, such as with cosmic chronometers, Baryon Acoustic Oscillations, Supernovae type Ia and Hubble parameter data [21, 54]. Hence, one natural avenue for future work is to replace the FLRW background in the McVittie-like setup with either a Starobinsky or Hu–Sawicki cosmology, and consider a

---

Schwarzschild BH embedded in such modified backgrounds.

Obviously, these cosmologies do not describe mass inhomogeneities embedded within them. However, if we do choose to consider an embedded central BH, then spacetime will locally resemble the Schwarzschild solution, provided that the expansion of the universe is sufficiently slow. Moreover, this allows for an intermediate region of flat spacetime to exist once again. This scenario satisfies the assumptions made in deriving equation 148, which motivates its validity for alternate  $f(R)$  backgrounds. Indeed, for such spacetimes, the same method can be applied as with the McVittie case. The process of obtaining a composite numerical solution for the angular size of the BH shadow will involve obtaining  $d_A(z)$  using a modified form of the Hubble parameter, which is defined differently in each of the background  $f(R)$  models. Equation 148 can then be applied to obtain the shadow’s angular size as a function of observer distance. It is interesting to investigate whether these will show similar conformity to our results, or will yield a shadow size that behaves differently with an increasing observer distance. Papers such as [7, 11, 31, 40] can serve as a guide to explore the prospects of deriving shadow sizes in these spacetimes.

Another prospect for future work lies in relaxing one of the most restrictive assumptions made throughout the dissertation – that BHs are illuminated by a dense and uniform distribution of background sources. In reality, very few BHs are actually found under such idealised conditions, as the majority of BHs are instead illuminated by their surrounding accretion disks [42]. Such a close source of light will naturally yield much more pronounced light-bending effects as seen in figure 7, and likely in the images made by the EHT. Although the size of the shadow remains unaffected, it might become obstructed due to this orbiting matter. Moreover, the obstruction might be more worsened if the BH also exhibits rotation. This topic is discussed meticulously in [69], but remains of particular interest.

Beyond their theoretical interest, BHs shadows can also serve as tools to assess the va-

---

lidity of cosmological models. In particular, equation 148 shows that the shadow size is generally sensitive to mass, redshift and observer distance. Moreover, for a distant BH, this dependence reduces to only redshift and angular diameter distance (see equation 151). Hence, measurements of angular size and mass for BH shadows at high redshift can be used to estimate the angular diameter distance. If we also have an independent measurement of the BH's redshift, then we can determine the precise dependence of  $d_A(z)$  on  $z$ . The results of such an observation will allow us to plot a graph similar to that found in figure 31. More importantly, this will also allow us to infer the density parameters of the late-time universe  $(\Omega_{0m}, \Omega_{0r}, \Omega_{0\Lambda})$ , using equation 107 [47, 66].

Dually, for BHs at small redshift, the most important parameter in cosmology – the Hubble constant  $H_0$ , can be estimated. Indeed, for  $z \ll 1$ , we can approximate  $d_A(z) \simeq \frac{z}{H_0}$  [47], and hence deduce the Hubble constant using equation 151 as:

$$H_0 = \frac{\alpha_{sh} z}{3\sqrt{3}m}.$$

Alternatively, by comparing observed shadow sizes with predicted ones using models of  $H(z)$  obtained from alternate theories of gravity, we can also place meaningful constraints on the value of  $H_0$  [66]. Such an independent method would definitely aid in resolving the longstanding Hubble tension present in modern cosmology [47]. However, while current instrumentation limits our ability to exploit these ideas, this will hopefully change in the near future. In any case, it is important to develop our theory sufficiently in preparation for its subsequent use. An account of the prospects and limitations of using BH shadows as "standard rulers" is given in [47, 66, 67].

In summary, while this thesis has focused primarily on idealised BH spacetimes, the results developed here are foundational for the analysis of any BH spacetime, with a particular interest towards cosmological applications. By extending these methods to more realistic, time-dependent, and modified gravity spacetimes, we can hope to gain a deeper understanding of our universe using the shadows of its most mysterious objects.

---

## A Derivation of curvature invariants for McVittie spacetime

The Black Hole Perturbation Toolkit package in Mathematica [1] is a useful tool which can be used to compute the curvature tensors of any given spacetime. In particular, deriving the curvature invariants for the McVittie spacetime is no easy task. This process was simplified greatly using this package.

The Ricci Scalar of the McVittie spacetime was found to be:

$$R = \frac{6}{a(t)^2(2ra(t) - m)} [(2ra(t) - 3m)\dot{a}(t)^2 + a(t)(m + 2ra(t))\ddot{a}(t)].$$

Although this form suffices for our analysis, we shall express it in terms of the following substitutions:

$$\frac{m}{2ra(t)} \rightarrow \mu, \quad \left(\frac{\dot{a}(t)}{a(t)}\right)^2 \rightarrow H(t)^2, \quad \text{and} \quad \frac{\ddot{a}(t)}{a(t)} \rightarrow H(t)^2 + \dot{H}(t),$$

which were all defined previously. This simplifies the Ricci scalar to [53]:

$$R = 12H(t)^2 + 6\dot{H}(t)\frac{1+\mu}{1-\mu}. \quad (152)$$

To derive the pressure due to the compact mass distribution, we must first assume that our universe can be modelled as a perfect fluid. This type of assumption is commonly used in literature [2, 15, 38]. In the rest frame of such a fluid, the energy-momentum tensor will take the special form:

$$T_\nu^\mu = \text{diag}(-\rho, p, p, p).$$

In order to access the pressure terms of this tensor, we need to obtain the components of the Einstein tensor and equate  $G_{rr} = \kappa T_{rr}$  using the EFEs. Using Mathematica once again, we obtain the  $G_{rr}$  component of the Einstein tensor as:

$$\begin{aligned} G_{rr} &= -\frac{(m + 2ra(t))^4}{16r^4a(t)^4(-m + 2ra(t))} [(-5m + 2ra(t))\dot{a}(t)^2 + 2a(t)(m + 2ra(t))\ddot{a}(t)] \\ &\implies -a(t)^2(1 + \mu)^4 \left[ 3H(t)^2 + 2\dot{H}(t)\frac{1+\mu}{1-\mu} \right]. \end{aligned}$$

---

Hence, equating this term to the RHS of the EFEs, we find:

$$\begin{aligned} \kappa(p g_{rr}) &=: \kappa T_{rr} = G_{rr} \\ \kappa p \cancel{[a(t)^2(1+\mu)^4]} &= -\cancel{a(t)^2(1+\mu)^4} \left[ 3H(t)^2 + 2\dot{H}(t) \frac{1+\mu}{1-\mu} \right] \\ \implies p &= -\frac{1}{8\pi} \left[ 3H(t)^2 + 2\dot{H}(t) \frac{1+\mu}{1-\mu} \right], \text{ since } \kappa = 8\pi. \end{aligned}$$

Lastly, the Kretschmann scalar is obtained straightforwardly with the appropriate command in Mathematica. Its lengthy expression is readily stated in equation 138. The code used to obtain all these curvature invariants is shown below:

```
In[1]:= << GeneralRelativityTensors`  
mu = m / (2 a[t] r);  
a'[t] = H[t] a[t];  
a''[t] = a[t] (H'[t] + H^2[t]);  
  
g = ToMetric[{"McVittie", "dx"}, {t,  
    r, Theta, Phi}, {{-((1 - mu)/(1 + mu))^2, 0, 0, 0}, {0,  
    a[t]^2 (1 + mu)^4, 0, 0}, {0, 0, r^2 a[t]^2 (1 + mu)^4, 0}, {0,  
    0, 0, r^2 Sin[Theta]^2 a[t]^2 (1 + mu)^4}}];  
TensorValues[g] // MatrixForm  
RicScalar = RicciScalar[g] // TensorValues // Simplify  
EinsTensor = EinsteinTensor[g] // TensorValues // Simplify  
KretschScalar = KretschmannScalar[g] // TensorValues // Simplify  
  
Simplify[Solve[EinsTensor[[2, 2]] == 8 Pi a[t]^2 (1 + mu)^4 P, P]]
```

---

## B Python code for plots

In this appendix, the Python programs used to calculate quantities, and plot the figures featured in this dissertation are presented. All programs were developed in JupyterLab 3.6.3 using Python 3.

### B.1 Plot 10

```
1 import numpy as np
2 import matplotlib.pyplot as plt
3
4 np.seterr(divide = 'ignore')
5 plt.rcParams["font.size"] = 22
6 plt.rcParams['axes.facecolor'] = 'yellow'
7 plt.rcParams["font.weight"] = "normal"
8 plt.rcParams['font.family'] = 'STIXGeneral'
9 plt.rcParams['mathtext.fontset'] = 'stix'
10
11 def main(m, r):
12     (m1, m2, m3) = m
13     (r1, r2, r3, r4) = r
14
15     lower_x = - 0.2*r1
16     upper_x = r4 + 1/r4 + 0.2*r1
17
18     lower_y = m3 - m3/(r1*m1) - 0.2*r1
19     upper_y = m1 + m1/(r1*m1) + 0.2*r1
20
21     theta = np.linspace(0, 2*np.pi, 1000)
22     sin_theta = np.sin(theta)
23     cos_theta = np.cos(theta)
24
25
```

```

26 plt.figure(figsize=(1.5*r4, 1.5*(upper_y - lower_y)*r4/(upper_x -
27   lower_x)), facecolor='white')
28 plt.xlim(lower_x, upper_x)
29 plt.ylim(lower_y, upper_y)
30
31 plt.xlabel(r"Observer Distance, $r_{\text{0}}$ [m]")
32 plt.ylabel(r"Geometric mass, $m \cdot G_c^{-2}$ [m]")
33 plt.xticks([r1, r2, r3, r4])
34 plt.yticks([m1, m2, m3])
35
36 plt.axvline(r1, color='gray', linestyle='--', linewidth=1)
37 plt.axvline(r2, color='gray', linestyle='--', linewidth=1)
38 plt.axvline(r3, color='gray', linestyle='--', linewidth=1)
39 plt.axvline(r4, color='gray', linestyle='--', linewidth=1)
40
41 plt.axhline(m1, color='gray', linestyle='--', linewidth=1)
42 plt.axhline(m2, color='gray', linestyle='--', linewidth=1)
43 plt.axhline(m3, color='gray', linestyle='--', linewidth=1)
44
45 #m1
46 plt.fill(m1*cos_theta/(r1*m1) + r1, m1*sin_theta/(r1*m1) + m1, '-
47   color='k', linewidth=5)
48 plt.fill(m1*cos_theta/(r2*m1) + r2, m1*sin_theta/(r2*m1) + m1, '-
49   color='k', linewidth=5)
50 plt.fill(m1*cos_theta/(r3*m1) + r3, m1*sin_theta/(r3*m1) + m1, '-
51   color='k', linewidth=5)
52 plt.fill(m1*cos_theta/(r4*m1) + r4, m1*sin_theta/(r4*m1) + m1, '-
53   color='k', linewidth=5)

```

```

53     plt.fill(m2*cos_theta/(r2*m1) + r2, m2*sin_theta/(r2*m1) + m2, '–',
54             color='k', linewidth=5)
55     plt.fill(m2*cos_theta/(r3*m1) + r3, m2*sin_theta/(r3*m1) + m2, '–',
56             color='k', linewidth=5)
57     plt.fill(m2*cos_theta/(r4*m1) + r4, m2*sin_theta/(r4*m1) + m2, '–',
58             color='k', linewidth=5)
59
60     #m3
61     plt.fill(m3*cos_theta/(r1*m1) + r1, m3*sin_theta/(r1*m1) + m3, '–',
62             color='k', linewidth=5)
63     plt.fill(m3*cos_theta/(r2*m1) + r2, m3*sin_theta/(r2*m1) + m3, '–',
64             color='k', linewidth=5)
65     plt.fill(m3*cos_theta/(r3*m1) + r3, m3*sin_theta/(r3*m1) + m3, '–',
66             color='k', linewidth=5)
67
68     # plt.savefig(f"Schwarzschild.png", bbox_inches='tight', dpi=300)
69
70
71
72 main(m=(4, 2, 1), r=(1, 3, 6, 10))

```

## B.2 Plot 11

```

1 import matplotlib.pyplot as plt
2 import math
3 import numpy as np
4
5 plt.rcParams["font.size"] = 20
6 plt.rcParams["font.weight"] = "normal"
7 plt.rcParams['font.family'] = 'STIXGeneral',
8 plt.rcParams['mathtext.fontset'] = 'stix'
9
10 def scale_factor(m, L):

```

```

11     num = (1 - 2 * m / r0 - L* r0**2 / 3)
12     den = (1 - 9 * L * m**2)
13     kottler_shadow = np.arcsin( (3*m*np.sqrt(3)/r0) * np.sqrt(num/den) )
14     return kottler_shadow
15
16 def plot_potential(m):
17     q = np.linspace(0, m, 1000)[1:-1]
18
19     inner_eh = m - (np.sqrt(m**2 - q**2))
20     outer_eh = m + (np.sqrt(m**2 - q**2))
21
22     inner_ps = 3 * m / 2 - (np.sqrt(9 * m**2 - 8 * q**2))/2
23     outer_ps = 3 * m / 2 + (np.sqrt(9 * m**2 - 8 * q**2))/2
24
25     plt.figure(figsize=(14, 6), facecolor='white')
26     plt.xlabel(r"Charge, $Q$ \ [m]")
27     plt.ylabel(r"Radial distance, $r$ \ [m]")
28     plt.axhline(m, linestyle='--', color='k')
29
30     plt.axvline(0, linestyle='--', color='k')
31     plt.xlim(0, m)
32     plt.ylim(1.05*min(inner_ps)-1e-1, 1.25*max(outer_ps))
33
34     plt.plot(q, outer_ps, 'b', label=r'Outer Photon Sphere, $r_{\text{ps}}$',
35               linewidth=4)
36     plt.plot(q, outer_eh, 'k', label=r'Outer Event Horizon, $r_{\text{eh}}$',
37               linewidth=4)
38     plt.plot(q, inner_ps, 'r', label=r'Inner Photon Sphere, $r_{\text{ps}}$',
39               linewidth=4)
40     plt.plot(q, inner_eh, 'orange', label=r'Inner Event Horizon, $r_{\text{eh}}$',
41               linewidth=4)
42
43     plt.legend(fontsize=17, loc=1, ncols=2)
44     plt.savefig(fr"C:\Users\dimit\Computational Physics\Thesis\Reissner

```

```

Nordstrom Structure.png", bbox_inches='tight', dpi=500)

41
42 plot_potential(m=1)

```

### B.3 Plot 12

```

1 import numpy as np
2 import matplotlib.pyplot as plt
3
4 plt.rcParams["font.size"] = 22
5 plt.rcParams['axes.facecolor'] = 'yellow'
6 plt.rcParams["font.weight"] = "normal"
7 plt.rcParams['font.family'] = 'STIXGeneral'
8 plt.rcParams['mathtext.fontset'] = 'stix'
9
10 def scale_factor(m, q):
11     sqrt_discriminant = np.sqrt(9 * m ** 2 - 8 * q ** 2)
12     return (3 * m + sqrt_discriminant) ** 2 / np.sqrt(3 * m ** 2 - 2 * q
13     ** 2 + m * sqrt_discriminant) / 160
14
15 def main(m, q):
16     A = 160
17
18     lower_x = min(q) - scale_factor(m, min(q)) - 0.3 * scale_factor(m, max(q))
19
20     upper_x = max(q) + scale_factor(m, max(q)) + 0.3 * scale_factor(m, max(q))
21
22     lower_y = m - scale_factor(m, min(q)) - 1.4 * scale_factor(m, max(q))
23     upper_y = m + scale_factor(m, min(q)) + 1.4 * scale_factor(m, max(q))
24
25     plt.figure(figsize=(1.8*m, 1.8*(upper_y - lower_y)*m/(upper_x -
26     lower_x)), facecolor='white')
27     plt.xlabel(r"Charge, $Q$ \ [m]")

```

```

25     plt.xticks(q)
26     plt.xlim(lower_x, upper_x)
27     plt.ylabel(r"Geometric mass, $m \sqrt{G c^2/m}$ [m]")
28     plt.yticks([m])
29     plt.ylim(lower_y, upper_y)
30
31     theta = np.linspace(0, 2*np.pi, 1000)
32     sin_theta = np.sin(theta)
33     cos_theta = np.cos(theta)
34
35     for charge in q:
36         plt.fill(scale_factor(m, charge)*cos_theta + charge, scale_factor(m, charge)*sin_theta + m, 'r', color='k', linewidth=5)
37         plt.plot(1.05*scale_factor(m, m)*cos_theta + charge, 1.05*scale_factor(m, m)*sin_theta + m, 'r', color='w', linewidth=1.5)
38
39     plt.savefig(f'ReissnerNordstrom Shadow.png', bbox_inches='tight', dpi=300)
40
41 main(m=10, q=(0, 3, 6, 8, 10))

```

## B.4 Plot 13

```

1 import numpy as np
2 import matplotlib.pyplot as plt
3
4 plt.rcParams["font.size"] = 22
5 plt.rcParams['axes.facecolor'] = 'white'
6 plt.rcParams["font.weight"] = "normal"
7 plt.rcParams['font.family'] = 'STIXGeneral'
8 plt.rcParams['mathtext.fontset'] = 'stix'
9
10 def scale_factor(m, q):
11     sqrt_discriminant = np.sqrt(9 * m ** 2 - 8 * q ** 2)

```

```

12     return (3 * m + sqrt_discriminant) ** 2 / np.sqrt(3 * m ** 2 - 2 * q
13     ** 2 + m * sqrt_discriminant)
14
15 def plot_event_horizon_comparison(m, r0):
16     charge_array = np.linspace(0, m, 1000)
17
18     pos_RN_size = scale_factor(m=m, q=charge_array)/(4 * np.sqrt(2) * r0)
19     pos_Sch_size = np.ones(1000) * (3 * np.sqrt(3) * m) / (2 * r0)
20
21     neg_RN_size = -pos_RN_size
22     neg_Sch_size = -pos_Sch_size
23
24     plt.figure(figsize=(13, 6), facecolor='white')
25     plt.ylabel(r"Angular size, $\alpha_{\text{sh}}$")
26     plt.xlabel(r"Charge, $Q$ [m]")
27     plt.xlim(0, m)
28     plt.ylim(-1.07*max(pos_Sch_size), 1.07*max(pos_Sch_size))
29
30     plt.plot(charge_array, pos_RN_size, 'r', label=r'Reissner-Nordstr\'
31               ddot{o}m', linewidth=3)
32     plt.plot(charge_array, pos_Sch_size, 'b', label="Schwarzschild",
33               linewidth=3)
34     plt.plot(charge_array, neg_RN_size, 'r', linewidth=3)
35     plt.plot(charge_array, neg_Sch_size, 'b', linewidth=3)
36     plt.legend(loc=6)
37
38     # plt.savefig(f"ReissnerNordstrom vs Schwarzschild.png", bbox_inches='
39                 tight', dpi=500)
40
41 plot_event_horizon_comparison(m=1, r0 = 100)

```

## B.5 Plot 16

```

1 import matplotlib.pyplot as plt
2 import math

```

```

3 import numpy as np
4
5 plt.rcParams["font.size"] = 23
6 plt.rcParams["font.weight"] = "normal"
7 plt.rcParams['font.family'] = 'STIXGeneral'
8 plt.rcParams['mathtext.fontset'] = 'stix'
9
10 def plot_BH_regions(m, a, axis):
11     theta = np.arange(0, 2 * np.pi, 0.001)
12
13     outer_eh = (m + np.sqrt(m**2 - a**2))*np.cos(theta-theta)
14     inner_eh = (m - np.sqrt(m**2 - a**2))*np.cos(theta-theta)
15     ergosphere = m + np.sqrt(m**2 - a**2*np.cos(theta)**2)
16
17     axis.plot(theta, ergosphere, 'blue', label=r'Ergosphere', linewidth=4)
18     axis.plot(theta, outer_eh, 'red', label=r'Outer Event Horizon, $r_+$',
19                linewidth=4)
20     axis.plot(theta, inner_eh, 'orange', label=r'Inner Event Horizon, $r_--$',
21                linewidth=4)
22
23     axis.fill_between(theta,ergosphere, outer_eh, label=r'Ergosphere',
24                       color='cornflowerblue')
25     axis.fill_between(theta,outer_eh, inner_eh, color='salmon')
26     axis.fill(theta, inner_eh, color='khaki')
27
28 def plot_figure(m, a):
29     fig, ax = plt.subplots(nrows = 1, ncols=len(a), figsize=[26,7],
30                           subplot_kw={'projection': 'polar'})
31
32     for (axis, a) in zip(ax, a):
33         axis.set_rmax(3)
34         plot_BH_regions(m, a, axis)
35         axis.grid(True)
36         axis.set_rticks([0, 1, 2]) # Less radial ticks

```

```

33     axis.set_theta_zero_location('N')
34     axis.set_theta_direction(-1)
35     axis.set_rlabel_position(22.5) # Move radial labels away from
36     plotted line
37
38     axis.set_title(fr"$a$ = {a}, $m$ = {m}")
39
40     fig.legend([r'Ergoregion', r'Outer Event Horizon, $r_{\text{eh}}$, +'],
41                [r'Inner Event Horizon, $r_{\text{eh}}$, -'], loc=8, ncols
42                =4)
43
44     plt.savefig(f"Kerr Surfaces.png", bbox_inches='tight', dpi=500)
45
46 plot_figure(m=1, a=[0, 0.6, 0.85, 0.9999])

```

## B.6 Plot 17

```

1 import matplotlib.pyplot as plt
2 import math
3 import numpy as np
4
5 plt.rcParams["font.size"] = 22
6 plt.rcParams["font.weight"] = "normal"
7 plt.rcParams['font.family'] = 'STIXGeneral',
8 plt.rcParams['mathtext.fontset'] = 'stix'
9
10 def plot_potential(a, r_max, m, L):
11     counter_orbit = 2*m*(1+ np.cos((2/3)*np.arccos(-a/m)))
12     co_orbit = 2*m*(1+ np.cos((2/3)*np.arccos(a/m)))
13
14     inner_eh = m - np.sqrt(m**2 - a**2)
15     outer_eh = m + np.sqrt(m**2 - a**2)
16
17     fig, axs = plt.subplots(nrows = 1, ncols=2, figsize=(18, 7))
18     fig.tight_layout(pad=2.2)
19     r = np.linspace(round(outer_eh, 3)+0.00004, r_max, 1000)

```

```

20     for plot in axs:
21         plot.axhline(y=0, color='k')
22         plot.axvline(x=0.02, color='k')
23         plot.axvline(x=inner_eh, linestyle='--', color='g', label=r'Event
24             Horizons, $r_{\text{eh}}$, $\pm$', linewidth=2.5)
25         plot.axvline(x=outer_eh, linestyle='--', color='g', linewidth=2.5)
26         plot.set_xlim(0, max(r))
27         plot.set_xlabel(r"Distance, $r$ [m]")
28
29
30     Delta = (r**2 + a**2 - 2*m*r)
31     a = abs(a)
32     Vp = (2*m*a*r + r**2 *np.sqrt(Delta))/((r**2 + a**2)**2 - Delta*a**2)
33    Vm = (2*m*a*r - r**2 *np.sqrt(Delta))/((r**2 + a**2)**2 - Delta*a**2)
34     axs[0].set_title('Co-rotating Orbits')
35     axs[0].set_ylim(1.1*min(Vm), 1.1*max(Vp))
36     axs[0].plot(r, Vp, 'b', linewidth=3)
37     axs[0].plot(r, Vm, 'r', linewidth=3)
38     axs[0].axvline(x=counter_orbit, linestyle='--', color='k')
39     axs[0].fill_between(r,Vp, Vm, color='lightgrey')
40     # axs[0].set_xticks([inner_eh, outer_eh, counter_orbit, 10])
41
42     a = - abs(a)
43     Vp = (2*m*a*r + r**2 *np.sqrt(Delta))/((r**2 + a**2)**2 - Delta*a**2)
44     Vm = (2*m*a*r - r**2 *np.sqrt(Delta))/((r**2 + a**2)**2 - Delta*a**2)
45     axs[1].set_title('Counter-rotating Orbits')
46     axs[1].set_ylim(1.1*min(Vm), 1.1*max(Vp))
47     axs[1].plot(r, Vp, 'b', label=r'$V_+(r)$', linewidth=3)
48     axs[1].plot(r, Vm, 'r', label=r'$V_-(r)$', linewidth=3)
49     axs[1].fill_between(r,Vp, Vm, color='lightgrey')
50     axs[1].axvline(x=co_orbit, linestyle='--', label=r'Unstable Circular
51             Orbits, $r_{\text{ps}}$', color='k')
52     axs[1].legend()

```

```

52
53     plt.savefig(f"Kerr Potential Plot.png", bbox_inches='tight', dpi=400)
54
55 plot_potential(a=0.8, m=1, L=2, r_max=20)

```

## B.7 Plot 19

```

1 import matplotlib.pyplot as plt
2 import math
3 import numpy as np
4
5 plt.rcParams["font.size"] = 16
6 plt.rcParams["font.weight"] = "normal"
7 plt.rcParams['font.family'] = 'STIXGeneral'
8 plt.rcParams['mathtext.fontset'] = 'stix'
9
10 def plot_potential(m):
11     a = np.linspace(0, m, 1000)
12
13     counter_orbit = 2 * m * (1 + np.cos((2 / 3) * np.arccos(abs(a) / m)))
14     co_orbit = 2 * m * (1 + np.cos((2 / 3) * np.arccos(- abs(a) / m)))
15
16     outer_eh = m + np.sqrt(m**2 - a**2)
17     inner_eh = m - np.sqrt(m**2 - a**2)
18
19     plt.figure(figsize=(17, 7), facecolor='white')
20     plt.xlim(0, 1.01)
21     plt.ylim(-0.015, 4.5*m)
22
23     plt.xlabel(r"Spin parameter, $a$ \ [m]")
24     plt.ylabel(r"Radial distance, $r$ \ [m]")
25     plt.axhline(1, linestyle='--', color='k')
26     plt.axhline(4, linestyle='--', color='k')

```

```

27 plt.plot(a, counter_orbit, 'b', label=r'Counter-rotating Orbit, $r_-\backslash
28 text{c}, +\}$', linewidth=4)
29 plt.plot(a, co_orbit, 'r', label=r'Co-rotating Orbit, $r_-\backslash\text{c}, -\}
30 \$', linewidth=4)
31 plt.plot(a, outer_eh, 'k', label=r'Outer Event Horizon, $r_-\backslash\text{eh}, +
32 \}$', linewidth=4)
33 plt.plot(a, inner_eh, 'orange', label=r'Inner Event Horizon, $r_-\backslash\text{eh},
34 \text{eh}, -\}$', linewidth=4)
35 plt.legend(ncols=2)

36 plt.savefig(f"Kerr Equatorial Orbits.png", bbox_inches='tight', dpi
37 =300)

38 plot_potential(m=1)

```

## B.8 Plots 20 and 21

```

1 import numpy as np
2 import matplotlib.pyplot as plt
3 from scipy.optimize import fsolve
4
5 plt.rcParams["font.size"] = 18
6 plt.rcParams["font.weight"] = "normal"
7 plt.rcParams['font.family'] = 'STIXGeneral',
8 plt.rcParams['mathtext.fontset'] = 'stix'
9
10 def convert_to_KS(surface, theta, a):
11     return [surface * np.cos(theta), np.sqrt(surface * surface + a * a *
12         np.cos(theta-theta)) * np.sin(theta)]
13
14 def photon_orbit_polynomial(r, T, a, m):
15     rho = r**2 + a**2 * np.cos(T)**2

```

```

16     return 4*r**2 *delta* a**2 * np.sin(T)**2 - (rho * (r - m) - 2 *r *
17         delta)**2
18
19 def plot_BH_regions(m, a, axis):
20     theta = np.linspace(0, 2*np.pi, 1000)
21     inner_region = []
22     outer_region = []
23     for T in theta:
24         radii = fsolve(photon_orbit_polynomial, [2.4*m, 4*m], args=(T, a,
25             m))
26         inner_region.append(radii[0])
27         outer_region.append(radii[1])
28
29     outer_eh = (m + np.sqrt(m**2 - a**2))*np.cos(theta-theta)
30     inner_eh = (m - np.sqrt(m**2 - a**2))*np.cos(theta-theta)
31     ergosphere = m + np.sqrt(m**2 - a**2*np.cos(theta)**2)
32
33     axis.plot(theta, ergosphere, 'blue', linewidth=4)
34     axis.plot(theta, outer_eh, 'red', linewidth=4)
35     axis.plot(theta, inner_eh, 'orange', linewidth=4)
36     axis.plot(theta, inner_region, 'magenta', linewidth=4)
37     axis.plot(theta, outer_region, 'magenta', linewidth=4)
38
39     axis.fill_between(theta, ergosphere, outer_eh, label=r'Ergosphere',
40         color='cornflowerblue')
41     axis.fill_between(theta, outer_eh, inner_eh, color='salmon', label=r'
42         Outer Event Horizon, $r_+$')
43     axis.fill(theta, inner_eh, color='gold', label=r'Inner Event Horizon,
44         $r_-$')
45     axis.fill_between(theta, inner_region, outer_region, color='magenta',
46         label='Photon Region', alpha=0.4)
47
48 def kerr_surfaces(m, a):
49     theta = np.linspace(0, 2*np.pi, 500)

```

```

44     inner_region = []
45     outer_region = []
46     for T in theta:
47         radii = fsolve(polar_photon_orbit, [2.4*m, 4*m], args=(T, a, m))
48         inner_region.append(radii[0])
49         outer_region.append(radii[1])
50
51     outer_eh = (m + np.sqrt(m**2 - a**2))*np.cos(theta-theta)
52     inner_eh = (m - np.sqrt(m**2 - a**2))*np.cos(theta-theta)
53     ergosphere = m + np.sqrt(m**2 - a**2*np.cos(theta)**2)
54     return outer_eh, inner_eh, ergosphere, inner_region, outer_region
55
56 def plot_kerr_schild(m, a):
57     fig, axis = plt.subplots(nrows = 1, ncols=len(a), figsize=[2.5 * 7,
58     0.92 * 7])
59     for (axis, a) in zip(axis, a):
60         axis.set_xlim(-4.3*m, 4.3*m)
61         axis.set_ylim(-4.3*m, 4.3*m)
62         axis.axvline(0, color='gray')
63         axis.axhline(0, color='gray')
64         axis.set_xlabel('$x$ / [m]')
65         axis.set_ylabel('$z$ / [m]')
66         axis.set_title(fr"$a$ = {a}, $m$ = {m}")
67
68     theta = np.linspace(0, 2*np.pi, 500)
69     outer_eh, inner_eh, ergosphere, inner_region, outer_region =
70     kerr_surfaces(m, a)
71
72     ergosphere_z, ergosphere_r = covert_to_KS(ergosphere, theta, a)
73     outer_z, outer_r = covert_to_KS(outer_eh, theta, a)
74     inner_z, inner_r = covert_to_KS(inner_eh, theta, a)
75     ipr_z, ipr_r = covert_to_KS(np.array(inner_region), theta, a)
    singularity = (-a, a)

```

```

76     opr_z, opr_r = convert_to_KS(np.array(outer_region), theta, a)
77
78     axis.plot(ergosphere_r, ergosphere_z, 'blue', label=r'Ergosphere',
79     linewidth=4)
80
81     axis.plot(outer_r, outer_z, 'red', label=r'Outer Event Horizon,
82     $r_+$', linewidth=4)
83
84     axis.plot(inner_r, inner_z, 'orange', label=r'Inner Event Horizon,
85     $r_-$', linewidth=4)
86
87     axis.plot(ipr_r, ipr_z, 'magenta', linewidth=4)
88
89     axis.scatter(singularity, (0, 0), c='k', linewidth=1, zorder=10,
90     label="Curvature Singularity")
91
92     axis.plot(opr_r, opr_z, 'magenta', linewidth=4)
93
94
95     axis.fill(opr_r, opr_z, color='magenta', alpha=0.4)
96     axis.fill(ipr_r, ipr_z, color='white')
97     axis.fill(ergosphere_r, ergosphere_z, color='cornflowerblue',
98     alpha=0.6)
99
100    axis.fill(outer_r, outer_z, color='salmon')
101
102    axis.fill(inner_r, inner_z, color='khaki')

103
104    fig.tight_layout()
105    fig.subplots_adjust(bottom=0.21)
106
107    fig.legend(['Ergoregion', r'Outer Event Horizon, $r_{\text{eh}}$',
108               r'Inner Event Horizon, $r_-$',
109               'Photon Region', r'Curvature Singularity'], ncols=5, loc
110               =8, fontsize=20)
111
112    # plt.savefig(f"Kerr Schild Surfaces.png", bbox_inches='tight', dpi
113    =800)

114
115
116 def plot_boyer_lindquist(m, a):
117
118     fig, ax = plt.subplots(nrows = 1, ncols=len(a), figsize=[21,6],
119     subplot_kw={'projection': 'polar'}) #22
120
121     for (axis, a) in zip(ax, a):
122
123         axis.set_rmax(4.3)
124
125         axis.grid(True)

```

```

101     axis.set_rticks([0, 1, 2, 3, 4])    # Less radial ticks
102
103     axis.set_theta_zero_location('N')
104
105     axis.set_theta_direction(-1)
106
107     axis.set_rlabel_position(22.5)    # Move radial labels away from
108     plotted line
109
110     axis.set_title(fr"$a\$ = {a}, \$\quad m\$ = {m}$")
111
112
113     theta = np.linspace(0, 2*np.pi, 500)
114
115     outer_eh, inner_eh, ergosphere, inner_region, outer_region =
116     kerr_surfaces(m, a)
117
118     axis.plot(theta, ergosphere, 'blue', linewidth=4)
119
120     axis.plot(theta, outer_eh, 'red', linewidth=4)
121
122     axis.plot(theta, inner_eh, 'orange', linewidth=4)
123
124     axis.plot(theta, inner_region, 'magenta', linewidth=4)
125
126     axis.plot(theta, outer_region, 'magenta', linewidth=4)
127
128
129     axis.fill_between(theta, ergosphere, outer_eh, label=r'Ergosphere',
130     , color='cornflowerblue')
131
132     axis.fill_between(theta, outer_eh, inner_eh, color='salmon', label
133 =r'Outer Event Horizon, $r_+$')
134
135     axis.fill(theta, inner_eh, color='gold', label=r'Inner Event
136     Horizon, $r_-$')
137
138     axis.fill_between(theta, inner_region, outer_region, color=
139     magenta', label='Photon Region', alpha=0.4)
140
141
142     fig.legend([r'Ergoregion', r'Outer Event Horizon, $r_{\text{eh}, +}$',
143                 r'Inner Event Horizon, $r_{\text{eh}, -}$', 'Photon Region',
144                 ], loc=8, ncols=4)
145
146     # plt.savefig(f"Kerr Photon Region.png", bbox_inches='tight', dpi=400)
147
148
149     plot_boyer_lindquist(m=1, a=[0?, 0.5, 0.95])
150
151     plot_kerr_schild(m=1, a=[0, 0.5, 0.95])

```

## B.9 Plot 25

```

28     x = -2 * np.tan(Gamma) * np.sin(Psi)
29     y = -2 * np.tan(Gamma) * np.cos(Psi)
30     return x, y
31
32 colors = ['black', 'darkred', 'red', 'darkorange', 'gold', 'lawngreen']
33 m_list = [1, 2, 5, 10, 20]
34 a_list = [0.01, 0.3, 0.6, 0.9, 0.999]
35 r0_list = [5, 10, 20, 50, 100]
36 T0_list = [0.01, np.pi/8, 2*np.pi/8, 3*np.pi/8, np.pi/2]
37
38 fig, axis = plt.subplots(nrows = 2, ncols=2, figsize=[20,20])
39
40 for i, m in enumerate(m_list):
41     x, y = obtain_shadow(a=0.9999*m, r0=100, m=m, T0=np.pi/2)
42     axis[0, 0].plot(x, y, label=f'r'$m$ = {m}', color=colors[i], linewidth=2)
43     axis[0, 0].plot(x, -y, color=colors[i], linewidth=2)
44
45     axis[0, 0].set_title(r"$a = 0.999m, \ r_0=100, \ \theta_0=\frac{\pi}{2}$")
46     axis[0, 0].set_xlabel(r"$x(r_{\text{ps}})$")
47     axis[0, 0].set_ylabel(r"$y(r_{\text{ps}})$")
48     axis[0, 0].axvline(0, color='k')
49     axis[0, 0].axhline(0, color='k')
50
51     axis_limit=8
52     axis[0, 0].set_xlim(-0.15*axis_limit, axis_limit)
53     axis[0, 0].set_ylim(-0.625*axis_limit, 0.625*axis_limit)
54     axis[0, 0].legend(loc=3, fontsize=16, ncols=1)
55
56
57 for i, a in enumerate(a_list):
58     x, y = obtain_shadow(a=a, r0=10, m=1, T0=np.pi/2)
59     axis[0, 1].plot(x, y, label=f'r'$a$ = {a}', color=colors[i], linewidth

```

```

=2)

60 axis[0, 1].plot(x, -y, color=colors[i], linewidth=2)

61

62 axis[0, 1].set_title(r"$m = 1, \ r_{\text{0}}=10, \ \theta_{\text{0}}=\frac{\pi}{2}$")
63 axis[0, 1].set_xlabel(r"$x(r_{\text{ps}})$")
64 axis[0, 1].set_ylabel(r"$y(r_{\text{ps}})$")
65 axis[0, 1].axvline(0, color='k')
66 axis[0, 1].axhline(0, color='k')

67

68 axis_limit=2
69 axis[0, 1].set_xlim(-axis_limit, axis_limit)
70 axis[0, 1].set_ylim(-axis_limit, axis_limit)
71 axis[0, 1].legend(loc=3, fontsize=16, ncols=1)

72

73

74 for i, r0 in enumerate(r0_list):
75     x, y = obtain_shadow(a=0.999, r0=r0, m=1, T0=np.pi/2)
76     axis[1, 0].plot(x, y, label=r'$r_{\text{0}}$ = ' + str(r0), color=colors[i], linewidth=2)
77     axis[1, 0].plot(x, -y, color=colors[i], linewidth=2)

78

79 axis[1, 0].set_title(r"$m = 1, \ a = 0.999, \ \theta_{\text{0}}=\frac{\pi}{2}$")
80 axis[1, 0].set_xlabel(r"$x(r_{\text{ps}})$")
81 axis[1, 0].set_ylabel(r"$y(r_{\text{ps}})$")
82 axis[1, 0].axvline(0, color='k')
83 axis[1, 0].axhline(0, color='k')

84

85 axis_limit=9
86 axis[1, 0].set_xlim(-0.1*axis_limit, 0.9*axis_limit)
87 axis[1, 0].set_ylim(-0.5*axis_limit, 0.5*axis_limit)
88 axis[1, 0].legend(loc=3, fontsize=16, ncols=1)

89

```

```

90
91 for i, T0 in enumerate(T0_list):
92     x, y = obtain_shadow(a=0.999, r0=10, m=1, T0=T0)
93     axis[1, 1].plot(x, y, label=r'$\theta_{\text{text}}{} = ' + str(round(T0, 3))
94     , color=colors[i], linewidth=2)
95     axis[1, 1].plot(x, -y, color=colors[i], linewidth=2)
96
97     axis[1, 1].set_title(r"$m = 1, \ a = 0.999, \ r_{\text{text}}{}=10$")
98     axis[1, 1].set_xlabel(r"$x(r_{\text{text}}{})$")
99     axis[1, 1].set_ylabel(r"$y(r_{\text{text}}{})$")
100    axis[1, 1].axvline(0, color='k')
101    axis[1, 1].axhline(0, color='k')
102
103    axis_limit=2
104    axis[1, 1].set_xlim(-0.75*axis_limit, axis_limit)
105    axis[1, 1].set_ylim(-0.875*axis_limit, 0.875*axis_limit)
106
107 plt.savefig(f"Kerr BH Shadow.png", bbox_inches='tight', dpi=400)

```

## B.10 Plot 27

```

1 import matplotlib.pyplot as plt
2 import math
3 import numpy as np
4
5 plt.rcParams["font.size"] = 18
6 plt.rcParams["font.weight"] = "normal"
7 plt.rcParams['font.family'] = 'STIXGeneral',
8 plt.rcParams['mathtext.fontset'] = 'stix'
9
10 def scale_factor(m, L):
11     num = (1 - 2 * m / r0 - L * r0**2 / 3)
12     den = (1 - 9 * L * m**2)

```

```

13     kottler_shadow = np.arcsin( (3*m*np.sqrt(3)/r0) * np.sqrt(num/den) )
14
15
16 def plot_potential(m):
17     L = np.linspace(0, 1 / (9 * m**2), 1000000)[1:-1]
18
19     h = np.sqrt(L / 3)
20     a = (1 / 3) * np.arccos(np.sqrt(27) * m * h)
21     inner_eh = (2 / (np.sqrt(3) * h)) * np.cos(a + np.pi / 3)
22     outer_eh = (2 / (np.sqrt(3) * h)) * np.cos(a - np.pi / 3)
23
24     plt.figure(figsize=(14, 6), facecolor='white')
25     plt.xlabel(r"Cosmological Constant, $\Lambda$ \ [m$^{-2}$]")
26     plt.ylabel(r"Radial distance, $r$ \ [m]")
27     plt.axhline(0, linestyle='--', color='k')
28     plt.axvline(0, linestyle='--', color='k')
29     plt.xlim(1e-7, 1 / (9 * m**2) + 5e-2)
30
31     plt.loglog(L, outer_eh, 'k', label=r'Cosmological Horizon, $r_{\text{eh}}$', linewidth=4)
32     plt.loglog(L, inner_eh, 'orange', label=r'BH Event Horizon, $r_{\text{eh}}$', linewidth=4)
33     plt.loglog(L, 3*m * L/L, 'b', label=r'Photon Sphere at $r_{\text{ps}}$ = 3m', linewidth=4)
34
35     plt.legend()
36     plt.savefig(fr"Kottler Surfaces.png", bbox_inches='tight', dpi=500)
37
38 plot_potential(m=1)

```

## B.11 Plot 29

```

1 import matplotlib.pyplot as plt
2 import math

```

```

3 import numpy as np
4
5 plt.rcParams["font.size"] = 20
6 plt.rcParams["font.weight"] = "normal"
7 plt.rcParams['font.family'] = 'STIXGeneral'
8 plt.rcParams['mathtext.fontset'] = 'stix'
9
10 def static_kottler(m, H0, r0):
11     num = (1 - 2 * m / r0 - H0**2 * r0**2)
12     den = (1 - 27 * H0 ** 2 * m**2)
13     kottler_shadow = np.arcsin( (3 * m * np.sqrt(3) / r0) * np.sqrt(num /
14         den) )
15
16     return kottler_shadow
17
18 def comoving_kottler(m, H0, r0):
19     term1 = np.sqrt(27) * m / r0
20     term2 = np.sqrt(1 - 2 * m / r0)
21     term3 = np.sqrt(1 - 27 * H0 **2 * m **2)
22     term4 = np.sqrt(27) * m * H0
23     term5 = np.sqrt(1 - 27 * m **2 * (1 - 2 * m / r0) / r0 ** 2)
24     kottler_shadow = np.arcsin(term1 * term2 * term3 + term4 * term5)
25
26     return kottler_shadow
27
28 def plot_Kottler_shadow(m, L, axis, color, r_lim):
29     H0 = np.sqrt(L / 3)
30     a = (1 / 3) * np.arccos(np.sqrt(27) * m * H0)
31     inner_eh = (2 / (np.sqrt(3) * H0)) * np.cos(a + np.pi / 3)
32     outer_eh = (2 / (np.sqrt(3) * H0)) * np.cos(a - np.pi / 3)
33     r0 = np.linspace(inner_eh, r_lim, 100000)
34
35     axis[0].plot(r0, static_kottler(m=m, H0=H0, r0=r0), color=color, label=
36     =fr"\Lambda$ = {L}", linewidth=3)
37     axis[1].plot(r0, comoving_kottler(m=m, H0=H0, r0=r0), label=fr"\Lambda$ =
38     = {L}", color=color, linewidth=3)

```

```

34
35 def plot_figure(m, lambda_list, upper_bound):
36     Lambda_list = [L for L in lambda_list if L < (1 / (9 * m * m))]
37     if Lambda_list != lambda_list: print(f'Parameters L = {set(Lambda_list)}\n'
38     f' ~ set(lambda_list) exceed 1 / 9m^2')
39
40     color_list = ['brown', 'red', 'darkorange', 'gold', 'limegreen']
41     r0 = np.linspace(3 * m, 100 * m, 10000)[1:-1]
42     photon_sphere = 3 * m
43     schw_shadow = np.arcsin((3 * np.sqrt(3) * m / r0) * np.sqrt(1 - 2 * m
44     / r0))
45
46     fig, axis = plt.subplots(nrows = 2, ncols=1, figsize=(13, 13),
47     facecolor='white')
48
49     for ax in axis:
50         ax.set_xlim(0.94*photon_sphere, upper_bound)
51         ax.set_ylim(0, 1.07*max(schw_shadow))
52         ax.set_xlabel(r"Observer distance, $r_{\text{sh}}$ [m]")
53         ax.axvline(3*m, color='k', linestyle='--', label=r'Photon Sphere',
54         $r_{\text{ps}}$, linewidth=3)
55
56         axis[0].set_title('Static Observer')
57         axis[0].set_ylabel(r"Angular size, $\alpha_{\text{sh}, \text{static}}$")
58         for i, L in enumerate(Lambda_list):
59             plot_Kottler_shadow(m=m, L=L, axis=axis, color=color_list[i],
60             r_lim=upper_bound)
61
62         axis[0].plot(r0, schw_shadow, 'b--', label="Schwarzschild", linewidth
63         =4)
64
65         axis[1].plot(r0, schw_shadow, 'b--', label="Schwarzschild", linewidth
66         =4)
67
68         axis[1].set_title('Comoving Observer')

```

```

61 axis[1].set_ylabel(r"Angular size, $\alpha_{\text{sh, comov}}$")
62
63 fig.tight_layout()
64 handles, labels = ax.get_legend_handles_labels()
65 unique = [(h, l) for i, (h, l) in enumerate(zip(handles, labels)) if l
66 not in labels[:i]]
67 axis[0].legend(*zip(*unique), loc=1)
68 # plt.savefig(fr"C:\Users\dimit\Computational Physics\Thesis\Kottler
69 Static and Comoving.png", bbox_inches='tight', dpi=500)
70
71 plot_figure(m=1, lambda_list=[1e-2, 1e-3, 5e-4, 1e-7], upper_bound = 80)

```

## B.12 Plot 30

```

1 import matplotlib.pyplot as plt
2 import math
3 import numpy as np
4
5 plt.rcParams["font.size"] = 20
6 plt.rcParams["font.weight"] = "normal"
7 plt.rcParams['font.family'] = 'STIXGeneral'
8 plt.rcParams['mathtext.fontset'] = 'stix'
9
10 def scale_factor(m, H0, R0):
11     mcvittie_shadow = np.arcsin((3 * np.sqrt(3) * m / R0) * np.sqrt(1 -
12         2 * m / R0)) + (3 * np.sqrt(3) * m / R0) * ((1 - H0 * R0 / 2) **
13         (-2) - 1)
14     return mcvittie_shadow
15
16
17 def plot_Kottler_shadow(m, H0, axis, color):
18     r0 = np.linspace(2 * m, 100 * m, 100)[1:-1]
19
20     axis.plot(r0, scale_factor(m=m, H0=H0, R0=r0), color=color, label=f"{}$H_0$ = {H0}", linewidth=3)

```

```

18
19 def plot_figure(m, H0_list):
20     color_list = ['brown', 'red', 'darkorange', 'gold', 'limegreen']
21     r0 = np.linspace(2 * m, 100 * m, 100)
22     photon_sphere = 3 * m
23     schw_shadow = np.arcsin((3 * np.sqrt(3) * m / r0) * np.sqrt(1 - 2 * m
24     / r0))
25
26     fig, axis = plt.subplots(figsize=(13, 6), facecolor='white')
27     plt.xlim(photon_sphere, 100 * m)
28     plt.ylim(0, 1.1*max(schw_shadow))
29     axis.set_xlabel(r"Observer distance, $R_\text{text{0}}$ [m]")
30     axis.set_ylabel(r"Angular size, $\alpha_\text{text{sh}}$")
31     for i, H0 in enumerate(H0_list):
32         plot_Kottler_shadow(m=m, H0=H0, axis=axis, color=color_list[i])
33
34     axis.plot(r0, schw_shadow, 'b--', label="Schwarzschild", linewidth=4)
35     plt.legend(loc=1, fontsize=18)
36     plt.savefig(fr"C:\Users\dimit\Computational Physics\Thesis\McVittie
37 Matter Dominated.png", bbox_inches='tight', dpi=500)
38
39 plot_figure(m=1, H0_list=[2e-2, 1.5e-2, 1e-2, 1e-7])

```

## B.13 Plot 31

```

1 import matplotlib.pyplot as plt
2 import math
3 import numpy as np
4
5 plt.rcParams["font.size"] = 18
6 plt.rcParams["font.weight"] = "normal"
7 plt.rcParams['font.family'] = 'STIXGeneral',
8 plt.rcParams['mathtext.fontset'] = 'stix'
9

```

```

10 def plot_figure(z_max):
11     color_list = ['brown', 'red', 'darkorange', 'gold', 'limegreen']
12     z = np.linspace(0.001, z_max, 10000)
13     daz_matter = 2 / (1 + z) * (1 - 1 / np.sqrt(1 + z))
14     daz_radiation = 1 / (1 + z) * (1 - 1 / (1 + z))
15     daz_lambda = 1 / (1 + z) * z
16
17     fig, axis = plt.subplots(figsize=(13, 7), facecolor='white')
18     axis.set_xlim(0.001, z_max)
19     axis.set_ylim(0, 1)
20     axis.set_xlabel(r"Redshift, $z$")
21     axis.set_ylabel(r"SOLID: Angular diameter distance, $d_A(z)$")
22
23     axis.plot(z, daz_lambda, 'g', label="Dark Energy Dominated", linewidth=4)
24     axis.plot(z, daz_matter, 'b', label="Matter Dominated", linewidth=4)
25     axis.plot(z, daz_radiation, 'r', label="Radiation Dominated",
26               linewidth=4)
26     plt.legend(loc=2, fontsize=16)
27
28     axis2 = axis.twinx()
29     axis2.set_ylabel(r"DASHED: Cosmological shadow size, $\alpha \text{ text{outer}} = \frac{3 \sqrt{3} m}{d_A(z)}$")
30     axis2.set_xlim(0.01, 10)
31     axis2.set_ylim(0, 12)
32     axis2.plot(z, 1/daz_lambda, 'g--', linewidth=2)
33     axis2.plot(z, 1/daz_matter, 'b--', linewidth=2)
34     axis2.plot(z, 1/daz_radiation, 'r--', linewidth=2)
35
36     plt.savefig(fr"C:\Users\dimit\Computational Physics\Thesis\Angular
37     Diamter Distances.png", bbox_inches='tight', dpi=500)
38 plot_figure(z_max=12)

```

## References

- [1] Black Hole Perturbation Toolkit. ([bhptoolkit.org](http://bhptoolkit.org)).
- [2] R. Adler, M. Bazin, M. Schiffer, and J. E. Romain. Introduction to general relativity. *Physics Today*, 18(9):68–68, 09 1965. ISSN 0031-9228. doi: 10.1063/1.3047725. URL <https://doi.org/10.1063/1.3047725>.
- [3] R. J. Adler, B. Casey, and O. C. Jacob. Vacuum catastrophe: An elementary exposition of the cosmological constant problem. *American Journal of Physics*, 63(7):620–626, 07 1995. ISSN 0002-9505. doi: 10.1119/1.17850. URL <https://doi.org/10.1119/1.17850>.
- [4] K. Akiyama et al. First M87 event horizon telescope results. IV. imaging the central supermassive black hole. *The Astrophysical Journal Letters*, 875(1):L4, apr 2019. doi: 10.3847/2041-8213/ab0e85. URL <https://dx.doi.org/10.3847/2041-8213/ab0e85>.
- [5] K. Akiyama et al. First Sagittarius A\* event horizon telescope results. I. the shadow of the supermassive black hole in the center of the Milky Way. *The Astrophysical Journal Letters*, 930(2):L12, May 2022. ISSN 2041-8213. doi: 10.3847/2041-8213/ac6674. URL <http://dx.doi.org/10.3847/2041-8213/ac6674>.
- [6] R. Allahverdi and J. K. Osiński. Early matter domination from long-lived particles in the visible sector. *Physical Review D*, 105(2), Jan. 2022. ISSN 2470-0029. doi: 10.1103/physrevd.105.023502. URL <http://dx.doi.org/10.1103/PhysRevD.105.023502>.
- [7] D. Arora, N. U. Molla, H. Chaudhary, U. Debnath, F. Atamurotov, and G. Mustafa. Exploring tidal force effects and shadow constraints for Schwarzschild-like black hole in Starobinsky-Bel-Robinson gravity, 2023. URL <https://arxiv.org/abs/2308.13901>.
- [8] E. Baird. Relativistic angle-changes and frequency-changes, 2000. URL <https://arxiv.org/abs/physics/0010006>.
- [9] J. D. Barrow and D. J. Shaw. The value of the cosmological constant. *General Relativity and Gravitation*, 43(10):2555–2560, June 2011. ISSN 1572-9532. doi: 10.1007/s10714-011-1199-1. URL <http://dx.doi.org/10.1007/s10714-011-1199-1>.
- [10] J. Beall. A Review of Astrophysical Jets. In *Proceedings of XI Multifrequency Behaviour of High Energy Cosmic Sources Workshop — PoS(MULTIF15)*, volume 246, page 058, 2016. doi: 10.22323/1.246.0058.

- [11] A. Belhaj, H. Belmahi, M. Benali, Y. Hassouni, and M. B. Sedra. Deflection angle and shadows by black holes in Starobinsky-Bel-Robinson gravity from M-theory, 2023. URL <https://arxiv.org/abs/2304.03883>.
- [12] G. S. Bisnovatyi-Kogan and O. Y. Tsupko. Shadow of a black hole at cosmological distances. *Physical Review D*, 98(8), Oct. 2018. ISSN 2470-0029. doi: 10.1103/physrevd.98.084020. URL <http://dx.doi.org/10.1103/PhysRevD.98.084020>.
- [13] S. Borghini, P. T. Chruściel, and L. Mazzieri. On the uniqueness of Schwarzschild-de Sitter spacetime. *Archive for Rational Mechanics and Analysis*, 247(2), Mar. 2023. ISSN 1432-0673. doi: 10.1007/s00205-023-01860-1. URL <http://dx.doi.org/10.1007/s00205-023-01860-1>.
- [14] C. J. Camilleri. *Tensor Analysis*. Malta University Press, 1999. ISBN 9789990945003. URL <https://staff.um.edu.mt/ccam1/tensor%20short%20sample%20secure.pdf>.
- [15] S. M. Carroll. *Spacetime and Geometry: An Introduction to General Relativity*. Cambridge University Press, 2019.
- [16] B. Carter. Global structure of the Kerr family of gravitational fields. *Phys. Rev.*, 174:1559–1571, Oct 1968. doi: 10.1103/PhysRev.174.1559. URL <https://link.aps.org/doi/10.1103/PhysRev.174.1559>.
- [17] S. Chandrasekhar. *The mathematical theory of black holes*. 1985. ISBN 978-0-19-850370-5.
- [18] Y.-X. Chen, J.-H. Huang, and H. Jiang. Radii of spherical photon orbits around Kerr-Newman black holes. *Physical Review D*, 107(4), Feb. 2023. ISSN 2470-0029. doi: 10.1103/physrevd.107.044066. URL <http://dx.doi.org/10.1103/PhysRevD.107.044066>.
- [19] P. T. Chruściel, J. L. Costa, and M. Heusler. Stationary black holes: Uniqueness and beyond. *Living Reviews in Relativity*, 15(1), May 2012. ISSN 1433-8351. doi: 10.12942/lrr-2012-7. URL <http://dx.doi.org/10.12942/lrr-2012-7>.
- [20] A. Das, A. Saha, and S. Gangopadhyay. Shadow of Kottler black hole in the presence of plasma for a co-moving observer. *Classical and Quantum Gravity*, 40(1):015008, Dec. 2022. ISSN 1361-6382. doi: 10.1088/1361-6382/aca5e4. URL <http://dx.doi.org/10.1088/1361-6382/aca5e4>.
- [21] A. De Felice and S. Tsujikawa. f(R) theories. *Living Reviews in Relativity*, 13(1), apr 2010. doi: 10.12942/lrr-2010-3. URL <https://doi.org/10.12942/lrr-2010-3>.

- [22] N. ESA. Einstein ring LRG 3-757, 2011. URL <https://science.nasa.gov/image-detail/einstein-ring-lrg-3-757/>.
- [23] V. Faraoni. Embedding black holes and other inhomogeneities in the universe in various theories of gravity: a short review, 2018. URL <https://arxiv.org/abs/1810.04667>.
- [24] V. Ferrari. Chapter 22: Geodesic motion in Kerr spacetime. Mar. 2019. URL [https://www.roma1.infn.it/teongrav/onde19\\_20/geodetiche\\_Kerr.pdf](https://www.roma1.infn.it/teongrav/onde19_20/geodetiche_Kerr.pdf).
- [25] S. E. Gralla, D. E. Holz, and R. M. Wald. Black hole shadows, photon rings, and lensing rings. *Physical Review D*, 100(2), July 2019. ISSN 2470-0029. doi: 10.1103/physrevd.100.024018. URL <http://dx.doi.org/10.1103/PhysRevD.100.024018>.
- [26] A. Grenzebach. *The Shadow of Black Holes*, pages 55–79. Springer International Publishing, Cham, 2016. ISBN 978-3-319-30066-5. doi: 10.1007/978-3-319-30066-5\_4. URL [https://doi.org/10.1007/978-3-319-30066-5\\_4](https://doi.org/10.1007/978-3-319-30066-5_4).
- [27] A. Grenzebach, V. Perlick, and C. Lämmerzahl. Photon regions and shadows of Kerr-Newman-NUT black holes with a cosmological constant. *Physical Review D*, 89(12), June 2014. ISSN 1550-2368. doi: 10.1103/physrevd.89.124004. URL <http://dx.doi.org/10.1103/PhysRevD.89.124004>.
- [28] S. Hod. Spherical null geodesics of rotating Kerr black holes. *Physics Letters B*, 718(4–5):1552–1556, Jan. 2013. ISSN 0370-2693. doi: 10.1016/j.physletb.2012.12.047. URL <http://dx.doi.org/10.1016/j.physletb.2012.12.047>.
- [29] M. H. Holmes. *Introduction to Perturbation Methods*. Springer New York, NY, 2012. doi: 10.1007/9. URL <https://doi.org/10.1007/9>.
- [30] J. Islam. The cosmological constant and classical tests of general relativity. *Physics Letters A*, 97(6):239–241, 1983. ISSN 0375-9601. doi: [https://doi.org/10.1016/0375-9601\(83\)90756-9](https://doi.org/10.1016/0375-9601(83)90756-9). URL <https://www.sciencedirect.com/science/article/pii/0375960183907569>.
- [31] R. Karmakar and U. D. Goswami. Quasinormal modes, thermodynamics and shadow of black holes in Hu–Sawicki f(R) gravity theory. *The European Physical Journal C*, 84(9), Sept. 2024. ISSN 1434-6052. doi: 10.1140/epjc/s10052-024-13359-4. URL <http://dx.doi.org/10.1140/epjc/s10052-024-13359-4>.
- [32] Y. Kim, C. Y. Oh, and N. Park. Classical geometry of De Sitter spacetime : An introductory review, 2002. URL <https://arxiv.org/abs/hep-th/0212326>.

- [33] R. Kumar and S. G. Ghosh. Black hole parameter estimation from its shadow. *The Astrophysical Journal*, 892(2):78, mar 2020. doi: 10.3847/1538-4357/ab77b0. URL <https://dx.doi.org/10.3847/1538-4357/ab77b0>.
- [34] O. Lahav and A. R. Liddle. The cosmological parameters, 2004. URL <https://arxiv.org/abs/astro-ph/0406681>.
- [35] D. Lebedev and K. Lake. Relativistic aberration and the cosmological constant in gravitational lensing I: Introduction, 2016. URL <https://arxiv.org/abs/1609.05183>.
- [36] J.-P. Luminet. Image of a spherical black hole with thin accretion disk. *Astronomy and Astrophysics*, 75:228–235, 04 1979.
- [37] G. E. Marsh. The infinite red-shift surfaces of the Kerr and Kerr-Newman solutions of the Einstein field equations, 2007. URL <https://arxiv.org/abs/gr-qc/0702114>.
- [38] C. W. Misner, K. S. Thorne, and J. A. Wheeler. *Gravitation*. 1973.
- [39] Y. Mizuno, Z. Younsi, C. M. Fromm, O. Porth, M. De Laurentis, H. Olivares, H. Falcke, M. Kramer, and L. Rezzolla. The current ability to test theories of gravity with black hole shadows. *Nature Astronomy*, 2(7):585–590, Apr. 2018. ISSN 2397-3366. doi: 10.1038/s41550-018-0449-5. URL <http://dx.doi.org/10.1038/s41550-018-0449-5>.
- [40] G. Mohan, N. Parbin, and U. D. Goswami. Investigating the effects of gravitational lensing by Hu-Sawicki f(R) gravity black holes. *Eur. Phys. J. C*, 85(4):413, 2025. doi: 10.1140/epjc/s10052-025-14143-8.
- [41] V. Mukhanov. *Physical Foundations of Cosmology*. Cambridge University Press, 2005.
- [42] R. Narayan and E. Quataert. Black hole accretion. *Science (New York, N.Y.)*, 307:77–80, 02 2005. doi: 10.1126/science.1105746.
- [43] B. C. Nolan. Particle and photon orbits in McVittie spacetimes. *Classical and Quantum Gravity*, 31(23):235008, Nov. 2014. ISSN 1361-6382. doi: 10.1088/0264-9381/31/23/235008. URL <http://dx.doi.org/10.1088/0264-9381/31/23/235008>.
- [44] P. Padhye, K. Paithankar, and S. Kolekar. Existence of photon region for stationary axisymmetric black holes, 2024. URL <https://arxiv.org/abs/2412.12665>.

- [45] R. Penrose. Gravitational collapse: the role of general relativity. 1969. URL <https://www.physics.umd.edu/grt/taj/776b/PenroseReview.pdf>.
- [46] V. Perlick. Black holes. July 2022. URL [https://www.zarm.uni-bremen.de/fileadmin/user\\_upload/space\\_science/gravitational\\_theory/BH22.pdf](https://www.zarm.uni-bremen.de/fileadmin/user_upload/space_science/gravitational_theory/BH22.pdf).
- [47] V. Perlick and O. Y. Tsupko. Calculating black hole shadows: Review of analytical studies. *Physics Reports*, 947:1–39, Feb. 2022. ISSN 0370-1573. doi: 10.1016/j.physrep.2021.10.004. URL <http://dx.doi.org/10.1016/j.physrep.2021.10.004>.
- [48] V. Perlick, O. Y. Tsupko, and G. S. Bisnovatyi-Kogan. Black hole shadow in an expanding universe with a cosmological constant. *Physical Review D*, 97(10), May 2018. ISSN 2470-0029. doi: 10.1103/physrevd.97.104062. URL <http://dx.doi.org/10.1103/PhysRevD.97.104062>.
- [49] P. Pesic. *Abel's Proof: An Essay on the Sources and Meaning of Mathematical Unsolvability*. MIT Press, 2003. ISBN 9781139451994. URL [https://www.google.rs/books/edition/Abel\\_s\\_Proof/nIpGp9Y5A1EC?hl=en](https://www.google.rs/books/edition/Abel_s_Proof/nIpGp9Y5A1EC?hl=en).
- [50] H. Pfister. On the history of the so-called Lense-Thirring effect. *General Relativity and Gravitation*, 39(11):1735–1748, Nov. 2007. doi: 10.1007/s10714-007-0521-4.
- [51] O. F. Piattella. Lensing in the McVittie metric, 2016. URL <https://arxiv.org/abs/1508.04763>.
- [52] E. Poisson. *A Relativist's Toolkit: The Mathematics of Black-Hole Mechanics*. Cambridge University Press, 2004. ISBN 9781139451994. URL [https://books.google.it/books?id=bk2XEgz\\_ML4C](https://books.google.it/books?id=bk2XEgz_ML4C).
- [53] N. Popławski. Black holes in the expanding universe. *Classical and Quantum Gravity*, 42(6):065017, Mar. 2025. ISSN 1361-6382. doi: 10.1088/1361-6382/adb537. URL <http://dx.doi.org/10.1088/1361-6382/adb537>.
- [54] J. Pérez-Romero and S. Nesseris. Cosmological constraints and comparison of viable f(R) models. *Physical Review D*, 97(2), Jan. 2018. ISSN 2470-0029. doi: 10.1103/physrevd.97.023525. URL <http://dx.doi.org/10.1103/PhysRevD.97.023525>.
- [55] W. Rindler. Visual horizons in world models. *Monthly Notices of the Royal Astronomical Society*, 116:662–677, Dec. 1956. doi: 10.1093/mnras/116.6.662. URL <https://doi.org/10.1093/mnras/116.6.662>.

- [56] E. Siegel. What the 3 biggest physics discoveries of the decade mean for the future of science, 2019. URL <https://www.forbes.com/sites/startswithabang/2019/12/20/what-the-3-biggest-physics-discoveries-of-the-decade-mean-for-the-future-of-science/>.
- [57] A. H. Sofi, M. A. Shah, M. R. Sibuea, S. A. Akhoon, B. N. Khanday, S. U. Majeed, A. A. Rather, and I. Nahvi. Quantum field theory in de Sitter spacetime, 2013. URL <https://arxiv.org/abs/1312.0311>.
- [58] R. Solanki. Kottler spacetime in isotropic static coordinates. *Classical and Quantum Gravity*, 39(1):015015, Dec. 2021. ISSN 1361-6382. doi: 10.1088/1361-6382/ac3aa0. URL <http://dx.doi.org/10.1088/1361-6382/ac3aa0>.
- [59] H. Stephani, D. Kramer, M. MacCallum, C. Hoenselaers, and E. Herlt. *Exact Solutions of Einstein's Field Equations*. Cambridge Monographs on Mathematical Physics. Cambridge University Press, 2 edition, 2003.
- [60] Z. Stuchlík, D. Charbulák, and J. Schee. Light escape cones in local reference frames of Kerr-deSitter black hole spacetimes and related black hole shadows. *The European Physical Journal C*, 78(3), Mar. 2018. ISSN 1434-6052. doi: 10.1140/epjc/s10052-018-5578-6. URL <http://dx.doi.org/10.1140/epjc/s10052-018-5578-6>.
- [61] J. L. Synge. The escape of photons from gravitationally intense stars. *Monthly Notices of the Royal Astronomical Society*, 131(3):463–466, 02 1966. ISSN 0035-8711. doi: 10.1093/mnras/131.3.463. URL <https://doi.org/10.1093/mnras/131.3.463>.
- [62] F. Tamburini, B. Thidé, and M. Della Valle. Measurement of the spin of the M87 black hole from its observed twisted light. *Monthly Notices of the Royal Astronomical Society: Letters*, 492(1):L22–L27, Nov. 2019. ISSN 1745-3933. doi: 10.1093/mnrasl/slz176. URL <http://dx.doi.org/10.1093/mnrasl/slz176>.
- [63] A. Tavlayan and B. Tekin. Exact formulas for spherical photon orbits around Kerr black holes. *Physical Review D*, 102(10), Nov. 2020. ISSN 2470-0029. doi: 10.1103/physrevd.102.104036. URL <http://dx.doi.org/10.1103/PhysRevD.102.104036>.
- [64] J. Taylor. *Classical Mechanics*. G - Reference,Information and Interdisciplinary Subjects Series. University Science Books, 2005. ISBN 9781891389221. URL <https://books.google.it/books?id=P1kCtNr-pJsC>.

- [65] O. Y. Tsupko and G. S. Bisnovatyi-Kogan. First analytical calculation of black hole shadow in McVittie metric. *International Journal of Modern Physics D*, 29(09):2050062, July 2020. ISSN 1793-6594. doi: 10.1142/s0218271820500625. URL <http://dx.doi.org/10.1142/S0218271820500625>.
- [66] O. Y. Tsupko, Z. Fan, and G. S. Bisnovatyi-Kogan. Black hole shadow as a standard ruler in cosmology. *Classical and Quantum Gravity*, 37(6):065016, Feb. 2020. ISSN 1361-6382. doi: 10.1088/1361-6382/ab6f7d. URL <http://dx.doi.org/10.1088/1361-6382/ab6f7d>.
- [67] S. Vagnozzi, C. Bambi, and L. Visinelli. Concerns regarding the use of black hole shadows as standard rulers. *Classical and Quantum Gravity*, 37(8):087001, Apr. 2020. ISSN 1361-6382. doi: 10.1088/1361-6382/ab7965. URL <http://dx.doi.org/10.1088/1361-6382/ab7965>.
- [68] R. M. Wald. *General Relativity*. Chicago Univ. Pr., Chicago, USA, 1984. doi: 10.7208/chicago/9780226870373.001.0001.
- [69] K. Wang, C.-J. Feng, and T. Wang. Image of Kerr-de Sitter black holes illuminated by equatorial thin accretion disks. *The European Physical Journal C*, 84, 05 2024. doi: 10.1140/epjc/s10052-024-12825-3.
- [70] S.-W. Wei, Y.-C. Zou, Y.-X. Liu, and R. B. Mann. Curvature radius and Kerr black hole shadow. *Journal of Cosmology and Astroparticle Physics*, 2019(08):030–030, Aug. 2019. ISSN 1475-7516. doi: 10.1088/1475-7516/2019/08/030. URL <http://dx.doi.org/10.1088/1475-7516/2019/08/030>.
- [71] S. Wiessinger. NASA scientific visualization studio: Black hole snapshot, 2012. URL <https://svs.gsfc.nasa.gov/10987/>.
- [72] K. Yagi and L. C. Stein. Black hole based tests of general relativity. *Classical and Quantum Gravity*, 33(5):054001, Feb. 2016. ISSN 1361-6382. doi: 10.1088/0264-9381/33/5/054001. URL <http://dx.doi.org/10.1088/0264-9381/33/5/054001>.
- [73] A. Zakharov. Shadows as a tool to evaluate black hole parameters including a tidal charge for extra dimension of spacetime. *New Astronomy Reviews*, 56:64–73, 07 2012. doi: 10.1016/j.newar.2011.09.002.